

# General Relativistic Multi Dimensional Simulations of Electron Capture Supernovae

Janina von Groote



TECHNISCHE UNIVERSITÄT MÜNCHEN

MAX-PLANCK-INSTITUT  
FÜR  
ASTROPHYSIK

**General Relativistic  
Multi Dimensional Simulations  
of Electron Capture Supernovae**

**Janina Christine von Grootte**

Vollständiger Abdruck der an die Fakultät für Physik der Technischen Universität München zur Erlangung des akademischen Grades eines

**Doktors der Naturwissenschaften (Dr. rer. nat.)**

eingereichten Dissertation.

Vorsitzende(r): Univ. – Prof. Dr. Lothar Oberauer  
Prüfer der Dissertation: 1. Priv. – Doz. Dr. Hans-Thomas Janka  
2. Univ. – Prof. Dr. Alejandro Ibarra

Die Dissertation wurde am 01.09.2014 bei der Technischen Universität München eingereicht und durch die Fakultät für Physik am 07.11.2014 angenommen.



Für meinen Papa



# Contents

<b>1</b>	<b>Introduction</b>	<b>1</b>
<b>2</b>	<b>Numerical Implementation</b>	<b>5</b>
2.1	Hydrodynamics . . . . .	5
2.2	Equation of State (EoS) . . . . .	8
2.3	Nuclear burning treatment . . . . .	10
2.4	Neutrino transport . . . . .	11
2.5	Nucleon potentials . . . . .	15
2.6	Convection . . . . .	15
2.7	Simulations . . . . .	15
<b>3</b>	<b>Spherically Symmetric Simulations (1D)</b>	<b>17</b>
3.1	Progenitor . . . . .	19
3.2	Overview . . . . .	22
3.3	Resolution study . . . . .	26
3.3.1	Energy resolution . . . . .	26
3.3.2	Radial resolution . . . . .	28
3.4	Early Phase . . . . .	32
3.4.1	GR vs. Post-Newton . . . . .	33
3.4.2	Nucleon potentials . . . . .	34
3.4.3	Convection . . . . .	37
3.4.4	Network . . . . .	46
3.4.5	EoS . . . . .	47
3.5	Cooling . . . . .	55
3.5.1	GR vs. Post-Newton . . . . .	56
3.5.2	Nucleon potentials . . . . .	59
3.5.3	Convection . . . . .	62
3.5.4	EoS . . . . .	68
3.6	Neutrino Driven Wind . . . . .	73
3.6.1	GR vs. Post-Newton . . . . .	75
3.6.2	Nucleon potentials . . . . .	76
3.6.3	Convection . . . . .	81
3.6.4	Network . . . . .	81
3.6.5	EoS . . . . .	81
3.7	Explosion Energy . . . . .	87
3.7.1	GR vs. Post-Newton . . . . .	88

3.7.2	Nucleon potentials . . . . .	91
3.7.3	Convection . . . . .	93
3.7.4	Network . . . . .	94
3.7.5	EoS . . . . .	94
<b>4</b>	<b>Axially Symmetric Simulations (2D)</b>	<b>99</b>
4.1	Angular resolution . . . . .	100
4.2	Neutrino signal for different EoS . . . . .	106
4.3	Early Ejecta . . . . .	109
4.4	Cooling . . . . .	118
4.5	Explosion energy . . . . .	123
<b>5</b>	<b>Summary and Conclusion</b>	<b>125</b>
	<b>Bibliography</b>	<b>137</b>

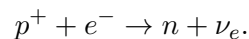




# 1 Introduction

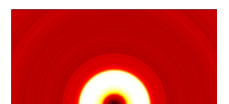
Supernovae are powerful explosions when stars reach the end of their life. They are fascinating phenomena that involve a broad spectrum of different branches of physics. For some class of supernovae, core collapses, a neutron star comes into existence. Their properties need to be described by high-density nuclear physics. To describe the dynamics of the collapse and the explosion of the star we have to use hydrodynamics. At the same time neutrinos play a very important role, which have to be described by particle physics and their interaction with the stellar matter has to be modelled with radiative transport methods. An accurate description of a supernova thus becomes very complicated and can only be accomplished by numerical simulations.

The type of supernova we are interested in are indeed such core collapse supernovae. In this scenario the star collapses when its gas pressure, thermally generated by the fusion of its light elements, becomes incapable of sustaining the star against its own gravity. The core of the star collapses and the density of the inner core rises, till nuclear density is reached. Then, strong nuclear forces appear and are enough to hold the collapse. This sudden halt causes a slight rebound and a shock wave is formed which moves outwards. From the outer hull of the star matter is still falling onto the core which causes the shock to stall. At the high-density conditions in the proto neutron star it becomes favourable for protons and electrons to transform into neutrons and neutrinos,



Next to that, huge amounts of neutrinos are also thermally produced. These highly energetic neutrinos slowly leave the core and might be capable of re-energising the shock and thereby cause the explosion of the star, provided they deposit a fraction of their energy on their way out.

An important subclass of this kind of supernovae are the so called Electron Capture Supernova (ECSN). Most massive stars collapses with an iron core at the end of their life. The least massive stars that still undergo a core collapse end up with a strongly degenerate Oxygen, Neon and Magnesium core. There the collapse is initiated by rapid electron captures on O, Ne, and Mg before a large iron core has formed. These stars are interesting as they end up with a thin, loosely-bound outer hull, due to their previous evolution. Therefore, the explosion is achieved easily, while simulations of iron core collapses still have difficulties to predict robust explosions. Also, more low mass stars exist than high mass stars – it was calculated that ECSN could make-up up to  $\approx 30\%$  of all supernovae (Wanajo et al., 2009). A



prominent example is the Crab Nebula, that was formed by the supernova observed in the year 1054, that is thought to be the remnant of such an event.

Furthermore supernovae eject elements which were fused during the evolution of the star, additionally more heavy elements can be produced during the explosion itself. It is believed that ECSN might be able to produce r-process elements, as their explosion is so fast that they might eject neutrino rich matter with the right conditions for r-process nucleosynthesis to occur. As neutrinos play an important role for the explosion, a sophisticated neutrino transport is needed to simulate these kind of supernovae.

Between the first attempt to simulate a supernova and the formation of a neutron star (Colgate et al., 1961) and today's multi dimensional, even fully 3D, simulations, (Nordhaus et al., 2010; Hanke et al., 2012; Burrows, 2012; Murphy et al., 2013; Dolence et al., 2013; Couch, 2013; Hanke et al., 2013) several improvements have been made. The important role of neutrinos for the explosion was already suggested by Colgate and White (1966), and experimentally confirmed when neutrino detectors observed a handful of neutrinos from a supernova in the Large Magellanic Cloud in 1987. Epstein (1979) suggested that instabilities due to convection should be considered, e.g. Colgate and Petschek (1980) simulated therefore Rayleigh-Taylor instabilities within the core. Additionally Bethe (1990) also mentioned the importance of convective instabilities outside the core. With the improvement of computers more and more sophisticated simulations were possible, and still improvements are made. But there are still some unknowns, like purely constrained high-density nuclear physics, needed to describe the proto neutron star (see e.g. Lattimer, 2006; Lattimer and Prakash, 2007; Steiner et al., 2013). We have to deal with this by using a number of different models in the form of Equation of State tables, given to us by nuclear theorists.

We hope to contribute to the knowledge about supernovae, by simulating ECSN with a number of different Equations of State and improved micro physics, in spherically and axially symmetric radiation-hydrodynamical simulations in general relativity.

We will address the influence of general relativity on the explosion of the star and the cooling of the proto neutron star. GR is necessary as both the proto neutron star is a very compact object and the velocities in such a supernova explosion can easily approach the speed of light. Most previous studies either approximated the effects of GR or used a comparable less sophisticated neutrino treatment. Martínez-Pinedo et al. (2012) and Roberts (2012 and Roberts et al., 2012a) discovered that previously published simulations with the VERTEX and VERTEX-CoCoNuT code (which we also use here) neglected an important term in the neutrino-nucleon cross section related to the nucleon mean-field potentials at high densities. This is corrected in the simulations shown here and the influence of the correction will be studied. Additionally, we will investigate the effect of convection and methods to model this multi dimensional effect in spherical symmetry and compare this to axially symmetric simulations. Wanajo et al. (2011, 2013a) noted that multi dimensional simulations of ECSNe can eject also some neutron rich matter and

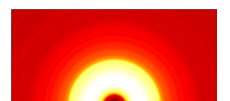


could thus be a site for r-process nucleosynthesis. We will reinvestigate this with our general relativistic code and better numerical resolution, and also over a longer timespan than previous work. Furthermore, we are also interested in the influence of different Equations of State, and will therefore make use of five different Equation of State tables.

## Organization of the Thesis

In this thesis we will first discuss the numerics of the code we used for our simulations in Chapter 2. The rest of the thesis is split in to two main chapters, one for the spherically symmetric (“1D”) simulations in Chapter 3, and one for the axially symmetric (“2D”) simulations in Chapter 4. In the 1D chapter we will also give a short overview over the progenitor we use and its explosion. The effects of different energy and radial resolutions will be discussed. In the rest of this chapter we will discuss the collapse and explosion of the star, the following cooling of the proto neutron star, the neutrino driven wind, and the explosion energy. In each of these sections we will discuss the influence of general relativity, the corrected nucleon opacities, convection and the effect of different Equations of State.

In the 2D chapter we will additionally address the influence of the angular resolution. We will show the neutrino signal, and early ejecta, for different Equations of State. The cooling phase, and explosion energy, will be discussed on the example of one long time 2D simulation and compared with 1D results.





## 2 Numerical Implementation

2 x 3 macht 4  
Widdewiddewitt und Drei  
macht Neune!  
Ich mach' mir die Welt  
Widdewidde wie sie mir gefällt

---

*(Hey, Pippi Langstrumpf,  
Astrid Lindgren, dt. Ver-  
sion von Wolfgang Franke)*

For our supernova simulations we use the VERTEX<sup>1</sup>- CoCoNuT<sup>2</sup> code of the Garching core-collapse supernova group. This code is the general relativistic version (Müller et al., 2010, 2012b, 2013) of the VERTEX code, which is described in detail in Rampp and Janka (2002) and Buras et al. (2006). The code is a hydrodynamic solver with a neutrino radiation transport module. It is capable of multi dimensional simulations. We use it to simulate the gravitational collapse and explosion of a star at the end of its life. Furthermore we can follow the cooling of the so produced proto neutron star.

The GR version of the code is described in great detail also in Müller (2009), we will therefore only sketch the most important equations.

### 2.1 Hydrodynamics

The stellar plasma and the neutron star matter is treated as a fluid with a local velocity  $\vec{v}$ , baryon density  $\rho_B$ , pressure  $p$  and internal energy density  $\epsilon$ . We have to solve the Euler Equations of hydrodynamics, in Newtonian form these are:

$$\frac{\partial}{\partial t} \rho_B + \frac{\partial}{\partial x^i} (\rho_B v^i) = 0, \quad (2.1a)$$

$$\frac{\partial}{\partial t} (\rho_B v_j) + \frac{\partial}{\partial x^i} (\rho_B v_j v^i) + \frac{\partial}{\partial x^j} p = -\rho_B \frac{\partial}{\partial x^j} \Phi + Q_{M_j}, \quad (2.1b)$$

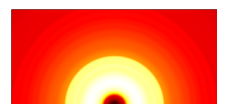
$$\frac{\partial}{\partial t} (\rho_B \epsilon) + \frac{\partial}{\partial x^i} ((\rho_B \epsilon + p) v^i) = -\rho_B v^i \frac{\partial}{\partial x^i} \Phi + Q_E + v^i Q_{M_i}. \quad (2.1c)$$

Note that  $i$  and  $j$  run from 1 to 3. The first equation is the continuity equation followed by the momentum and energy equations.  $p$  and  $\epsilon$  have to be given by an Equation of State (EoS) and  $Q_M$  and  $Q_E$  respectively are the source terms of

---

<sup>1</sup>Variable Eddington factor Radiative Transfer for Supernova EXplosions

<sup>2</sup>Core Collapse with “Nu” (=new) Technology



momentum and energy.  $\Phi$  is the Newtonian gravitational potential. In general, the EoS depends on the chemical composition to determine the pressure  $p$ . Therefore, we also have to account for the advection of the chemical composition of the fluid with equations similar to Eq. (2.1). The net electron fraction  $Y_e$  is defined as the ratio of the net electron per baryon number density,

$$Y_e = \frac{n_{e^-} - n_{e^+}}{n_B}, \quad (2.2)$$

where  $n_{e^-}$ ,  $n_{e^+}$ , and  $n_B$  are the electron, positron and baryon number densities, respectively. As a result of the neutrino transfer, a source term  $Q_N$  arises for  $Y_e$  due to electron flavor neutrino reactions, resulting in

$$\frac{\partial}{\partial t}(\rho_B Y_e) + \frac{\partial}{\partial x^i}(\rho_B Y_e v^i) = Q_N. \quad (2.3)$$

Similarly, for the chemical composition of a nucleus  $k$ ,

$$Y_k = \frac{n_k}{n_B}, \quad (2.4)$$

with source term  $Q_{N_k}$ , one has

$$\frac{\partial}{\partial t}(\rho_B Y_k) + \frac{\partial}{\partial x^i}(\rho_B Y_k v^i) = Q_{N_k}. \quad (2.5)$$

The grav. potential  $\Phi$  in the Euler Eqs. (2.1b) and (2.1c) is the solution of Poisson's Equation,

$$\nabla^2 \Phi = 4\pi G \rho_B. \quad (2.6)$$

In a supernova environment it is possible for the matter to reach very high velocities. Even velocities higher than the speed of light were found in Newtonian codes. Also, a neutron star or a black hole which are the possible results of a core collapse supernova are genuinely relativistic objects. To consider this, we need a relativistic treatment, which is done by the VERTEX-CoCoNuT code.

The Euler Equations in general relativistic form become a little bit more difficult. A perfect fluid can be modelled with two conservation equations: Particle number conservation,

$$\nabla_\mu J^\mu = 0, \quad (2.7)$$

with the baryonic rest mass current  $J^\mu = \rho u^\mu$ ,  $u^\mu$  being the four-velocity, and conservation of energy,

$$\nabla_\mu T^{\mu\nu} = 0, \quad (2.8)$$

where  $T^{\mu\nu}$  is the stress-energy tensor,

$$T^{\mu\nu} = (e + p)u^\mu u^\nu + pg^{\mu\nu}. \quad (2.9)$$

Here  $e = \rho c^2 + \rho\epsilon$  is the total energy density,  $p$  the pressure,  $\rho$  the rest-mass density,  $\epsilon$  the specific internal energy density and  $g^{\mu\nu}$  the metric tensor. Again  $\epsilon$  and  $p$  are



given by the EoS. All variables are measured in the local frame of the fluid and  $\mu, \nu \in \{0, 1, 2, 3\}$ .

To be able to integrate Eqs. (2.7) and (2.8) as well as the evolution equation for the metric numerically, we use the Arnowitt-Deser-Misner (ADM) 3+1 formalism (Arnowitt et al., 2008) for the metric. Note that from here on for the rest of this Chapter we use geometrical units with  $c = G = 1$ .

With that, the four-dimensional line element is set to

$$ds^2 = g_{\mu\nu} dx^\mu dx^\nu = -\alpha^2 dt^2 + \gamma_{ij}(dx^i + \beta^i dt)(dx^j + \beta^j dt), \quad (2.10)$$

where  $\alpha$  is called the lapse function,  $\gamma_{ij}$  the induced three-metric tensor on each hypersurface and  $\beta^i$  the shift vector.

We use the conserved variables defined by Banyuls et al. (1997)

$$D = \rho W \quad \text{rest mass density,} \quad (2.11)$$

$$S^i = \rho h W^2 v^i \quad \text{momentum density,} \quad (2.12)$$

$$\tau = \rho h W^2 - p - \rho W \quad \text{total energy density,} \quad (2.13)$$

where  $h = 1 + \epsilon + p/\rho$  is the specific enthalpy,  $W = 1/\sqrt{1 - v_i v^i}$  is the Lorentz factor and  $v^i = u^i/(\alpha u^0) + \beta^i/\alpha$  is the three-velocity in the Eulerian frame. With that we can finally write down the equations of general relativistic hydrodynamics in flux-conservative form,

$$\frac{\partial}{\partial t}(\sqrt{\gamma}\rho W) + \frac{\partial}{\partial x^i}(\sqrt{-g}\rho W \hat{v}^i) = 0, \quad (2.14a)$$

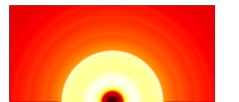
$$\begin{aligned} \frac{\partial}{\partial t}(\sqrt{\gamma}\rho h W^2 v_j) + \frac{\partial}{\partial x^i}(\sqrt{-g}(\rho h W^2 v_j \hat{v}^i + p \delta_j^i)) = \\ \sqrt{-g} T^{\mu\nu} \left( \frac{\partial}{\partial x^\mu} g_{\nu j} - \Gamma_{\mu\nu}^\lambda g_{\lambda j} \right) + \left( \frac{\partial}{\partial t}(\sqrt{\gamma} S_j) \right)_C, \end{aligned} \quad (2.14b)$$

$$\begin{aligned} \frac{\partial}{\partial t}(\sqrt{\gamma}(\rho h W^2 - p - \rho W)) + \frac{\partial}{\partial x^i}(\sqrt{-g}((\rho h W^2 - p - \rho W) \hat{v}^i + p v^i)) = \\ \alpha \sqrt{-g} \left( T^{\mu 0} \frac{\partial}{\partial x^\mu} \ln(\alpha) - T^{\mu\nu} \Gamma_{\mu\nu}^0 \right) + \left( \frac{\partial}{\partial t}(\sqrt{\gamma}(\rho h W^2 - p - \rho W)) \right)_C, \end{aligned} \quad (2.14c)$$

see Müller et al. (2010). Here,  $\sqrt{-g} = \alpha \sqrt{\gamma}$ , with  $\gamma = \det(\gamma_{ij})$ ,  $\hat{v}^i = v^i - \beta^i/\alpha$ ,  $\Gamma_{\mu\nu}^\delta$  are the Christoffel symbols and  $\delta_j^i$  the Kronecker delta.

Like in Eqs. (2.1) the first equation is the continuity equation, followed by the momentum and energy equations.

Also the terms for the evolution equation of the chemical composition change in



general relativistic form to

$$\frac{\partial}{\partial t}(\sqrt{\gamma}\rho W Y_e) + \frac{\partial}{\partial x^i}(\sqrt{-g}\rho W Y_e v^i) = \left( \frac{\partial}{\partial t}(\sqrt{\gamma}\rho W Y_e) \right)_C, \quad (2.15a)$$

$$\frac{\partial}{\partial t}(\sqrt{\gamma}\rho W X_k) + \frac{\partial}{\partial x^i}(\sqrt{-g}\rho W X_k v^i) = 0. \quad (2.15b)$$

Again Eq. (2.15a) is the relativistic version of Eq. (2.3) and Eq. (2.15b) of Eq. (2.5).

The terms which are marked with a subscript ‘‘C’’ in Eqs. (2.14) and (2.15a) are the source terms due to the exchange of momentum and energy with the neutrino field and are explained in Müller et al. (2010) and the next section.

## CFC

To solve the Equations for  $\alpha$ ,  $\beta^i$ ,  $\gamma_{ij}$  we use the Conformal Flatness Condition (CFC) approximation, this is described in detail in Dimmelmeier (2001).

In the CFC approximation we assume that the three-metric  $\gamma_{ij}$  can be approximated as

$$\gamma_{ij} = \phi^4 \hat{\gamma}_{ij} = \begin{pmatrix} \phi^4 & 0 & 0 \\ 0 & \phi^4 r^2 & 0 \\ 0 & 0 & \phi^4 r^2 \sin^2 \theta \end{pmatrix}, \quad (2.16)$$

where  $\phi$  is called the conformal factor. This reduces the number of metric quantities to five,  $\phi$ ,  $\alpha$ ,  $\beta^1$ ,  $\beta^2$ ,  $\beta^3$ . We also demand that CFC is fulfilled instantaneously, which allows us to get rid of the time derivatives. This results in equations for the lapse function  $\alpha$ , the conformal factor  $\phi$ , and the shift vector  $\beta^i$ ,

$$\hat{\Delta}\phi = -2\pi\phi^5 \left( \rho h W^2 - p + \frac{K_{ij}K^{ij}}{16\pi} \right), \quad (2.17)$$

$$\hat{\Delta}(\alpha\phi) = -2\pi\alpha\phi^5 \left( \rho h (3W^2 - 2) + 5p + \frac{7K_{ij}K^{ij}}{16\pi} \right), \quad (2.18)$$

$$\hat{\Delta}\beta^i = 16\pi\alpha\phi^4 S^i + 2K^{ij}\hat{\nabla}_j \left( \frac{\alpha}{\phi^6} \right) - \frac{1}{3}\hat{\nabla}^i \hat{\nabla}_k \beta^k, \quad (2.19)$$

where  $\hat{\Delta}$  and  $\hat{\nabla}$  are the Laplace and covariant derivative operators for a flat three-space,  $K_{ij}$  is the extrinsic curvature and  $S^i = \rho h W^2 v^i$ .

## 2.2 Equation of State (EoS)

Initially the star is well described by an ideal gas, with densities  $\lesssim 10^{10}$  g/cm<sup>3</sup>. Electron and positrons are treated as a Fermi gas with arbitrary degeneracy, and the nuclei are treated as classical Boltzmann gases (Janka, 1999). For higher temperature we also take nuclear reactions into account. We use two different treatments, an approximate burning treatment and an accurate burning network, see Section 2.3. For very high temperatures we assume nuclear statistic equilibrium



**Table 2.1:** Properties of the five EoS we use in our simulations

	$K$	$J$	$L$
LS180	180 MeV	28.62 MeV	73.83 MeV
LS220	220 MeV	28.61 MeV	73.82 MeV
SHEN	281 MeV	36.89 MeV	110.79 MeV
SKA	263 MeV	32.85 MeV	74.53 MeV
WOLFF	263 MeV	32.9 MeV	

(NSE).<sup>3</sup> To calculate this, we use a composition table as described in Buras et al. (2006)

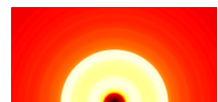
When the star collapses, we reach densities above  $10^{14}$  g/cm<sup>3</sup>. The matter at such high densities involves complicated nuclear physics. This can not be calculated during the simulation. Thus we use high density EoS tables of nuclear physics calculations and lookup the needed quantities. For the high density EoS we use in total five different models. We use two different EoS from Lattimer and Swesty (1991 and Lattimer et al., 1985), with the nuclear incompressibility  $K = 180$  MeV and  $K = 220$  MeV, which are based on a compressible liquid drop model. Additionally we use another EoS from Lattimer (2009), called SKA. Also, we use the EoS from Shen et al. (1998a,b) in the form of Shen et al. (2011), which is based on a relativistic mean field model. Finally, we use also the EoS of Hillebrandt and Wolff (1985), which was calculated by a Hartree-Fock method.

The nuclear parameters of this five EoS are given in Table 2.1, where  $K$  is the nuclear incompressibility parameter,  $J$  the symmetry energy at the saturation density, and  $L$  the logarithmic derivative of the symmetry energy. A detailed description of these properties can be found in e.g. Steiner et al. (2013). In Figure 2.1 we show the Tolmann-Pppenheimer-Volkov (TOV) (Tolman, 1939; Oppenheimer and Volkoff, 1939) solution, that is, the structure equation for a static neutron star configuration in GR, for the five mentioned EoS. Recent observations found a neutron star with a mass of  $\sim 2M_{\odot}$ , (Demorest et al., 2010; Antoniadis et al., 2013). This is a tight constraint for the EoS. We see in Figure 2.1 that the LS180 is the only one of the five EoS that can not fulfil this constraint. But the LS180 was used very often in previous work in the literature and we will therefore use it as well, to be able to do a better comparison with existing results.

In Figure 2.2 we show the sketch of the partitioning of the high and low density EoS setup. Up until the formation of a neutron star we use the schema on the left hand side.  $T_{\text{NSE}}$  is the transition temperature for NSE and is set to 0.776 MeV. The value of  $\rho_{\text{low}}$  depends on the high density EoS we use and is  $\sim 10^{6-8}$  g/cm<sup>3</sup>, the exact values not relevant for the setup. The threshold density  $\rho_{\text{high}}$  is always set to  $10^{11}$  g/cm<sup>3</sup>.

After a neutron star is formed we switch over the scheme on the right hand side

<sup>3</sup>A condition where all nuclear reactions and their inverse reactions happen so fast (on the time scales of the hydrodynamics) that an equilibrium composition is established immediately



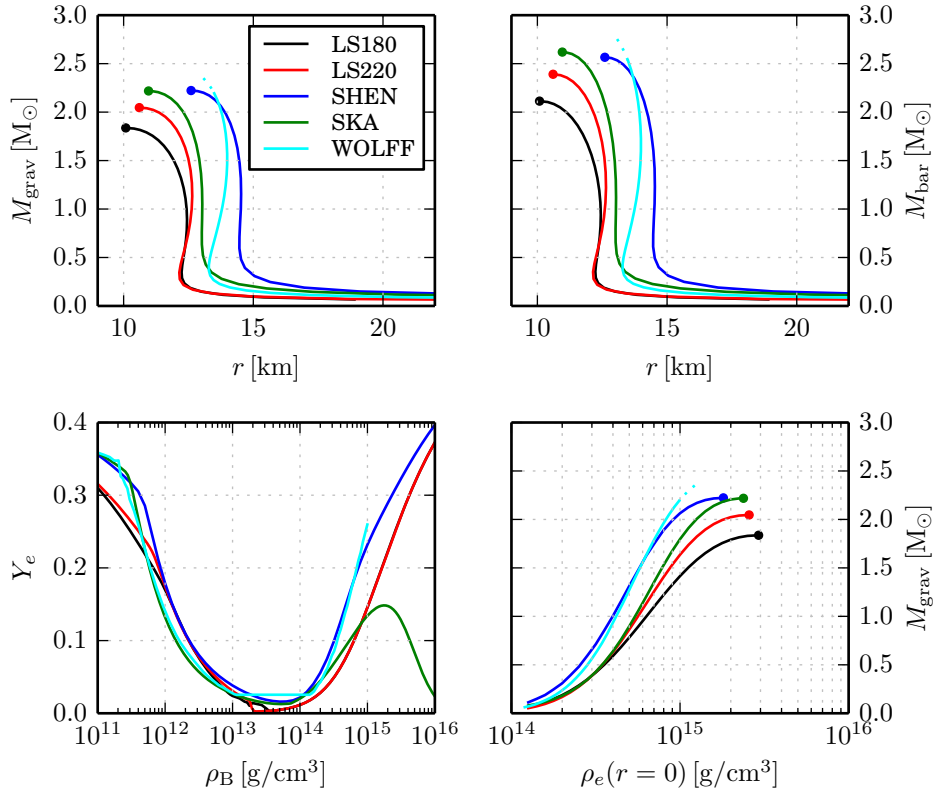


**Figure 2.1:** Mass-radius relation of the five EoS we used is shown in the upper panel, the dot marks the most massive stable configuration. For the WOLFF EoS we could not find a most massive stable configuration in the tabulated region. In the lower panels on the left hand side are the  $\beta$ -equilibrium  $Y_e$  values for a cold configuration (as cold as possible for the irregularly tabulated WOLFF EoS), and the mass central energy-density relation is shown on the right hand side of the lower panel. Image credit: Lorenz HÜdepohl.

of Figure 2.2, where  $T_{\text{NSE}}$  and  $\rho_{\text{high}}$  stay the same. At 30 ms after the neutron star formation we reduce  $T_{\text{NSE}}$  to  $0.4 \text{ MeV}/k_B$  to account for the formation of  $\alpha$ -particles and the so-called  $\alpha$ -effect, see Section 3.6.4.

### 2.3 Nuclear burning treatment

We use two different burning treatments for our simulations. One is an approximate burning treatment described and implemented by Kitaura (2007, Appendix II D). The other one is a full nuclear reaction network, implemented by A. Marek. The approximate burning treatment uses the most important reactions of C12, O16, Ne20, Mg24, and Si28 burning. The network takes all possible reactions between the traced species into account. Both burning treatments use additional electron



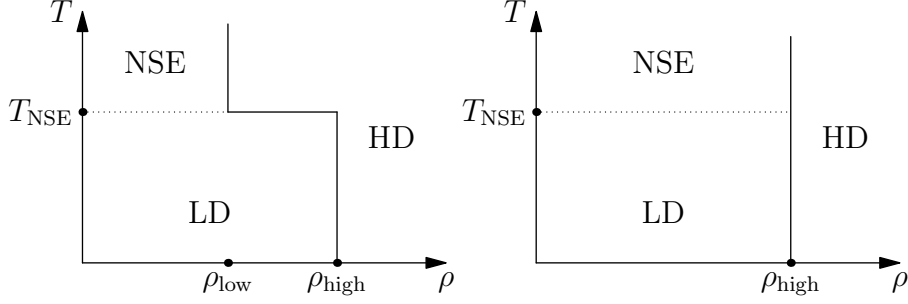


**Figure 2.2:** Two different  $(\rho, T)$  partition used for the different Equation of State partitions used for the simulations. The diagram on the left hand side shows the layout during the collapse, on the right hand side the one used after the formation of the neutron star. During the collapse we use the high density equations of state down to lower densities for high temperatures than in the post collapse phase. The low density regime is further split into, the nuclear statistical equilibrium regime, and an ideal gas regime with the nuclear burning treatment.

capture rates from Takahara et al. (1989).

## 2.4 Neutrino transport

Depending on the density, neutrinos can either be fully trapped in the stellar medium inside the core, interact with the stellar fluid, or at low density travel freely and escape. Therefore, neutrinos have to be treated as radiation and must be calculated using a Boltzmann treatment. In the Newtonian case the Boltzmann equation is:

$$\frac{\partial f}{\partial t} + v_i \frac{\partial f}{\partial x^i} + \left( \frac{dp_i}{dt} \right) \frac{\partial f}{\partial p^i} = C[f], \quad (2.20)$$

where  $C[f]$  is the “collision integral” and  $f(\vec{x}, \vec{p}, t)$  is the particle distribution function of a neutrino species. In our code we only model three kinds of neutrinos:  $\nu_e, \bar{\nu}_e$  and the all heavy lepton neutrinos  $\nu_\mu, \bar{\nu}_\mu, \nu_\tau, \bar{\nu}_\tau$  combined as a single representative species  $\nu_x$ . This is justified as these heavy lepton neutrinos can only interact with the medium by neutral current interactions, as the typical neutrino energies are not enough to create large amounts of muons.

Usually the neutrino intensity  $\mathcal{I}$  is used instead of the neutrino distribution function  $f$ , which is related to  $\mathcal{I}$  as

$$\mathcal{I} = \frac{\varepsilon^3}{h^3 c^2} f. \quad (2.21)$$

With this, we can rewrite Eq. (2.20) to

$$\frac{1}{c} \frac{\partial}{\partial t} \mathcal{I} + \mu \frac{\partial}{\partial r} \mathcal{I} + \frac{1 - \mu^2}{r} \frac{\partial}{\partial \mu} \mathcal{I} = C[\mathcal{I}] \quad (2.22)$$

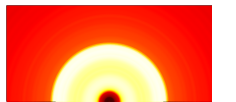


**Table 2.2:** Neutrino interactions as used in our simulations.  $\nu$  stands for any neutrino or anti-neutrino,  $A$  represents heavy nuclei,  $N$  stands for neutrons or protons.

Reaction	References
$\nu e^\pm \rightleftharpoons \nu e^\pm$	Mezzacappa and Bruenn (1993a), Cernohorsky (1994)
$\nu A \rightleftharpoons \nu A$	Horowitz (1997), Bruenn and Mezzacappa (1997)
$\nu N \rightleftharpoons \nu N$	Bruenn (1985), Mezzacappa and Bruenn (1993b), Burrows and Sawyer (1998), Horowitz (2002), Carter and Prakash (2002), Reddy et al. (1999)
$\nu_e n \rightleftharpoons e^- p$	$-n-$ , Burrows and Sawyer (1999)
$\bar{\nu}_e p \rightleftharpoons e^+ n$	$-n-$ , Burrows and Sawyer (1999)
$\nu_e A' \rightleftharpoons e^- A$	Bruenn (1985), Mezzacappa and Bruenn (1993b), Langanke et al. (2003)
$\nu \bar{\nu} \rightleftharpoons e^- e^+$	Bruenn (1985), Pons et al. (1998)
$\nu \bar{\nu} NN \rightleftharpoons NN$	Hannestad and Raffelt (1998)
$\nu A \rightleftharpoons \nu A^*$	Langanke et al. (2008)
$\nu_{\mu,\tau} \bar{\nu}_{\mu,\tau} \rightleftharpoons \nu_e \bar{\nu}_e$	Buras et al. (2003)
$\bar{\nu}_{\mu,\tau} \bar{\nu}_{\mu,\tau} \rightleftharpoons \bar{\nu}_{\mu,\tau} \bar{\nu}_e$	Buras et al. (2003)

where  $\mu = \cos \theta$  is the angle-cosine and  $v_i \frac{\partial}{\partial x^i} = \mu \frac{\partial}{\partial r} + \frac{1-\mu^2}{r} \frac{\partial}{\partial \mu}$  was used. Eq. (2.22) is a complicated integro-differential equation. In order to solve it we take angular moments of Eq. (2.22). We define angular moments of  $\mathcal{I}$

$$\{J, H, K, L, \dots\}(r, t, \varepsilon) = \frac{1}{2} \int_{-1}^{+1} \mu^{\{0,1,2,3,\dots\}} \mathcal{I}(r, t, \varepsilon, \mu) d\mu, \quad (2.23)$$

and take  $\int_{-1}^{+1} \mu^n d\mu$  of Eq. (2.22).

This gives an infinite system of moment equations,

$$\frac{1}{c} \frac{\partial}{\partial t} J + \frac{1}{r^2} \frac{\partial}{\partial r} (r^2 H) = C^{(0)}, \quad (2.24)$$

$$\frac{1}{c} \frac{\partial}{\partial t} H + \frac{1}{r^2} \frac{\partial}{\partial r} (r^2 K) + \frac{1}{r} \cdot (K - J) = C^{(1)}, \quad (2.25)$$

$$\frac{1}{c} \frac{\partial}{\partial t} K + \frac{1}{r^2} \frac{\partial}{\partial r} (r^2 L) + \frac{2}{r} \cdot (L - H) = C^{(2)}, \quad (2.26)$$

where  $C^{(n)}$  denotes the n-th moment of the collision integral. In each equation the next moment appears, therefore the system does not have a closure. We could close the system would we know the Eddington factors

$$f_K = \frac{K}{J} \quad \text{and} \quad f_L = \frac{L}{J}. \quad (2.27)$$

This is achieved in VERTEX by iterating system (2.24) - (2.24) together with a simplified Boltzmann equation, see Rampp and Janka (2002). The neutrino transfer



is coupled to hydrodynamical part via the source terms,

$$Q_E = -4\pi \int_0^\infty d\varepsilon \sum_i C_{\nu_i}^{(0)}(\varepsilon), \quad (2.28)$$

$$Q_M = -\frac{4\pi}{c} \int_0^\infty d\varepsilon \sum_i C_{\nu_i}^{(1)}(\varepsilon), \quad (2.29)$$

$$Q_N = -4\pi m_B \int_0^\infty d\varepsilon \varepsilon^{-1} \left( C_{\nu_e}^{(0)}(\varepsilon) - C_{\bar{\nu}_e}^{(0)}(\varepsilon) \right), \quad (2.30)$$

to the hydrodynamical equations,  $m_B$  is the baryon mass.

The general relativistic transport follows in principle the same concept. As the equations tend to be very long we will only mention the important ones. A detailed explanation can be found in Müller et al. (2010), once again  $G = c = 1$ . We also use the moment definition as in Eq. (2.23), one finds for the first two transport Equations,

$$\begin{aligned} & \frac{\partial W(\hat{J} + v_r \hat{H})}{\partial t} + \frac{\partial}{\partial r} \left[ \left( W \frac{\alpha}{\phi^2} - \beta^r v_r \right) \hat{H} + \left( W v_r \frac{\alpha}{\phi^2} - \beta^r \right) \hat{J} \right] - \\ & \frac{\partial}{\partial \varepsilon} \left\{ W \varepsilon \hat{J} \left[ \frac{1}{r} \left( \beta^r - \frac{\alpha v_r}{\phi^2} \right) + 2 \left( \beta^r - \frac{\alpha v_r}{\phi^2} \right) \frac{\partial \ln \phi}{\partial r} - 2 \frac{\partial \ln \phi}{\partial t} \right] + \right. \\ & W \varepsilon \hat{H} \left[ v_r \left( \frac{\partial \beta^r \phi^2}{\partial r} - 2 \frac{\partial \ln \phi}{\partial t} \right) - \frac{\alpha}{\phi^2} \frac{\partial \ln \alpha W}{\partial r} + \alpha W^2 \left( \beta^r \frac{\partial v_r}{\partial r} - \frac{\partial v_r}{\partial t} \right) \right] - \\ & \left. \varepsilon \hat{K} \left[ \frac{\beta^r W}{r} - \frac{\partial \beta^r W}{\partial r} + W v_r r \frac{\partial}{\partial r} \left( \frac{\alpha}{r \phi^2} \right) + W^3 \left( \frac{\alpha}{\phi^2} \frac{\partial v_r}{\partial r} + v_r \frac{\partial v_r}{\partial t} \right) \right] \right\} - \\ & W \hat{J} \left[ \frac{1}{r} \left( \beta^r - \frac{\alpha v_r}{\phi^2} \right) + 2 \left( \beta^r - \frac{\alpha v_r}{\phi^2} \right) \frac{\partial \ln \phi}{\partial r} - 2 \frac{\partial \ln \phi}{\partial t} \right] - \\ & W \hat{H} \left[ v_r \left( \frac{\partial \beta^r \phi^2}{\partial r} - 2 \frac{\partial \ln \phi}{\partial t} \right) - \frac{\alpha}{\phi^2} \frac{\partial \ln \alpha W}{\partial r} + \alpha W^2 \left( \beta^r \frac{\partial v_r}{\partial r} - \frac{\partial v_r}{\partial t} \right) \right] + \\ & \hat{K} \left[ \frac{\beta^r W}{r} - \frac{\partial \beta^r W}{\partial r} + W v_r r \frac{\partial}{\partial r} \left( \frac{\alpha}{r \phi^2} \right) + W^3 \left( \frac{\alpha}{\phi^2} \frac{\partial v_r}{\partial r} + v_r \frac{\partial v_r}{\partial t} \right) \right] = \alpha \hat{C}^{(0)}, \end{aligned} \quad (2.31a)$$



for the  $J$  Equation and,

$$\begin{aligned}
& \frac{\partial W(\hat{H} + v_r \hat{K})}{\partial t} + \frac{\partial}{\partial r} \left[ \left( W \frac{\alpha}{\phi^2} - \beta^r v_r \right) \hat{K} + \left( W v_r \frac{\alpha}{\phi^2} - \beta^r \right) \hat{H} \right] - \\
& \frac{\partial}{\partial \varepsilon} \left\{ W \varepsilon \hat{H} \left[ \frac{1}{r} \left( \beta^r - \frac{\alpha v_r}{\phi^2} \right) + 2 \left( \beta^r - \frac{\alpha v_r}{\phi^2} \right) \frac{\partial \ln \phi}{\partial r} - 2 \frac{\partial \ln \phi}{\partial t} \right] + \right. \\
& W \varepsilon \hat{K} \left[ v_r \left( \frac{\partial \beta^r \phi^2}{\partial r} - 2 \frac{\partial \ln \phi}{\partial t} \right) - \frac{\alpha}{\phi^2} \frac{\partial \ln \alpha W}{\partial r} + \alpha W^2 \left( \beta^r \frac{\partial v_r}{\partial r} - \frac{\partial v_r}{\partial t} \right) \right] - \\
& \left. \varepsilon \hat{L} \left[ \frac{\beta^r W}{r} - \frac{\partial \beta^r W}{\partial r} + W v_r r \frac{\partial}{\partial r} \left( \frac{\alpha}{r \phi^2} \right) + W^3 \left( \frac{\alpha}{\phi^2} \frac{\partial v_r}{\partial r} + v_r \frac{\partial v_r}{\partial t} \right) \right] \right\} + \\
& (\hat{J} - \hat{K}) \left[ v_r \left( \frac{\beta^r}{r} - \frac{\partial \beta^r}{\partial r} \right) + \frac{\partial}{\partial r} \left( \frac{W \alpha}{\phi^2} \right) - \frac{W \alpha}{r \phi^2} + W^3 \left( \frac{\partial v_r}{\partial t} - \beta^r \frac{\partial v_r}{\partial r} \right) \right] + \\
& (\hat{H} - \hat{L}) \left[ \frac{W^3 \alpha}{\phi^2} \frac{\partial v_r}{\partial r} + \frac{\beta W}{r} - \frac{\partial \beta W}{\partial r} - W v_r r \frac{\partial}{\partial r} \left( \frac{\alpha}{r \phi^2} \right) + \frac{\partial W}{\partial t} \right] - \\
& W \hat{H} \left[ \frac{1}{r} \left( \beta^r - \frac{\alpha v_r}{\phi^2} \right) + 2 \left( \beta^r - \frac{\alpha v_r}{\phi^2} \right) \frac{\partial \ln \phi}{\partial r} - 2 \frac{\partial \ln \phi}{\partial t} \right] - \\
& W \hat{K} \left[ v_r \left( \frac{\partial \beta^r \phi^2}{\partial r} - 2 \frac{\partial \ln \phi}{\partial t} \right) - \frac{\alpha}{\phi^2} \frac{\partial \ln \alpha W}{\partial r} + \alpha W^2 \left( \beta^r \frac{\partial v_r}{\partial r} - \frac{\partial v_r}{\partial t} \right) \right] + \\
& \hat{L} \left[ \frac{\beta^r W}{r} - \frac{\partial \beta^r W}{\partial r} + W v_r r \frac{\partial}{\partial r} \left( \frac{\alpha}{r \phi^2} \right) + W^3 \left( \frac{\alpha}{\phi^2} \frac{\partial v_r}{\partial r} + v_r \frac{\partial v_r}{\partial t} \right) \right] = \alpha \hat{C}^{(1)}.
\end{aligned} \tag{2.32a}$$

for the  $H$  Equation, where the conformal factor  $\phi$ , the lapse function  $\alpha$ , and the radial shift vector  $\beta^r$  are the metric functions from the CFC approximation,  $W$  is again the Lorentz factor.

Also here the Eddington factors  $f_K$  and  $f_L$ , are closing the system. The relativistic form of the source terms in Eqs. (2.14) and (2.15a) is given by

$$\left( \frac{\partial}{\partial t} (\sqrt{\gamma} S_1) \right)_C = \sqrt{\gamma} W (v_r Q_E + Q_M), \tag{2.33}$$

$$\left( \frac{\partial}{\partial t} (\sqrt{\gamma} (\rho h W^2 - p - \rho W^2)) \right)_C = \sqrt{\gamma} W (Q_E + v_r Q_M), \tag{2.34}$$

$$\left( \frac{\partial}{\partial t} (\sqrt{\gamma} \rho W Y_e) \right)_C = \sqrt{\gamma} Q_N. \tag{2.35}$$

with the quantities  $Q_E$ ,  $Q_M$ ,  $Q_N$  from Eqs. (2.28) – (2.30)

The code is capable to do multi dimensional simulations. For that we solve a spherically symmetric problem along each angular ray. Additionally we consider the advection of trapped neutrinos between different rays in the neutron star due to fluid motion. This is called ray-by-ray-plus method, see Buras et al. (2006).



## 2.5 Nucleon potentials

Martínez-Pinedo et al. (2012) and Roberts (2012); Roberts et al. (2012a) detected that in the neutrino nucleon opacities of Burrows and Sawyer (1999) a term with the nucleon mean-field potentials was not considered. This term was therefore also missing in all previous simulations done with the VERTEX and VERTEX-CoCoNuT code. For first simulations with the VERTEX code and the corrected treatment see Hudepohl (2014). Also here we used for most simulations the corrected opacities.

## 2.6 Convection

Simulations in spherical symmetry (1D) can not model non-radial flows. For this reason, they can not simulate truly multidimensional effects such as convection. To compensate, Hudepohl (2014) implemented a mixing length scheme in his thesis to account for the additional matter fluxes due to convection. He could show that with this treatment, the 1D simulations match multidimensional simulations more closely and are especially important for the cooling phase.

For this reason, here we also ported his Newtonian version into the GR hydrodynamics part and use it in some selected models.

In spherical symmetry, a region becomes unstable against convective fluid motions if the Ledoux criterion is positive, that is if

$$C_{\text{led}} = \left( \frac{\partial \rho}{\partial s} \right)_{Y,p} \frac{ds}{dr} + \left( \frac{\partial \rho}{\partial Y} \right)_{s,p} \frac{dY}{dr} \quad (2.36)$$

$$= \frac{d\rho}{dr} - \frac{1}{c_s^2} \frac{dp}{dr} > 0. \quad (2.37)$$

Müller et al. (2010) mentions that this should be modified in the relativistic case to

$$C_{\text{led-GR}} = \frac{d\rho(1 + \epsilon)}{dr} - \frac{1}{c_s^2} \frac{dp}{dr} > 0, \quad (2.38)$$

where  $\rho$  is the density,  $\epsilon$  the specific internal energy density,  $c_s$  the sound speed and  $p$  the pressure. We also implemented this criterion next to the classical expression of Eq. (2.37).

## 2.7 Simulations

In the following Chapters we will compare various models with each other. Table 2.3 give an overview of the names, and their meaning, of our spherically symmetric simulations and Table 2.4 for the axially symmetric simulations.

Additionally, we will add the high density EoS we used to the name of the simulations, if unclear.



**Table 2.3:** Overview of the abbreviation used for the various spherically symmetric models. E bins are the number of energy bins, ML is the mixing length convection method used.

Model	GR	E bins	Nuclear potentials	ML	Nuclear reaction
p-newt	-/-	21	-/-	-/-	Kitaura (2007)
std-12	✓	12	-/-	-/-	Kitaura (2007)
std-21	✓	21	-/-	-/-	Kitaura (2007)
np-12	✓	12	✓	-/-	Kitaura (2007)
con	✓	21	-/-	$C_{\text{led}}$	Kitaura (2007)
r-con	✓	21	-/-	$C_{\text{led-GR}}$	Kitaura (2007)
con-np	✓	21	✓	$C_{\text{led}}$	Kitaura (2007)
r-con-np	✓	21	✓	$C_{\text{led-GR}}$	Kitaura (2007)
net	✓	21	✓	$C_{\text{led}}$	Network
r-net	✓	21	✓	$C_{\text{led-GR}}$	Network

**Table 2.4:** Denotation of the models done for the axially symmetric simulations.

Model	angular bins	angular resolution	Energy bins	Nuclear potentials
128	128	1.44°	12	-/-
np-140	140	1.29°	21	✓
np-280	280	0.64°	21	✓

In the axially symmetric (2D) case the digit always gives the number of angular ( $\theta$ ) zones, measuring the angular resolution. All 2D models were simulated with the VERTEX-CoCoNuT code.

The non-relativistic models were provided to us by Hüdepohl (2009)



## 3 Spherically Symmetric Simulations (1D)

**Pumbaa:** Hey, Timon, ever wonder what those sparkly dots are up there?

**Timon:** Pumbaa, I don't wonder; I know.

**Pumbaa:** Oh. What are they?

**Timon:** They're fireflies. Fireflies that, uh... got stuck up on that big bluish-black thing.

**Pumbaa:** Oh, gee. I always thought they were balls of gas burning billions of miles away.

**Timon:** Pumbaa, with you, everything's gas.

---

*(The Lion King)*

Oxygen-Neon-Magnesium core progenitors are very interesting objects to study. Nomoto (1983) wrote that an ONeMg core star could be a progenitor candidate for the supernova that produced the Crab Nebula, due to the observed abundances. It would produce a low explosion energy and the ejected Ni mass would also be low. For a recent discussion see also Tominaga et al. (2013) and Nomoto et al. (2014). Furthermore, this type of progenitor is the only one where a neutrino-driven explosion does occur already in spherically symmetric simulations. It is possible that supernovae from such stars might make up to  $\approx 30\%$  of all supernovae (Wanajo et al., 2009),

The first, purely hydrodynamic simulations with Nomoto's (1984) ONeMg progenitor were done by Hillebrandt et al. (1984). They obtained a prompt explosion, due to nuclear burning that increased the pressure behind the shock. Later simulations by Burrows and Lattimer (1985) and Baron et al. (1987) could not verify this, in fact they got no explosion at all. Nevertheless, Baron et al. (1987) hinted that neutrino heating might cause an explosion at later times. When Mayle and Wilson (1988) ran their simulations for a longer time, they indeed obtained such an explosion via "late-time neutrino heating". It was discussed that the different outcomes (prompt explosion, no explosion at all, and neutrino-driven explosions) were mostly a result of the different high density neutron star EoS used in the



simulations. Nowadays the supernova community mostly agrees on the viability of the delayed neutrino heating mechanism. Still, the question remained how much impact the high density neutron star EoS has on an electron capture supernovae (ECSNe). Kitaura et al. (2006) used in their simulations two different EoS, a rather soft (LS180) and very stiff (WOLFF) one. They conclude that both simulations lead to a neutrino-driven explosion. In fact even without neutrinos one finds an “explosion”.

The ECSNe kept being of interest as it was suggested that the rapid expansion of the shock surface could be a possible site for the formation of r-process elements. Ning et al. (2007) could produce r-process elements on trajectories on the shocked surface layers, if they assumed favourable conditions for the temperature, density, entropy and electron fraction. Janka et al. (2008), however, could not back that up with their hydrodynamical simulations, as they could never achieve similarly favourable conditions for the r-process as had been assumed by Ning et al. (2007). They conclude that the reason for that is that their simulated shock velocity is much smaller than that assumed by Ning et al. (2007). Therefore, the expansion timescale is too low in order to eject matter with such a high entropy.

The shock region was not the only suggested site for r-process nucleosynthesis. Woosley and Hoffman (1992), Hoffman et al. (1997), Wittl et al. (1994), Takahashi et al. (1994) suggested the neutrino driven wind, an outflow of matter that is lifted by neutrinos leaving the surface of the proto neutron star as it cools. But to confirm this, long-time (longer than 1 s) simulations with detailed neutrino transfer were needed. Such kind of simulations were done by Fischer et al. (2010) and Hüdepohl et al. (2010). Fischer et al. (2010) used the AGILE-BOLTZTRAN code with a full nuclear network and the SHEN EoS to simulate a number of iron and the ONeMg core for over 20 s. Hüdepohl et al. (2010) gave a direct comparison to Fischer et al. (2010) with the VERTEX code and a comparably better neutrino rates treatment. Both groups could not confirm that r-process conditions are present in the neutrino driven wind. Both studies get a proton-rich wind and therefore no r-process is possible. Even though, the neutrino driven wind keeps to be an interesting site, as a weak r-process might still be possible there (Wanajo, 2013; Arcones and Thielemann, 2013). Also, axially symmetric simulations showed that neutron-rich ejecta are possible (Wanajo et al., 2011), due to early convective motions that are able to eject neutron-rich matter more quickly than in 1D simulations, which will be explored in detail in the next Chapter.

Müller et al. (2010) published first 1D results with the ONeMg progenitor and the VERTEX-CoCoNuT code. They compared their results with the simulations done by the post-Newtonian VERTEX version to test the long-time performance of the code. They showed that the effective potential approach of the VERTEX code is in good agreement with the relativistic one and that the VERTEX-CoCoNuT simulations are stable also for long-time runs. We repeat those full relativistic simulations over a longer timespan and also for different EoS. We used these models as a comparison for our models with better resolution and to see the influence of the EoS. Furthermore, we improved our simulations with a corrected nucleon potential



treatment in the neutrino nucleon interactions and in the spherically symmetric case also with a mixing length treatment to approximate multidimensional convection. In some of our simulations we also used a nuclear burning network. All simulations were done with five different EoS that cover a range from very stiff (WOLFF) to soft (LS180).

### 3.1 Progenitor

For all our simulation we use one specific progenitor model, the Oxygen/Neon/Magnesium (ONeMg) core progenitor from Nomoto (1984, 1987). We want to sketch a simplified evolution of this progenitor. Detailed information about the stellar evolution and such kind of stars in general can be found in e.g. Kippenhahn et al. (2012) and references therein.

This star belongs to the so called (Super-)Asymptotic Giant Branch stars (AGB stars). This kind of stars have an initial mass or “zero age main sequence mass” (ZAMS mass) between  $8 - 12 M_{\odot}$  (Siess, 2006). They are the low mass end of star which later undergo core collapse (Janka, 2012).

The structure of such stars is roughly the same, see Figure 3.1a, only the quantitative elemental abundances might differ. AGB stars have H- and He-burning shells

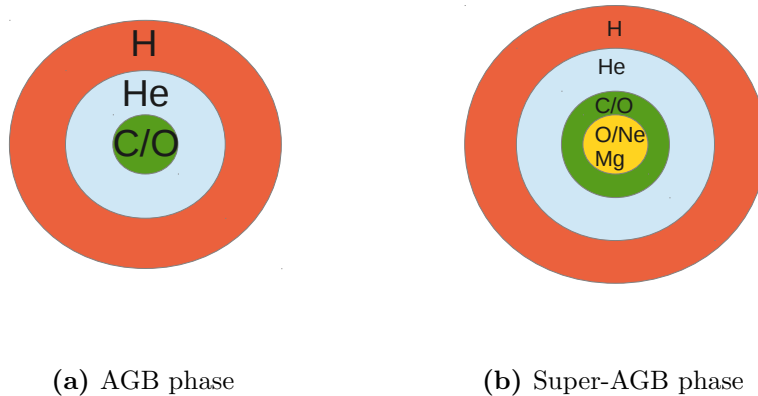


**Figure 3.1:** Composition of a star in the AGB phases

and a Carbon/Oxygen core due to the evolution they went through. SAGB stars can also ignite Carbon and end up with an Oxygen/Neon/Magnesium (ONeMg) core as shown in Figure 3.1b.

The final fate of the star depends on its mass. More massive star can ignite Neon and will probably go through all the nuclear burning stages of a massive star and collapse with an iron core,

In less massive stars, Neon does not ignite and the core becomes strongly electron degenerate (Nomoto, 1984). There, the electrons have to fill every low energy



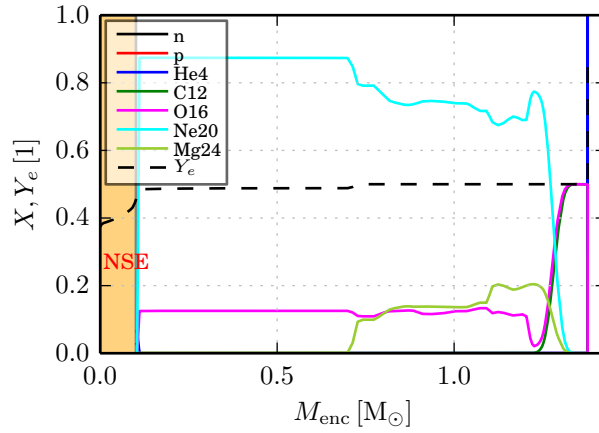
quantum state and additional electrons are forced to fill up quantum states with higher and higher energies, as the same electrons can not occupy the same state due to the Pauli exclusion principle. The resulting degeneracy pressure sustains the core against its gravitational pull. The core still grows as it still accumulates the ashes from the burning shells above. But it can only grow up to a certain critical limit, the so-called “Chandrasekhar Mass”. This limit is reached when the electron degeneracy pressure can not counter the force of gravity any longer. The inner core of the star collapses. Due to the increased density it now becomes favourable for the electrons to combine with the nuclei in electron-capture reactions. The emitted neutrinos from the electron capture reactions carry away energy and lepton number from the core. These electrons are now ”taken away” from the core, the degeneracy pressure is reduced and the core collapses even more rapidly. In the case of the ONeMg core, the most important electron capture reactions are (Nomoto, 1987):



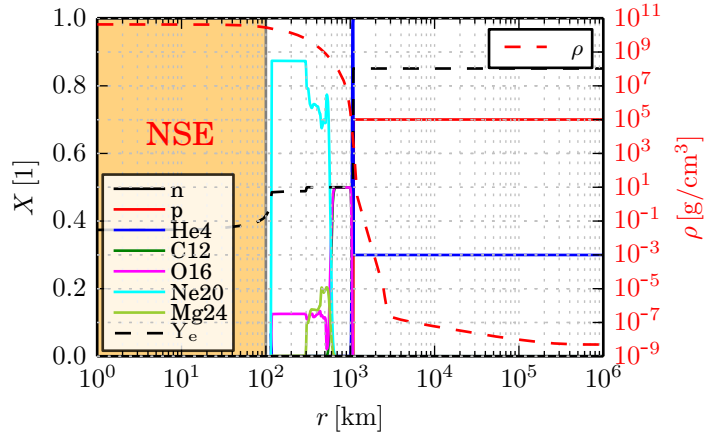
As the core contracts, density and temperature rise and the conditions for Oxygen ignition are reached, the released energy then quickly heats the matter into nuclear statistical equilibrium (NSE). While the nuclear reaction release some amount of energy, they do not halt the collapse, as the velocity of the resulting deflagration front is much smaller compared to the infall velocity (Hillebrandt et al., 1984). Actually, it can even accelerate the collapse, as electrons can now also be captured on the ensemble of newly present elements in the NSE composition.

Figure 3.2 shows the initial mass fraction and electron fraction  $Y_e$  using the enclosed mass as a radial coordinate of the progenitor we use.  $Y_e$  shows two drops due to previous electron captures, the drop is more prominent in the NSE region as there are more elements available which can capture electrons. In comparison to that Figure 3.3 shows a profile of the mass fraction and density as a function of radius.





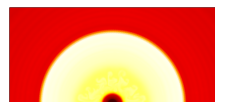
**Figure 3.2:** Initial composition and electron fraction  $Y_e$  of the ONeMg progenitor. The orange shaded region marks the area where the matter is in NSE.



**Figure 3.3:** Profile of the initial mass fraction and density. The orange shaded area marks the NSE region.

One can see that most of the mass of the star is contained in its very compact ( $\sim 1000$  km) ONeMg core. On the right y-axis, the steep density profile is also shown. A sharp drop in density over many orders of magnitude separates the ONeMg core from the H/He hull.

The stellar evolution of such stars is very difficult to model due to complicated processes happening there, such as dredge-ups, flashes, stellar winds and the accompanied nuclear reactions, see Siess (2006) for an exemplary evolution of an  $9.5 M_{\odot}$  star. Thus, there are not a lot of progenitors published in the literature that have been modelled up until the point of gravitational collapse. The one of Nomoto (1984, 1987) is currently the only one available to us.



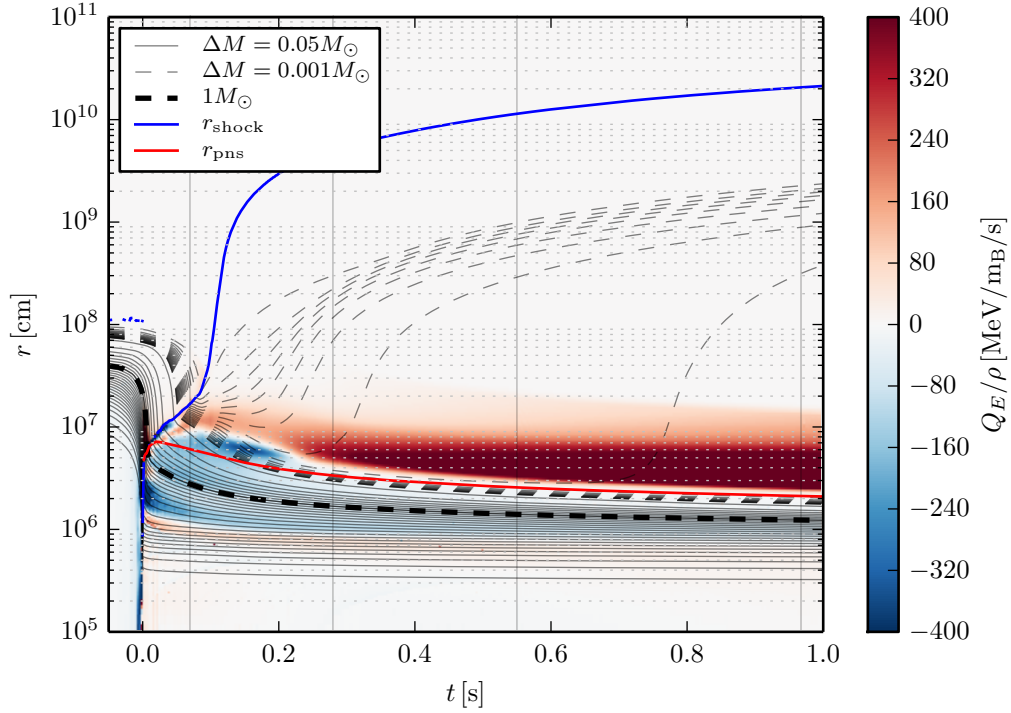


**Figure 3.4:** Evolution of mass shells over time for the SHEN std-12 model. Colour coded is the net neutrino heating (reddish) or cooling (bluish) over time. The time is normalized to the moment of core bounce. The solid grey lines indicate mass shells separated by  $0.05 M_{\odot}$ , the dashed thick black line marks one solar mass and the dashed grey lines above  $1.36 M_{\odot}$  are separated by  $10^{-3} M_{\odot}$ . The red line is the proto neutron star radius, here defined as the density contour of  $10^{11} \text{ g/cm}^3$ . The shock radius is marked with a blue line.

## 3.2 Overview

Figure 3.4 gives an overview about the first second. As the behaviour is similar in all our simulations we use a spherical symmetric (1D) simulation with the SHEN EoS as an example. The figure shows the evolution of selected mass shells, and colour coded the neutrino heating rate. From the time  $-0.05 \text{ s}$  to  $0.0 \text{ s}$  the inner mass shells are falling down, the inner core of the star is collapsing. During that phase the nuclei in the core get compressed till nuclear density ( $\rho_{nuc} \approx 2.7 \cdot 10^{14} \text{ g/cm}^3$ ) is reached. Then, heavy nuclei dissolve into individual nucleons and the core becomes a proto neutron star (PNS). The increasing pressure of the nuclear matter stops the collapse. The core gets compressed a little bit more and bounces back, this creates a shock wave, which travels out through the still in-falling matter.

Table 3.1 gives an overview of the different shock radii, enclosed masses and the collapse duration for the different available models at bounce time. The difference between the std-12 and np-12 model to the con-np and net model is mainly due



**Table 3.1:** Various quantities at the moment of bounce, the shock radius ( $r_{\text{sh}}$ ), the enclosed mass ( $M_{\text{sh}}$ ) and the collapse duration  $t_{\text{col}}$ .

Model	LS180		
	$r_{\text{sh}}$ [km]	$M_{\text{sh}}$ [ $M_{\odot}$ ]	$t_{\text{col}}$ [s]
con-np-1D	10.23	0.414	0.061
np-12-1D	10.08	0.410	0.059
r-con-np-1D	10.24	0.414	0.061
std-12-1D	10.12	0.411	0.059
std-21-1D	10.26	0.412	0.062

Model	LS220		
	$r_{\text{sh}}$ [km]	$M_{\text{sh}}$ [ $M_{\odot}$ ]	$t_{\text{col}}$ [s]
con-np-1D	10.09	0.427	0.060
np-12-1D	10.04	0.422	0.059
r-con-np-1D	10.03	0.426	0.060
std-12-1D	10.16	0.427	0.059
std-21-1D	10.08	0.421	0.061

Model	SHEN		
	$r_{\text{sh}}$ [km]	$M_{\text{sh}}$ [ $M_{\odot}$ ]	$t_{\text{col}}$ [s]
con-np-1D	11.06	0.485	0.060
np-12-1D	11.19	0.488	0.058
r-con-np-1D	11.06	0.485	0.060
std-12-1D	11.08	0.486	0.059
std-21-1D	11.09	0.484	0.060

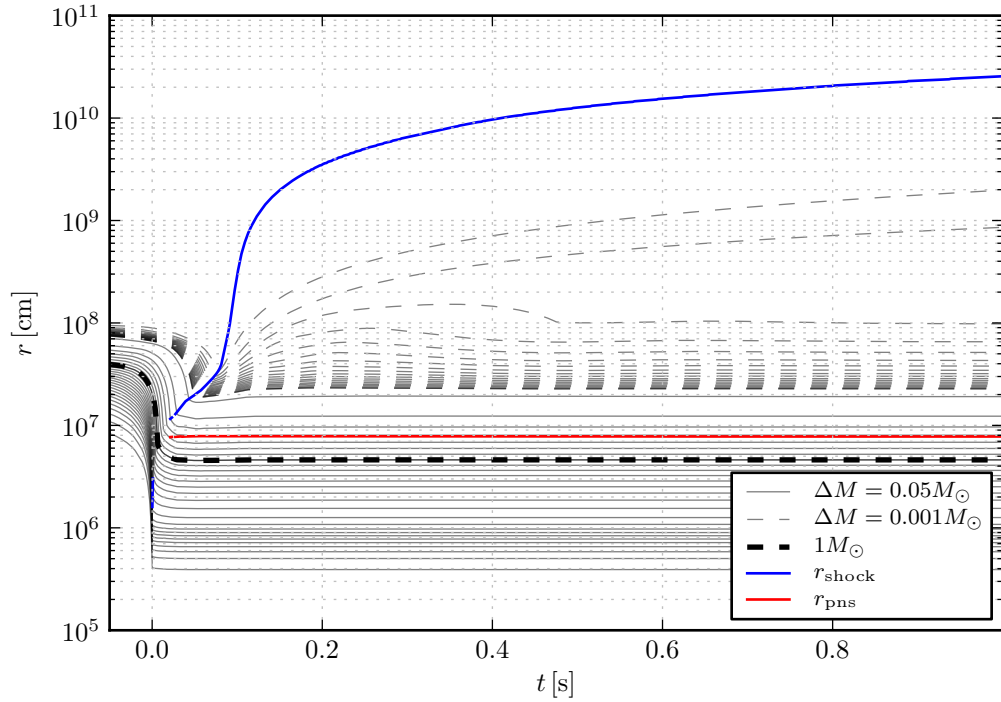
  

Model	SKA		
	$r_{\text{sh}}$ [km]	$M_{\text{sh}}$ [ $M_{\odot}$ ]	$t_{\text{col}}$ [s]
con-np-1D	10.62	0.494	0.062
np-12-1D	10.57	0.494	0.061
r-con-np-1D	10.58	0.493	0.062
std-12-1D	10.58	0.494	0.061
std-21-1D	10.61	0.492	0.063

Model	WOLFF		
	$r_{\text{sh}}$ [km]	$M_{\text{sh}}$ [ $M_{\odot}$ ]	$t_{\text{col}}$ [s]
con-np-1D	12.05	0.467	0.070
np-12-1D	11.94	0.466	0.067
r-con-np-1D	12.02	0.467	0.070
std-12-1D	12.08	0.467	0.068
std-21-1D	12.11	0.467	0.071





**Figure 3.5:** Similar to Figure 3.4 but without neutrino transport, therefore no neutrino heating and cooling. Note that also here the shock travels outwards, however, not all of the matter behind it is ejected, but will fall back at some point.

to their different energy resolution, see Section 3.3.

From 0s to around 0.1s the outer layers of the star are falling through the shock, whereby the heavy nuclei get photodissociated into nucleons. We saw in Figure 3.3 that the density profile of the star is very steep. Therefore, there is not enough infalling matter to hold the outwards movement of the shock. Once the shock passes the steep gradient it can move out freely.

The outer shells of the star get accreted onto the PNS while releasing their binding energy in the form of neutrinos. Meanwhile, neutrinos from the surface of the PNS get released. Those neutrinos carry away energy from the PNS and are able to deposit some of it on matter behind the shock. This neutrino heating region is the red shaded area in Figure 3.4. From around 0.08s on we can see that these heated layers expand, leading to an explosion. The blue shaded areas indicate neutrino cooling, where the neutrinos take away energy by leaving the system. For more details on this neutrino driven explosion mechanism, see e.g. Janka (2001).

As a comparison we show in Figure 3.5 a similar plot of a 1D simulation with the SHEN EoS, but without any neutrino interactions allowed after the formation of the proto neutron star. Again, the grey and black lines represent different enclosed masses and red and blue are the PNS and shock radius, respectively. Due to the



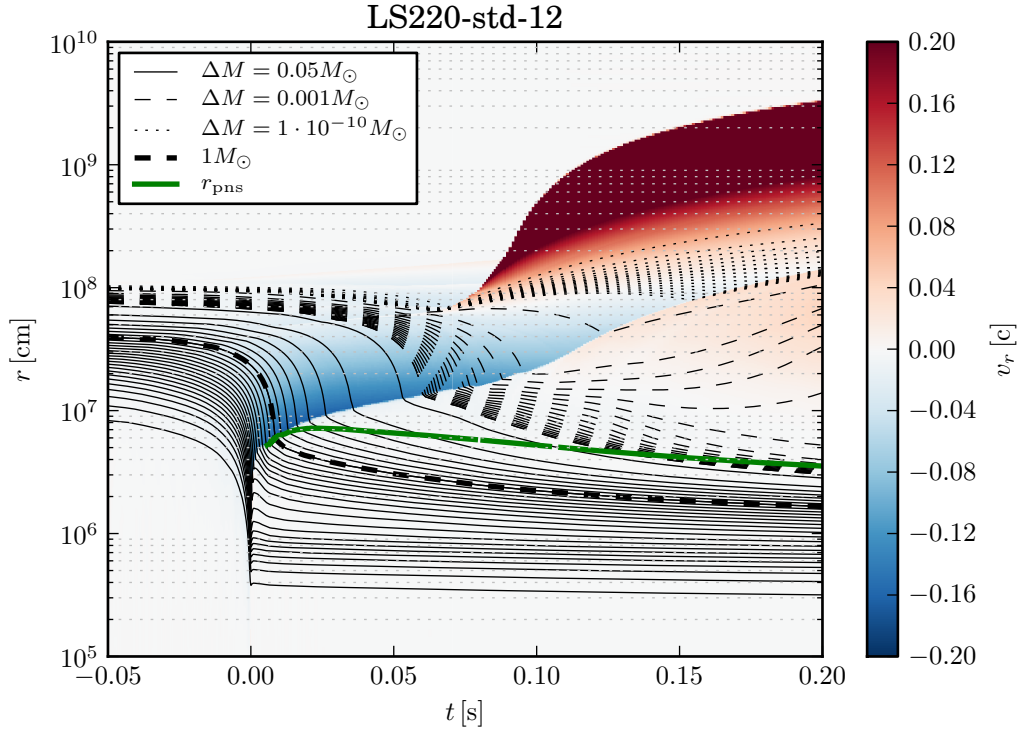


**Figure 3.6:** Evolution of mass shells over the time of the std-12 model with the LS220 EoS. Colour coded is the radial velocity over time. The green line it the proto neutron star radius.

fact there a no neutrinos leaving the PNS it can not cool down and stays hot and expanded. Also the shock on it's own is not enough to trigger a explosion as indicated by the still down-falling mass shells. Some matter gets blown away with the shock but it is not enough to explode all of the outer hull of the star or to attain similar explosion energies as with neutrino heating.

We found that the evolution of the collapse is very unstable against small changes. An example of a peculiar case is shown in Figure 3.6, where we colour coded the radial velocity. We see two separated regions with outwards movement, one behind the shock tat formed at the birth of the proto neutron star, resulting in the explosion we also saw in Figure 3.4. The other one starts around 0.06 s, where the increased velocities of the outer shell show another outwards moving shock. We find that this second shock front comes from explosive burning of the intermediate mass elements, such as Mg and Si. This effect occurred in some of our simulations with the LS220 EoS and in most of the simulation done with the full burning network. We find that slight adjustments of typically inconsequential numerical parameters or even the use of different compiler or compiler version can trigger or inhibit this apparently chaotic phenomenon.



### 3.3 Resolution study

Marek (2007) pointed out that it is always nice to know that your simulations are stable against changes in the numerical resolution. In our simulations with the VERTEX-CoCoNuT code the most important dimensions are firstly the grid in neutrino energy space, secondly the grid in radial direction, and thirdly – for the axially symmetric (2D) simulations – the angular grid. In this section we will discuss the effect of changing the first two on the basis of the neutrino signal. The 2D case will be discussed in Section 4.1.

The neutrino luminosity is the total amount of neutrino energy emitted through a spherical surface per unit time. Also of interest is the neutrino mean energy, which is defined as the ratio of neutrino energy density  $J$  over neutrino number density  $\mathcal{J}$ ,

$$\langle \varepsilon \rangle = \frac{\int J d\varepsilon}{\int \mathcal{J} d\varepsilon} = \frac{\int_0^\infty d\varepsilon \int_{-1}^1 d\mu \mathcal{I}(\varepsilon, \mu)}{\int_0^\infty d\varepsilon \int_{-1}^1 d\mu \varepsilon^{-1} \mathcal{I}(\varepsilon, \mu)}, \quad (3.5)$$

where  $\mathcal{I}$  is the neutrino intensity.

#### 3.3.1 Energy resolution

The energy grid consist of geometrically spaced energy bins over the energy range of 0 MeV – 380 MeV. Mostly, the VERTEX-CoCoNuT simulations are done with 12 energy bins, as the relativistic treatment is already computationally expensive. But for a better comparison with the non-relativistic simulations from Hüdepohl et al. (2010), see Section 3.4.1, we also performed simulations with 21 energy bins. Figure 3.7 shows the resulting neutrino signal for different EoSs. All quantities were taken at a radius of 500 km and we considered the redshift to infinity and the doppler shift from the co-moving frame. On the left hand side we see the luminosities and on the right hand side the mean energies. The  $L_{\nu_e}$  has a local maximum peak even before the core bounce, we concur with Hüdepohl (2014) that this peak comes from a semi-transparent region before the proto neutron star is formed. This first maximum is followed by the  $\nu_e$  breakout burst, when the neutrinosphere becomes transparent for the electron neutrinos. When we analyse the model with 21 energy bins (std-21) and the model with 12 energy bins (std-12) we see, that the luminosity signal is very similar up to the time of bounce. After that, the std-21 model shows a higher electron neutrino burst than the 12 bin model. The  $L_{\bar{\nu}_e}$  and  $L_{\nu_x}$  look the same for the first 50 ms.

The mean energies differs visibly before the time of bounce. Note that only the mean energies of the electron neutrinos are well defined during collapse, as there are practically no  $\bar{\nu}_e$  and  $\nu_x$  neutrinos emitted during that time. After bounce the  $\langle \varepsilon_{\nu_e} \rangle$  of the 21 bin model is higher than in the 12 bin case. The  $\langle \varepsilon_{\bar{\nu}_e} \rangle$  shows the same behaviour. The  $\langle \varepsilon_{\nu_x} \rangle$  of the std-21 model on the other hand is for a short moment after bounce lower than in the std-12 model, till it also gets higher. Theses effects are seen in all five EoS shown in Figure 3.7. We indicated already that the



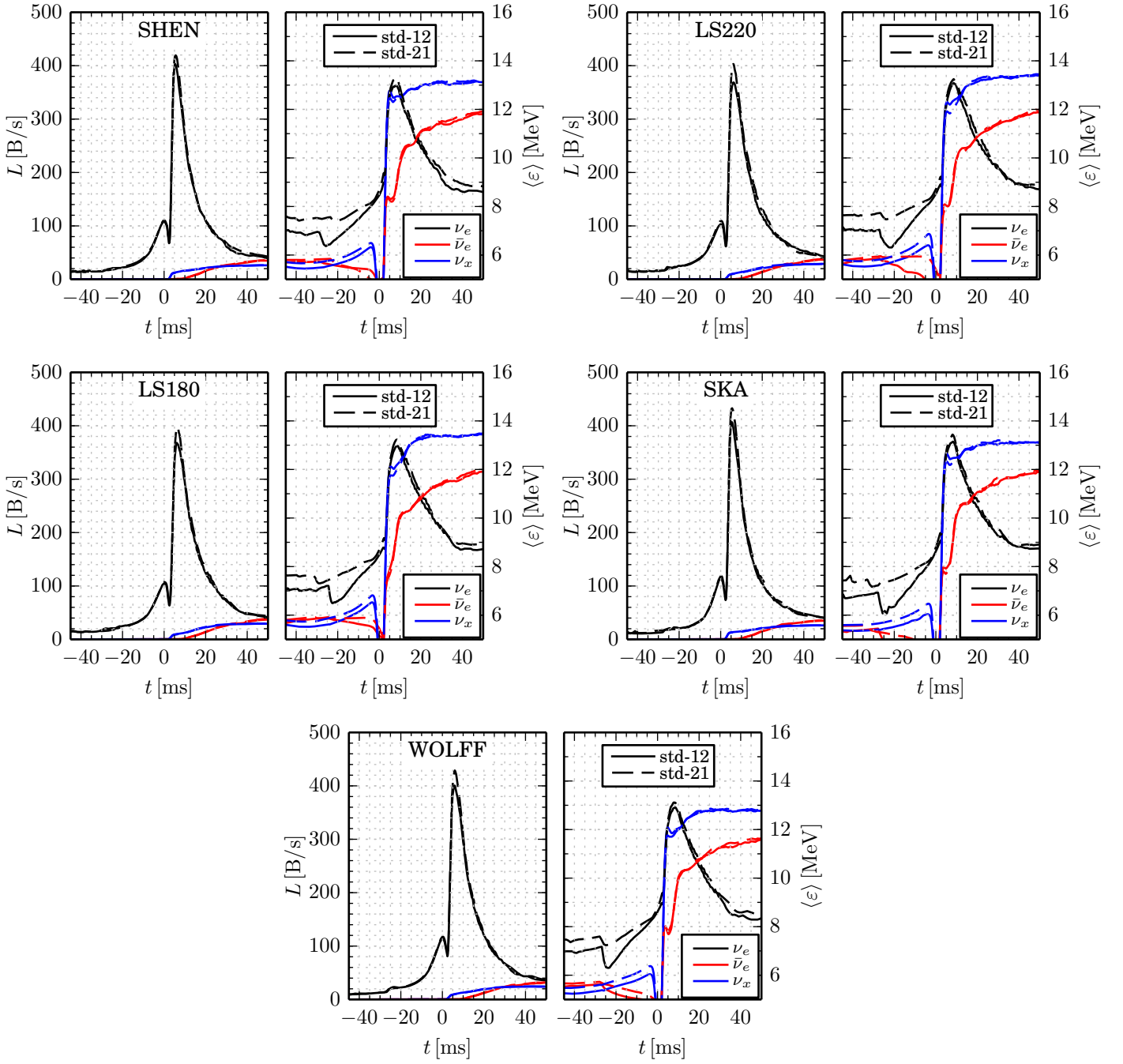


**Figure 3.7:** Comparison of the neutrino signal for simulations for the first 50 ms with different numbers of energy bins and for all five EoSs. On the right hand side, of each panel, is the neutrino luminosities and on the left hand side the neutrino mean energies. The colours represent the neutrino species, electron neutrinos  $\nu_e$  (black), anti-electron neutrinos  $\bar{\nu}_e$  (red) and heavy-lepton neutrinos  $\nu_x$  (blue).



energy resolution has some effect on the collapse duration. Therefore, we compare std-12 and std-21 model in more detail. In Table 3.1 the influence of the number of energy bins on to the collapse time and the shock formation radius as well as the enclosed mass at that time can be seen. The strongest effect is visible in the collapse time, which can vary around 1 – 3 ms depending on the resolution. The enclosed mass and the shock radius at the moment of bounce stay roughly the same, however.

We also wanted to see if the resolution has any affect on a longer timescale. Figure 3.8 therefore shows the neutrino signal up to 4 s post-bounce for models with four different EoS, and 2.5 s post-bounce for the models with the WOLFF EoS in Figure 3.9.

For the luminosities we do not see a huge difference. Only if we look very closely we see that the luminosities for the electron and anti-electron neutrinos are minimally higher for the 21 energy bin model than for the 12 energy bin model, whereas the luminosities for the heavy lepton neutrinos of the 21 energy bin model are lower. For the energies, we actually can see a difference. We see the strongest effect for the heavy lepton neutrinos, where the std-21 model has lower energies than the std-12 model. The same is true for the anti-electron energies. The electron neutrino energies of both models are very close. But we see that the model with the 21 energy bins has a slightly higher mean energy than the 12 energy bin model. This is found for all the Equations of State, shown in Figures 3.8 and 3.9.

To quantitatively assess the impact of the higher energy resolution, we compare in Tables 3.2 and 3.3 the time averaged neutrino parameters after a few seconds for these models. Shown are the neutrino mean energies whose time evolution we saw in the figures before, the number of emitted neutrinos  $N$ , and the cumulatively emitted total neutrino energy  $E$ , which is defined as

$$E_{\nu}^{\text{tot}}(t) = \int_{-\infty}^t L_{\nu}(t') dt'. \quad (3.6)$$

We see that all in all the relative changes stay within 3% at worst. The total emitted electron neutrino energy  $E_{\nu_e}$  shows the highest difference between the 21 and 12 energy bin models.

The transport of our code is already quite expensive, therefore simulations with a lower number of energy bins are thus acceptable, although simulations with higher energy bins are certainly preferred. We simulated most of our simulations with 21 energy bins. As those models are computational more expensive, and evolve slower than models with 12 energy bins, we continued the models that had been set-up with 12 energy bins. Especially the models with the corrected nucleon potentials, because we were interested in the late time effect of those models in particular.

### 3.3.2 Radial resolution

For the ONeMg progenitor we also need to have a good radial resolution to represent the steep density profile of the star, see Figure 3.3. Therefore, we already use more



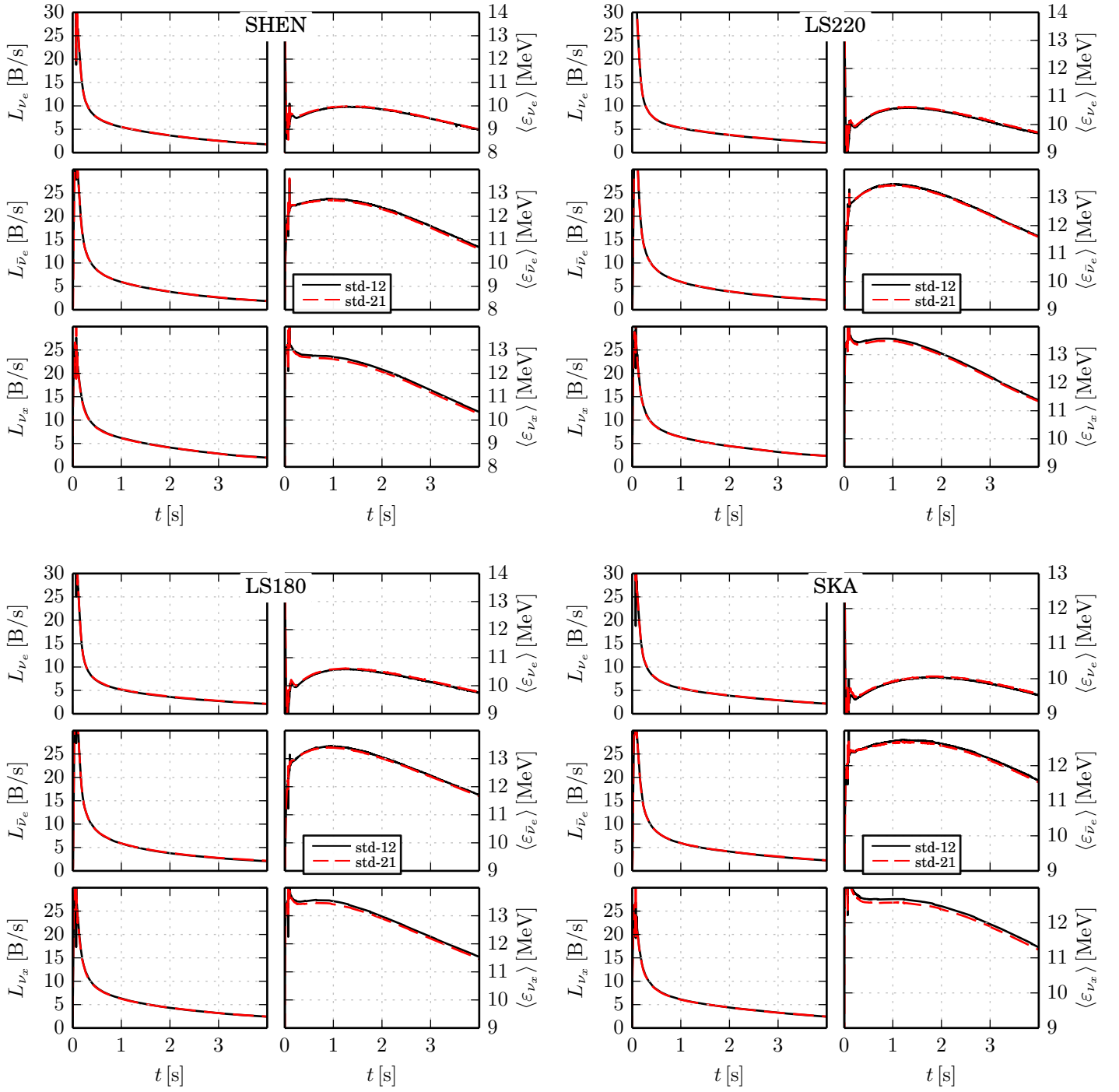


**Figure 3.8:** Similar to Figure 3.7 but for the first 4 seconds post-bounce. The upper panels in each sub plot show the electron neutrinos, the middle the anti-electron neutrinos, and the lower the heavy lepton neutrinos.



**Table 3.2:** Time averaged neutrino mean energies and total number of emitted neutrinos for the first four seconds after bounce, for four EoSs and the models with 12 and 21 energy bins. Note that to get the total emitted neutrino number/energy one has to weight the  $\nu_x$  with a factor of four, as they only represent one of the four heavy lepton neutrino kinds ( $\nu_\mu, \bar{\nu}_\mu, \nu_\tau, \bar{\nu}_\tau$ ).

Model	LS180								
	$\langle \varepsilon \rangle_{\nu_e}$	$\langle \varepsilon \rangle_{\bar{\nu}_e}$	$\langle \varepsilon \rangle_{\nu_x}$	$N_{\nu_e}$	$N_{\bar{\nu}_e}$	$N_{\nu_x}$	$E_{\nu_e}$	$E_{\bar{\nu}_e}$	$E_{\nu_x}$
	[MeV]			$[10^{57}]$			[B]		
std-12-1D	10.1	12.8	13.1	1.68	1.08	1.08	27.2	22.2	22.8
std-21-1D	10.2	12.8	13.0	1.69	1.09	1.09	27.8	22.4	22.7

Model	LS220								
	$\langle \varepsilon \rangle_{\nu_e}$	$\langle \varepsilon \rangle_{\bar{\nu}_e}$	$\langle \varepsilon \rangle_{\nu_x}$	$N_{\nu_e}$	$N_{\bar{\nu}_e}$	$N_{\nu_x}$	$E_{\nu_e}$	$E_{\bar{\nu}_e}$	$E_{\nu_x}$
	[MeV]			$[10^{57}]$			[B]		
std-12-1D	10.1	12.9	13.1	1.70	1.09	1.09	27.6	22.5	22.9
std-21-1D	10.2	12.8	13.0	1.71	1.10	1.09	28.1	22.6	22.8

Model	SHEN								
	$\langle \varepsilon \rangle_{\nu_e}$	$\langle \varepsilon \rangle_{\bar{\nu}_e}$	$\langle \varepsilon \rangle_{\nu_x}$	$N_{\nu_e}$	$N_{\bar{\nu}_e}$	$N_{\nu_x}$	$E_{\nu_e}$	$E_{\bar{\nu}_e}$	$E_{\nu_x}$
	[MeV]			$[10^{57}]$			[B]		
std-12-1D	9.7	12.2	12.4	1.74	1.11	1.08	27.0	21.8	21.4
std-21-1D	9.8	12.2	12.3	1.75	1.12	1.08	27.5	21.9	21.3

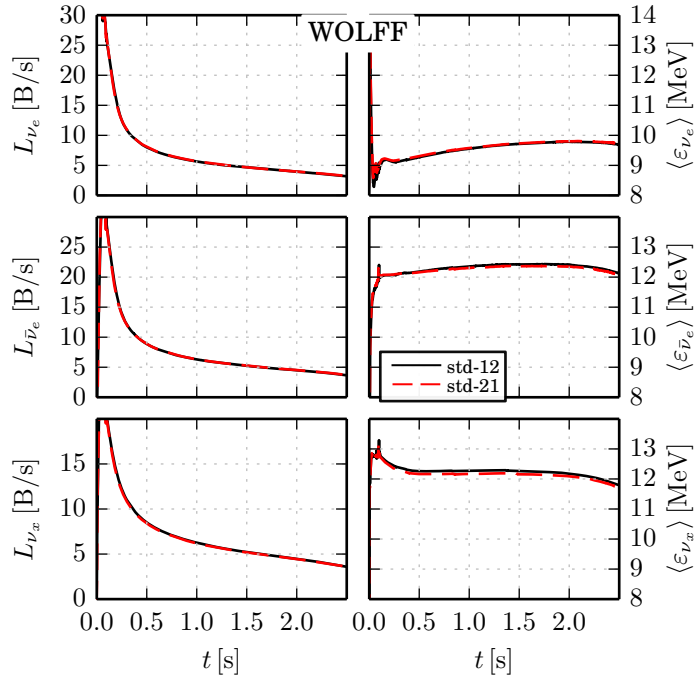
  

Model	SKA								
	$\langle \varepsilon \rangle_{\nu_e}$	$\langle \varepsilon \rangle_{\bar{\nu}_e}$	$\langle \varepsilon \rangle_{\nu_x}$	$N_{\nu_e}$	$N_{\bar{\nu}_e}$	$N_{\nu_x}$	$E_{\nu_e}$	$E_{\bar{\nu}_e}$	$E_{\nu_x}$
	[MeV]			$[10^{57}]$			[B]		
std-12-1D	9.8	12.4	12.5	1.75	1.13	1.11	27.5	22.5	22.2
std-21-1D	9.9	12.4	12.4	1.77	1.14	1.11	28.0	22.6	22.1

**Table 3.3:** As Table 3.2 but only for the first 2.5 s for the models with the WOLFF EoS.

Model	$\langle \varepsilon \rangle_{\nu_e}$	$\langle \varepsilon \rangle_{\bar{\nu}_e}$	$\langle \varepsilon \rangle_{\nu_x}$	$N_{\nu_e}$	$N_{\bar{\nu}_e}$	$N_{\nu_x}$	$E_{\nu_e}$	$E_{\bar{\nu}_e}$	$E_{\nu_x}$
	[MeV]			$[10^{57}]$			[B]		
	std-12-1D	9.5	12.2	12.3	1.59	0.97	0.89	24.2	18.9
std-21-1D	9.7	12.2	12.3	1.59	0.97	0.89	24.7	18.9	17.4





**Figure 3.9:** As Figure 3.8 but for the WOLFF EoS.

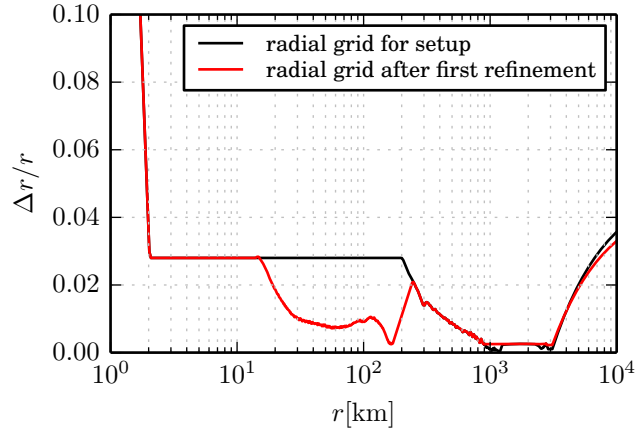


**Figure 3.10:** Radial resolution for the first two grids used in our simulations. The black line shows the initial radial resolution of all our models. The red line gives an example of a possible first grid refinement.

radial zones than is common for other progenitors. In our case we simulate all models with 1400 radial zones initially. The radial resolution  $\Delta r/r$  is shown in Figure 3.10. We made some tests with an even higher radial resolution using 1600 zones and 1800 zones, which did however not change the results measurably.



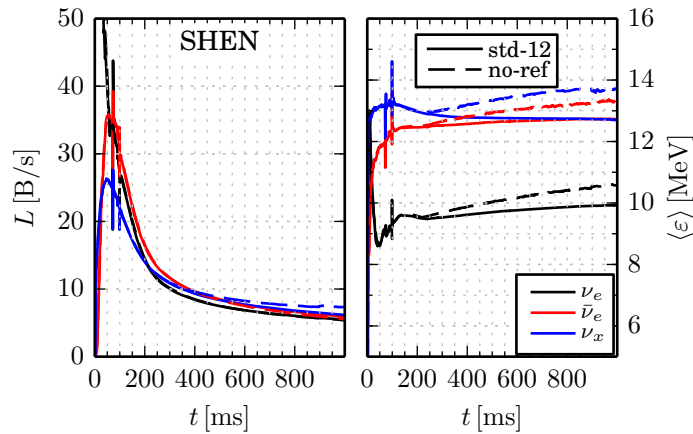


**Figure 3.11:** Comparing the neutrino luminosities and mean energies of a model which was refined when needed (solid lines) with one which was not refined at all (dashed lines), on the bases of the SHEN EoS. The values were extracted at 500 km and transformed into a resting observer’s frame.

As the simulation progresses, the proto neutron star shrinks. Therefore, we have again a steep density profile which we want to resolve as best as possible, considering also that this is the region most important for the transport of the escaping neutrinos. To achieve this we have to refine our radial grid periodically as the simulation progresses. An example of such a refinement is also illustrated in Figure 3.10. We found that it has a great effect if we do not refine the simulations, see Figure 3.11, where we compare a model which we refine when ever found necessary, and a model which we did not refine at all during the simulation. We see that the luminosities and energies of the unrefined model starts to rise above the refined model, at a certain point. This sharp rise is clearly an unphysical behaviour. We usually refine our models the first time around 70 ms post-bounce, which is way before the time we see first resolution effects ( $\approx 200$  ms). Note also that all curves show a small irregularity at around 0.07 s. This is due to a numerical artefact and visible in all our models: When the shock front passes through 500 km, where we typically evaluate the neutrino signal, the velocities there get very high and when we then transform the co-moving neutrino signal into the observer frame, slight inaccuracies in the transformation are greatly amplified.

We can safely say that 1400 radial zones at the beginning of the simulation are reasonable and the radial grid should be refined during the simulation as often as needed in order to resolve the neutron star’s surface.

### 3.4 Early Phase

The Neutrino signal is the first and possibly only sign we might get from a core collapse supernova. Neutrinos also play an important role for the explosion of the



star. For the famous supernova SN1987A, several neutrino events were detected, eleven by Kamiokande II (Hirata et al., 1987), eight in the IMB water-Cherenkov detector (Bionta et al., 1987) and possibly also five from the Baksan scintillator detector (Alexeyev et al., 1988). These events occurred before the first photons from SN1987A were visible, as it takes hours to days for the shock wave to reach the visible surface of the star. Currently running detectors are even linked together in the SuperNova Early Warning System (SNEWS) in order to alert astronomers in advance when a galactic supernova happens. Future detectors are planned which could even detect a neutrino signal beyond the Milky Way (Scholberg, 2007). As ECSN could make up to  $\approx 30\%$  of all supernova (Wanajo et al., 2009), it is interesting what kind of neutrino signal one could expect from them.

In this section we will investigate the neutrino signal for the first 500 ms for different models, starting with the comparison between our GR models with the post-Newtonian models from H udepohl (2009). Then, we will concentrate purely on our GR models and demonstrate the evolution of our models as we include more and more relevant physics, step by step.

### 3.4.1 GR vs. Post-Newton

We want to do a comparison of models with and without GR to see the effects from the fully relativistic treatment, when using similar neutrino physics. To do so, Lorenz H udepohl kindly provided us with his simulation data from H udepohl (2009). They are simulated with the VERTEX code and a pseudo relativistic potential, to mimic the most important effects of a general relativistic potential, which also includes simulations for the LS180, SHEN and SKA EoS. The initial set-up was done with 1600 radial zones and 21 energy bins. We will compare those to our 21 energy bin simulations with the fully relativistic treatment. We saw in Section 3.3.2 that the difference of the radial zones between H udepohl (2009) and our simulation has no effect.

First of all, the most visible improvement is the velocity. M uller et al. (2010) already stated that in the post-Newtonian simulations the shock gets accelerated over the steep density profile so fast that it reaches velocities way above the speed of light. Therefore, also the shock radius is higher as illustrated in Figure 3.12. On the left hand side we see the velocity evolution over time and on the right the shock radius as it moves outwards for the GR and the post-Newtonian simulations. In the post-Newtonian case we get maximum velocities of  $5.3c$ , whereas in the GR case the velocities obviously stay always below  $c$ , as expected.

The influence on the neutrino signal is less pronounced. In Figure 3.13 we show the first 500 ms of the neutrino signal for all available EoS. In the top panel of all figures the electron neutrinos are shown, followed by the anti-electron neutrinos in the middle and the heavy lepton neutrinos at the bottom. On the left hand side are always the luminosity and on the right hand side the mean energy. All in all the neutrino signal of the GR simulations are all at a slightly lower level than those on of the post-Newtonian ones. Also the neutron star radius is lower,



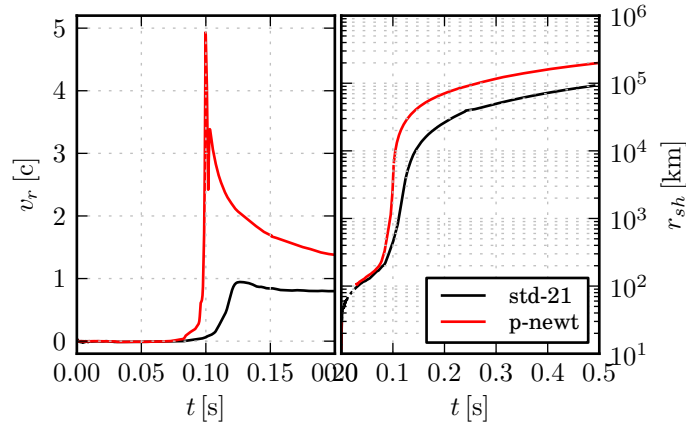


**Figure 3.12:** Comparison of the GR (black line) and post-Newtonian (red line) models. On the left hand side we see the velocity evolution over time. On the right hand side we have the evolution of the shock radius over time.

and contracts faster for the GR model than for the p-newt model, we define the neutron star radius as the density contour of  $\rho = 10^{11} \text{ g/cm}^3$ . The neutron star mass is very similar, as we see in Figure 3.14.

To first order one can assume that the luminosity is proportional to the proto neutron star radius and surface temperature,  $L_\nu \propto T^4 R^2$ , and  $\langle \varepsilon_\nu \rangle \propto k_B T$ . With this we would expect, judging from the difference of the neutron star radius, an even bigger difference between the luminosities of the GR and post-Newtonian models than we see in Figure 3.13. Of course, this is just a crude approximation, which shows that we can not so easily estimate the influence of GR.

### 3.4.2 Nucleon potentials

A further improvement was done for the neutrino nucleon opacities. As already stated in Section 2.5 the simulations before were not taking the nucleon potentials into account for the neutrino nucleon interactions. As this affects  $\nu_e$  and  $\bar{\nu}_e$  differently, we want to discuss in this section what the impact of this improvement is on the neutrino signal. We compare therefore in Figure 3.15 models done with the SHEN EoS which do and do not have the corrected nucleon opacities. We see that both models have similar luminosities for the first 0.15 s. At later times the luminosities of the corrected nucleon opacities model are below the other models luminosities. This is seen more prominent in  $\nu_e$  and  $\nu_x$  than in  $\bar{\nu}_e$ . Martínez-Pinedo et al. (2012) shows the same trend, using the SHEN EoS, in the first 0.5 s of their Fig 2 (upper left panel). We can compare our np-12 model with their RMF “(U<sub>n</sub>, U<sub>p</sub>)” and our std-12 with their “(U<sub>n</sub>, U<sub>p</sub>) = 0” model.

In case of the mean energies, the model with corrected nucleon opacities has lower energies than the model without for the  $\nu_e$  and  $\nu_x$ . For the mean energy of



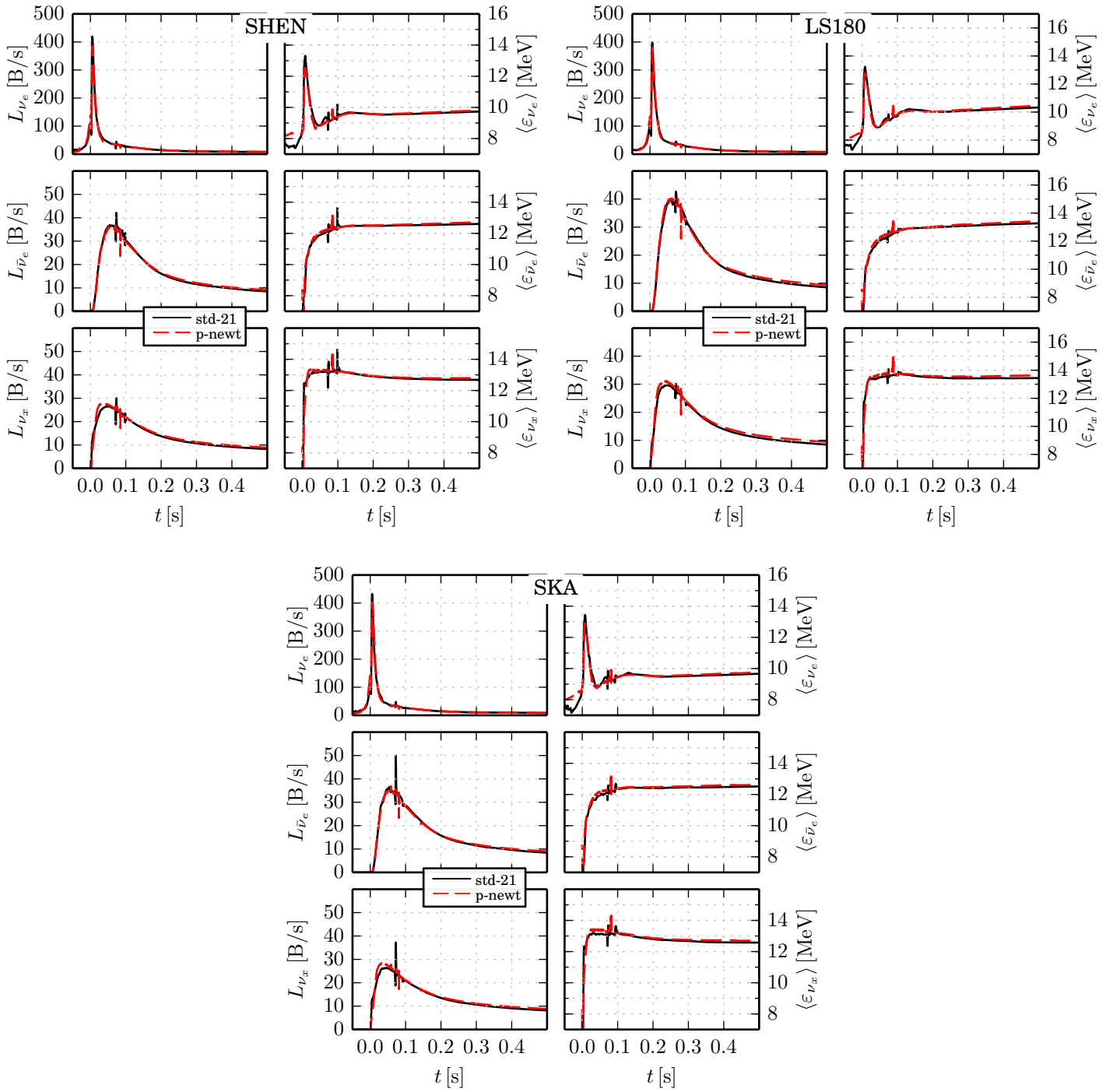


**Figure 3.13:** Comparing the neutrino signal of the GR and post-Newtonian models over the first 500 ms, for the three different EoS.



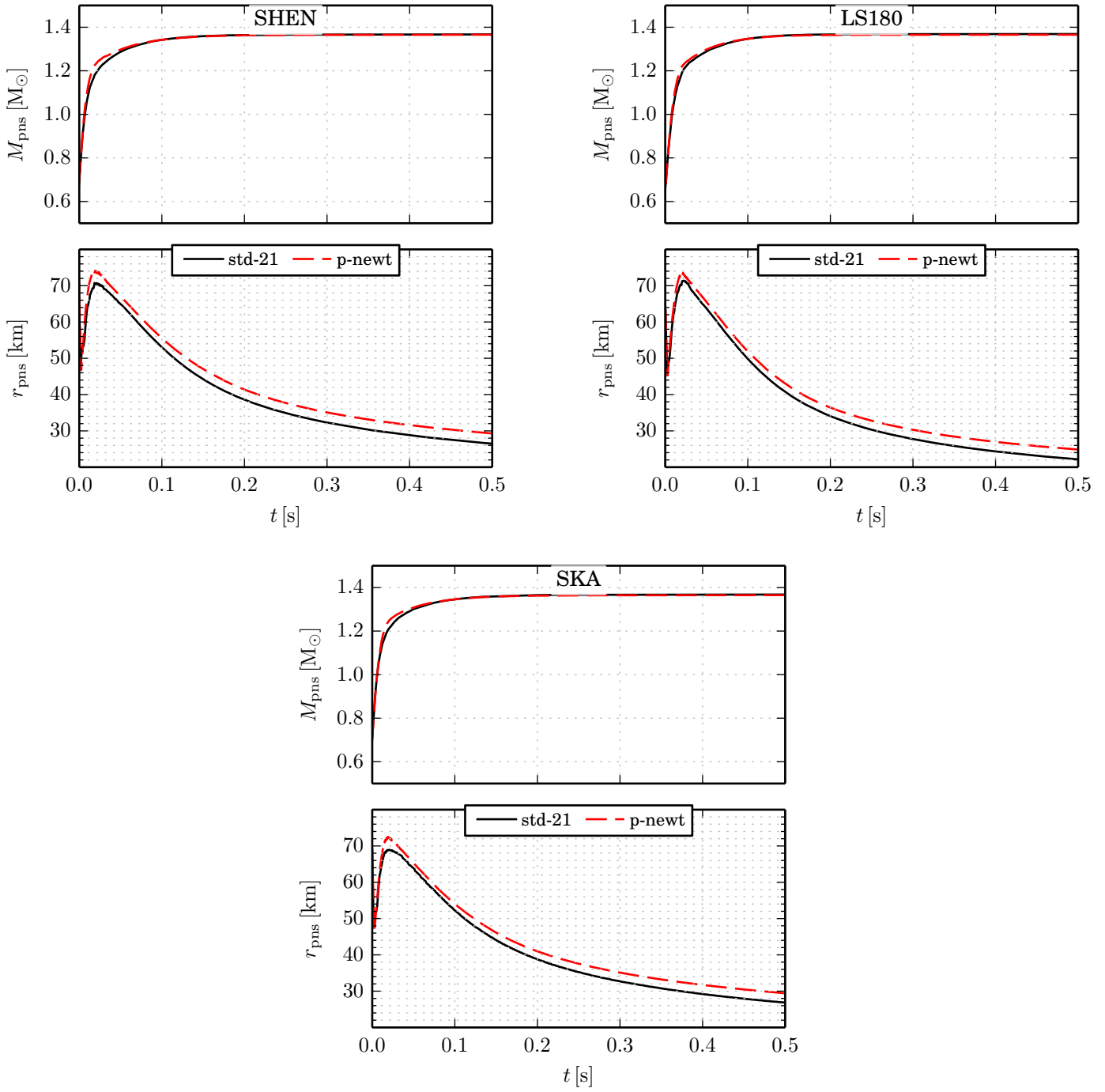


**Figure 3.14:** Comparing the time evolution of the proto neutron star mass  $M_{\text{pns}}$  (upper panel) and proto neutron star radius  $r_{\text{pns}}$  (lower panel) of the GR models with the post-Newtonian models.



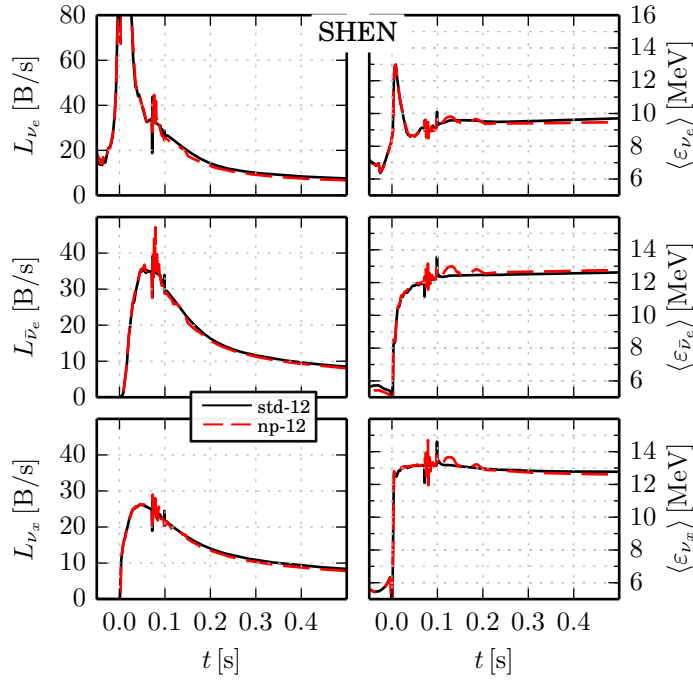


**Figure 3.15:** The neutrino signal of models with the SHEN EoS with and without the corrected neutrino nucleon opacities. Shown are the first 500 ms at a radius of 500 km transformed into a resting lab frame. We see on the left hand side the time evolution of the neutrino luminosities and on the right hand side the time evolution of the neutrino mean energies. As before the top panel shows the electron neutrinos  $\nu_e$ , the middle one the anti-electron neutrinos  $\bar{\nu}_e$ , and the bottom one the heavy-lepton neutrinos  $\nu_x$ .

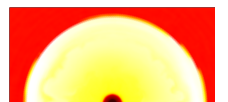
the  $\bar{\nu}_e$ , the corrected model has a slightly higher energy than the std-12 model. This is also in agreement with Martínez-Pinedo et al. (2012) as we see in his Fig. 2, lower left panel.

Comparing those observation with the simulation of the LS180, SKA, and WOLFF EoS, at the end of this Chapter, we can see similar effects, more or less pronounced. The luminosities show more diversity between the different EoS. The WOLFF EoS models, shows the smallest relative influence compared to the other EoS. For the mean energies, we see that the relative influence of the nucleon potentials is very similar for all EoS.

Martínez-Pinedo et al. (2012) and Hüdepohl (2014) show that the main influence of the nucleon potentials occurs during the cooling phase of the proto neutron star. We will also see this in Section 3.5.2.

### 3.4.3 Convection

Hüdepohl (2014) already confirmed that the convection treatment helps to improve 1D simulations and make them more comparable to axially symmetric (2D) simula-



tions. We want to confirm this with our own simulations that now also include GR. We use both convective cases described in Section 2.6. The Newtonian version of Eq. (2.37) was already implemented and well tested with the VERTEX code, see H\"udepohl (2014). Therefore, we adapted his version to the GR module and made a number of test runs with this implementation before conducting simulations with the relativistic criterion of Eq. (2.38).

We actually find that the Newtonian convection criterion agrees better with the 2D simulations than the relativistic convection criterion, see Figure 3.17. The reason for this could be that the larger convectively unstable region in the Newtonian case better models the overshooting in the multidimensional simulation, another reason could be that there are still some unresolved numerical problems for the relativistic criterion. Also, the neutrino pressure and energy density would in principle also need to be included in Eq. (2.37) and (2.38) which should be explored in the future. We kept both cases running with the VERTEX-CoCoNuT code, to compare the effects of both criteria.

To show the differences of those two treatments we made a similar plot as Figures 3.2 and 3.3 from H\"udepohl (2014), to illustrate the convective regions, see Figure 3.16. We see the time evolution of the convective regions of a 2D and a 1D model with the WOLFF EoS. The green region shows the convectively unstable area in the Newtonian case, and the cyan region for the relativistic treatment. To illustrate the convective unstable region of the 2D model we mark the lateral velocities above certain values.

We see two distinct convectively unstable regions. A short lived convection in the core at lower radii and the classical proto neutron star convection, visible for the whole time. We see that the green region is extended over a wider range than the cyan area, especially over the first 0.3 s. Although both treatments lay on top of the convectively unstable area of the 2D model, they do not fully cover the actual area. This might also be due to overshooting, which happens when convective matter is carried into the surrounding convective stable region by its momentum. The 2D model also shows lateral velocities above the PNS radius in the accretion layer, which can not be modelled by a simple mixing-length scheme. We thus allow the mixing length scheme only to work within the proto neutron star.

We want to look at the effect the different convectively unstable areas have in our simulations. Therefore we compare a 2D model of the WOLFF EoS with a non-convective 1D model and two 1D models with convection, one with the relativistic and one with the Newtonian mixing length convection treatment. For this comparison we used models with the same radial and energy resolution, to rule out differences due to that. Also, all models were simulated without the corrected neutrino nucleon opacities as the longest running 2D WOLFF model was set-up without them and to concentrate on the effect of the convection treatment alone. In Figure 3.17 we show in the upper panels a profile of the electron fraction  $Y_e$ , entropy  $s$ , and temperature  $T$  of those models, at a time 125 ms post-bounce. We see that the electron fraction and entropy are the most affected quantities. We also see that the Newtonian convective treatment matches the 2D simulations better



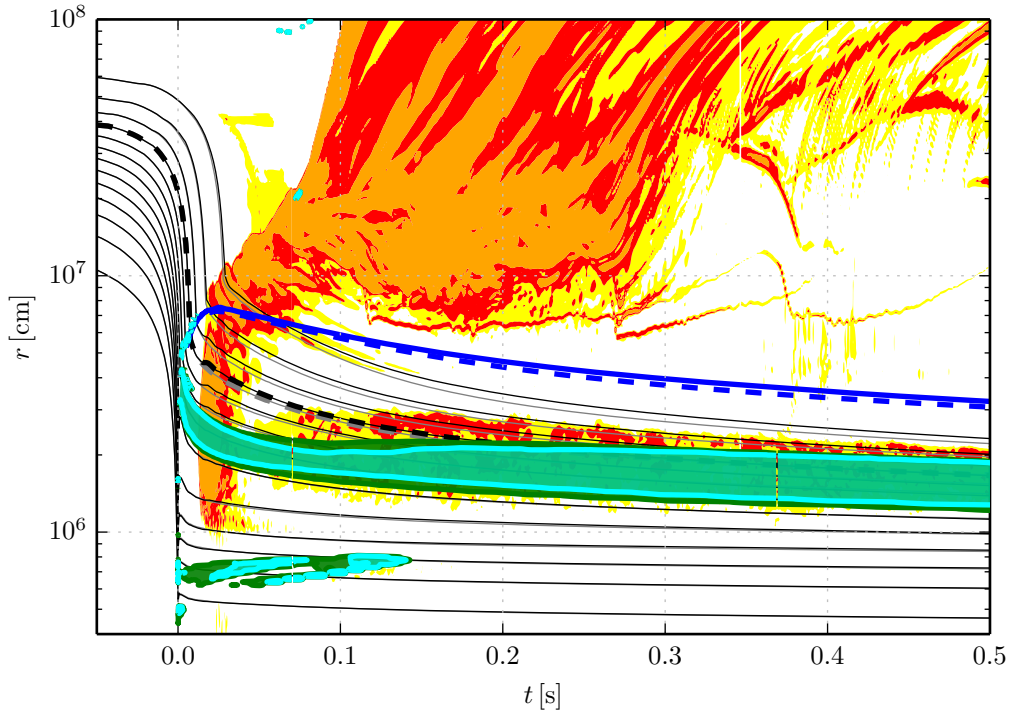
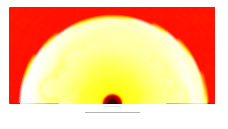


**Figure 3.16:** The lateral velocities higher than 1000, 2000, and 3000 km/s of the 2D model where used to indicate its convection. The green shaded region shows the region where a 1D model would have its convective unstable region if the Newtonian Ledoux criterion was used. The cyan shaded region, is the convective unstable region for the relativistic Ledoux criterion. The blue lines represent the proto neutron star radius, solid for the 2D model, dashed for the non-convective 1D model.

then the relativistic one, which stays closer to the non-convective model.

The lower panels of Figure 3.17 show a direct comparison of the Newtonian convective treatment, left side, and the relativistic convection treatment, right side, with the non-convective model. There, we show the profile, also at 125 ms post-bounce, of the Brunt-Väisälä frequency  $\omega_{BV}$ , a direct measure of the growth rate of a convective instability. We see that in both cases the convective peak around 20 km of the non-convective model is flattened in the case of the models with mixing length convection. Note that the second smaller peak at around 100 km is not flattened by the convective models, as it is outside the PNS.

The different convection treatment also affects the neutrino signal. In Figure 3.18 we show luminosities, left hand side, and the mean energies, right hand side, of the same models as in Figure 3.17. We see again that the convective model with the Newtonian criterion comes closer to the 2D model than the one with the relativistic version. In all flavors is the neutrino luminosity of the 1D non-convective model below the other models. The gap between the 1D non-convective model and the



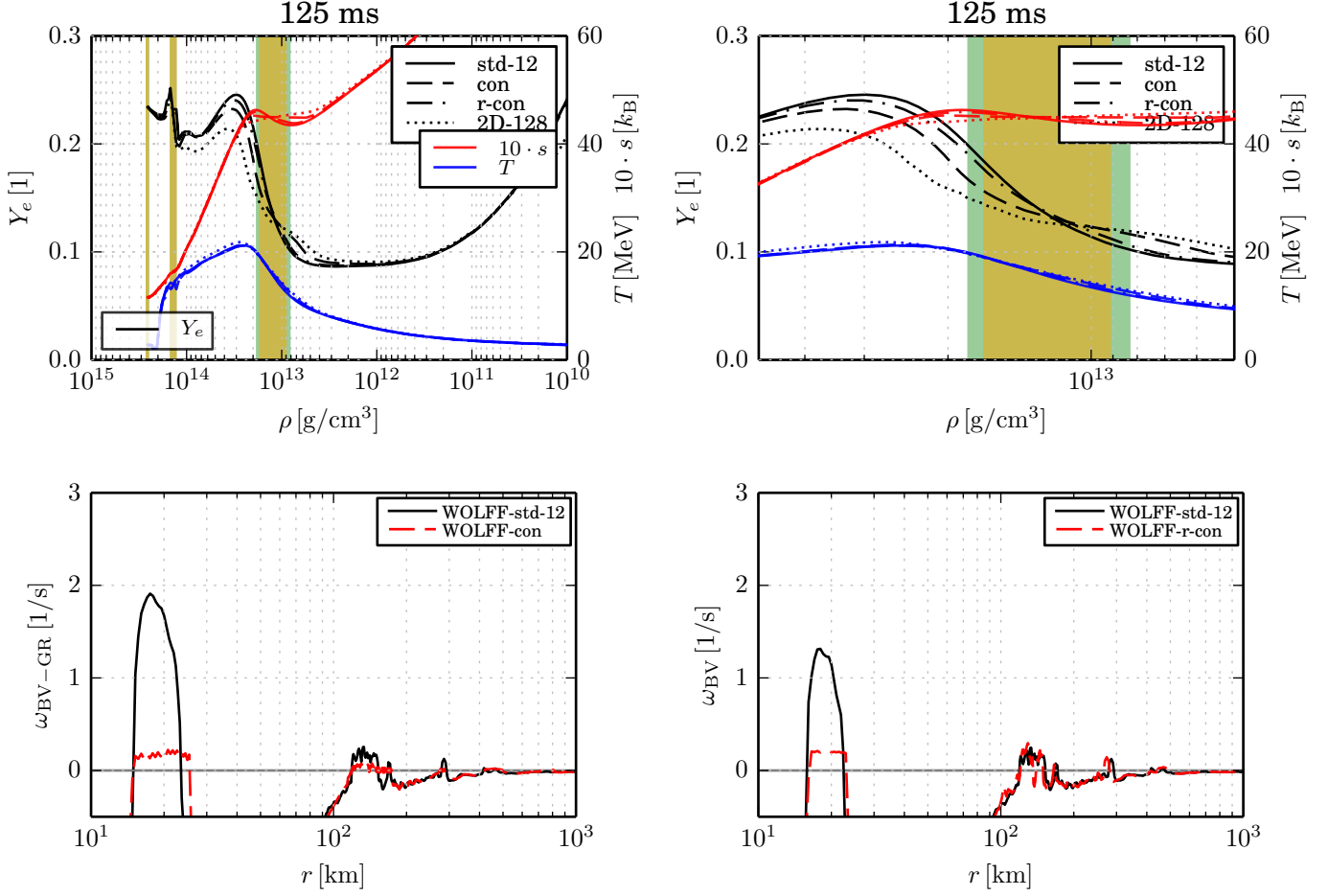


**Figure 3.17:** The upper panel shows profiles of an axially symmetric and two spherically models with the mixing length scheme and one without, 125 ms after core bounce. Marked in green is the region of convective instability according to the Newtonian criterion. The relativistic criterion is represented by the ochre shaded area. We enlarged the convective area of the upper left panel to the upper right hand side, to see the effect better. The lower panel we compare the profile of the Brunt-Väisälä frequency  $\omega_{BV}$  of a non-convective model with a model with the Newtonian criterion (left hand side), and a model with the relativistic criterion (right hand side), also at 125 ms after core bounce.



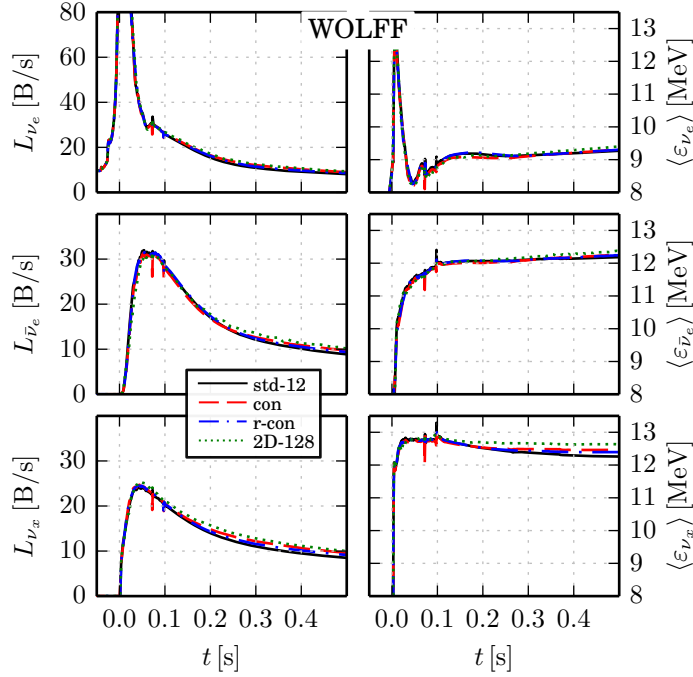


**Figure 3.18:** Comparing the effects of a convective treatment in 1D on the neutrino signal with 2D. Note that the 2D mean energy is averaged over all angles.

2D model increases from the  $L_{\nu_e}$  to  $L_{\bar{\nu}_e}$  to the  $L_{\nu_x}$ . While the 1D Newtonian convective model stays closely below the 2D model, the 1D relativistic convective model is still very similar to the 1D non-convective model. Even though the  $L_{\nu_e}$  are less affected, the 1D model with Newtonian convection agrees better with 2D model than the other two.

For the mean energies of the 2D model we used an angular averaged mean energy, for a better comparison, similar to Eq.(3.5) defined as the angle-integrated neutrino energy density over the angle-integrated number density,

$$\langle \epsilon \rangle_{\Omega} = \frac{\int_{\Omega} \int_0^{\infty} d\epsilon \int_{-1}^1 d\mu \mathcal{I}(\epsilon, \mu, \theta, \phi)}{\int_{\Omega} \int_0^{\infty} d\epsilon \int_{-1}^1 d\mu \epsilon^{-1} \mathcal{I}(\epsilon, \mu, \theta, \phi)}. \quad (3.7)$$

We see that the mean energies of the 2D model are a bit higher than the 1D models, especially in the  $\langle \epsilon_{\nu_x} \rangle$  case. Although the differences are minimal, we can, at least for the  $\nu_x$  mean energies, see that again the model with the Newtonian convection criterion agrees better with the 2D case than the model with the relativistic convection criterion.

In Figure 3.19 we see that the proto neutron star radius for the 2D and convection models is higher than the for the non-convective model. This explains the shallower luminosity of these models. The luminosity can be estimated on the basis of the proto neutron star (PNS) radius with  $L_{\nu} \propto R^2 T^4$ . As the mean energies of the



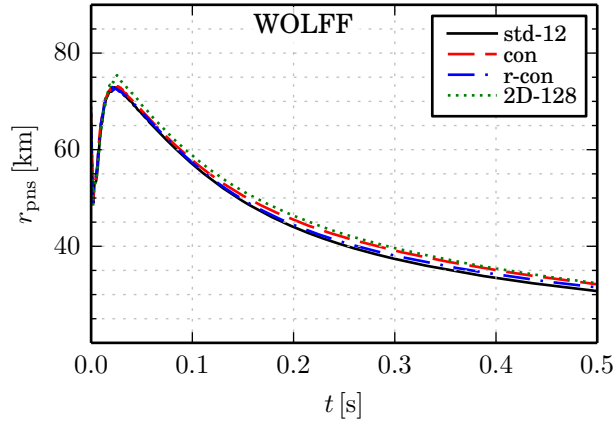


**Figure 3.19:** Comparison of the proto neutron star between the non-convective 1D model, the two convective 1D models and a 2D model.

models are quite similar to each other, we can ignore the temperature component as  $\langle \varepsilon_\nu \rangle \propto k_B T$ . And we find that the relative difference of  $R_{PNS}^2$  matches the relative differences of the luminosities of the different models, the different PNS radius thus seems to be the dominant source for the different luminosities.

(We chose the WOLFF EoS for this comparison as it is the 2D model which has been simulated longest.)

We also want to investigate the relative effects of a convective model compared to a non-convective model in 1D and with different EoS. Note that from here on the convective models with both types of convection are also simulated with the corrected neutrino nucleon opacities.

In Figure 3.20 and 3.21 we show the neutrino signal of all our models with the five different EoS. To look only at the effect of the convection on has to compare the convection models (con-np, r-con-np) with the non-convective models with corrected neutrino nucleon opacities (np-12). In our simulations all the luminosities of the convective models are higher than those of the non-convective models, for all EoS. But the luminosity of the different EoS models vary in the relative influence of the convection. The LS180 (the softest EoS) model shows the biggest differences, the WOLFF (the stiffest EoS) model the lowest. Also we see, as mentioned above, that the Newtonian convective models have higher luminosities than the relativistic convection models. For the relativistic criterion the highest difference to the non-convective model are also found for the LS180 and the lowest for the WOLFF EoS.

The effect of the Newtonian convection models are comparable to H\"udepohl (2014). But one should consider that in these models the accretion phase is much longer and the explosion has not occurred in the first 0.5 s. A better comparison can be done in the later cooling phase.

The relative influence of the convection on the mean energies is very similar



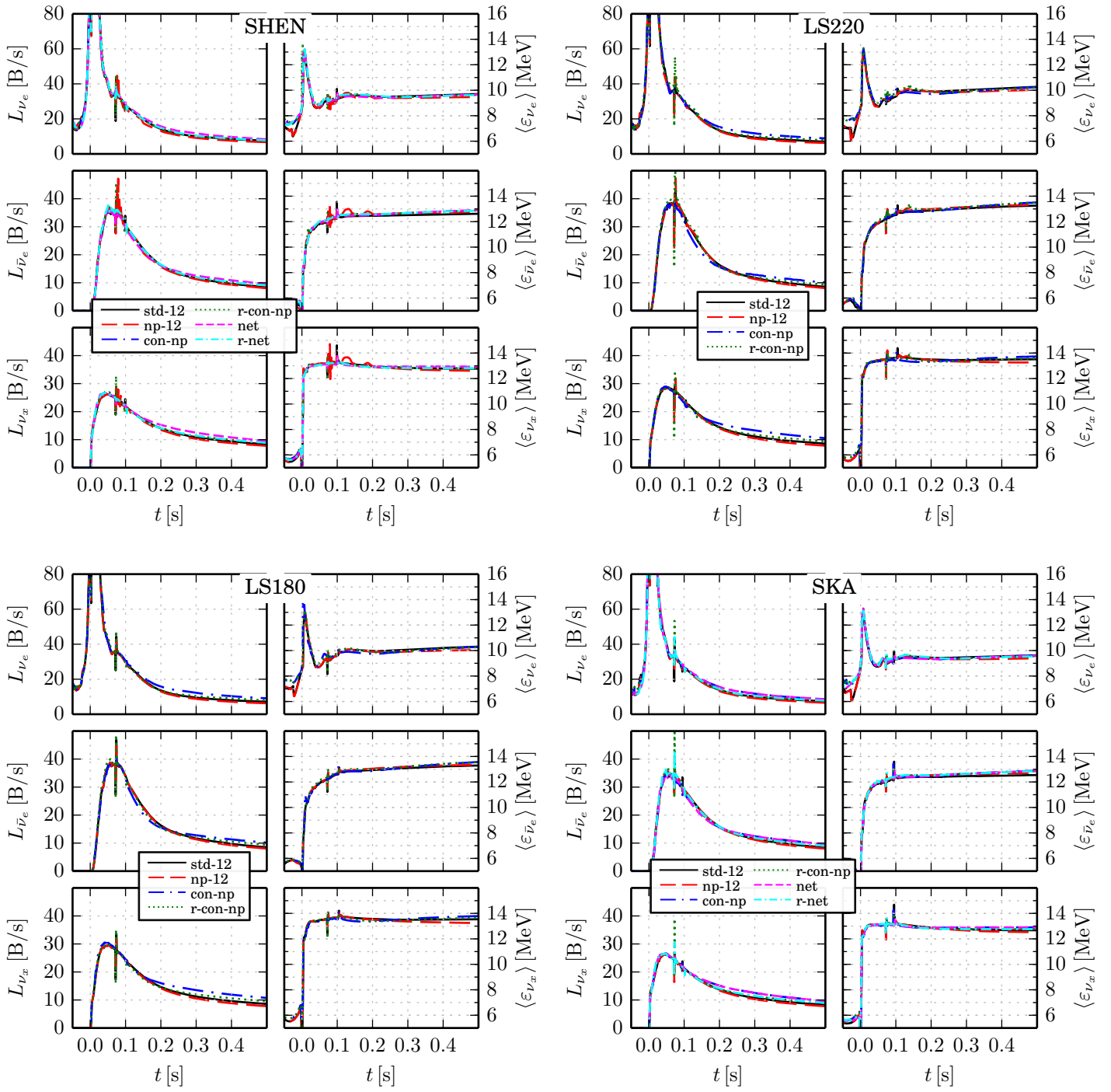
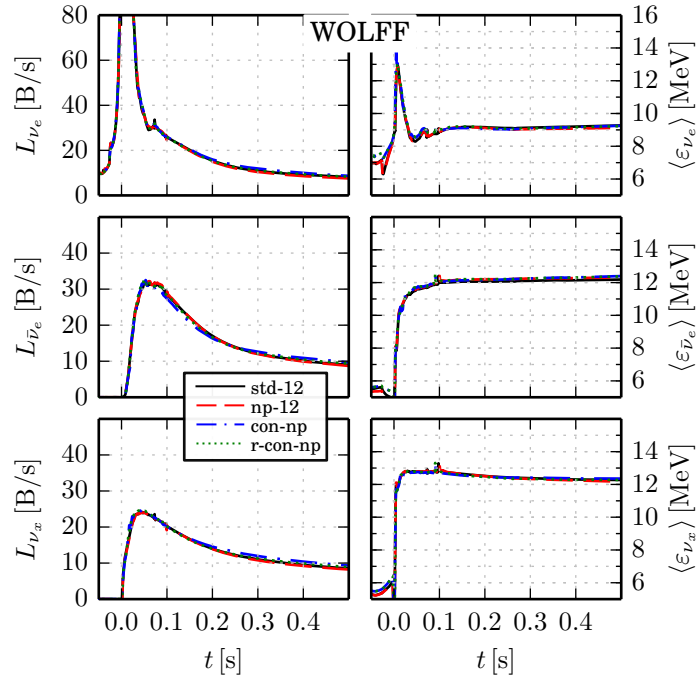


Figure 3.20: Neutrino signal for all models for four different EoSs.





**Figure 3.21:** Neutrino signal for all models with the WOLFF EoS.

for all EoS and also for the Newtonian and relativistic convection. After 0.3 s the  $\nu_e$  mean energies are always higher for the convection models than for the non-convective models, as are the  $\bar{\nu}_e$  energies, for all EoS. The same effect is seen for the  $\nu_x$  mean energies, but more pronounced. This is in contrast to Hüdepohl (2014) where his Table 3.4 shows that the mean energies are lower for the first 0.5 s. The reason is that in his models the accretion is still ongoing during the first 0.5 s. If we compare our models with the later cooling phase of the models in Hüdepohl (2014), e.g. his Figure 5.3, we see that the mean energies for the first few seconds are also higher there for the convection models than for non-convective ones.

In our simulations the higher luminosities for the convective models goes hand in hand with the increased proto neutron star radius, which we show in Figures 3.22 for each EoS. We see that the proto neutron star radius for the convection models follows the non-convective models for the first  $\sim 0.15$  s, in the Newtonian cases, and  $\sim 0.25$  s for the relativistic cases. After that the radius gets larger for the convection models than the non-convective models, just like the luminosities, which also get higher after  $\sim 0.15$  s,  $\sim 0.25$  s, respectively.

All five EoS show similar behaviour in the relative differences of the models. Only the LS180 EoS shows some peculiarity around the formation of the proto neutron star, where the Newtonian convective model is higher than all other models. This might be due to an extended “prompt” convection region.



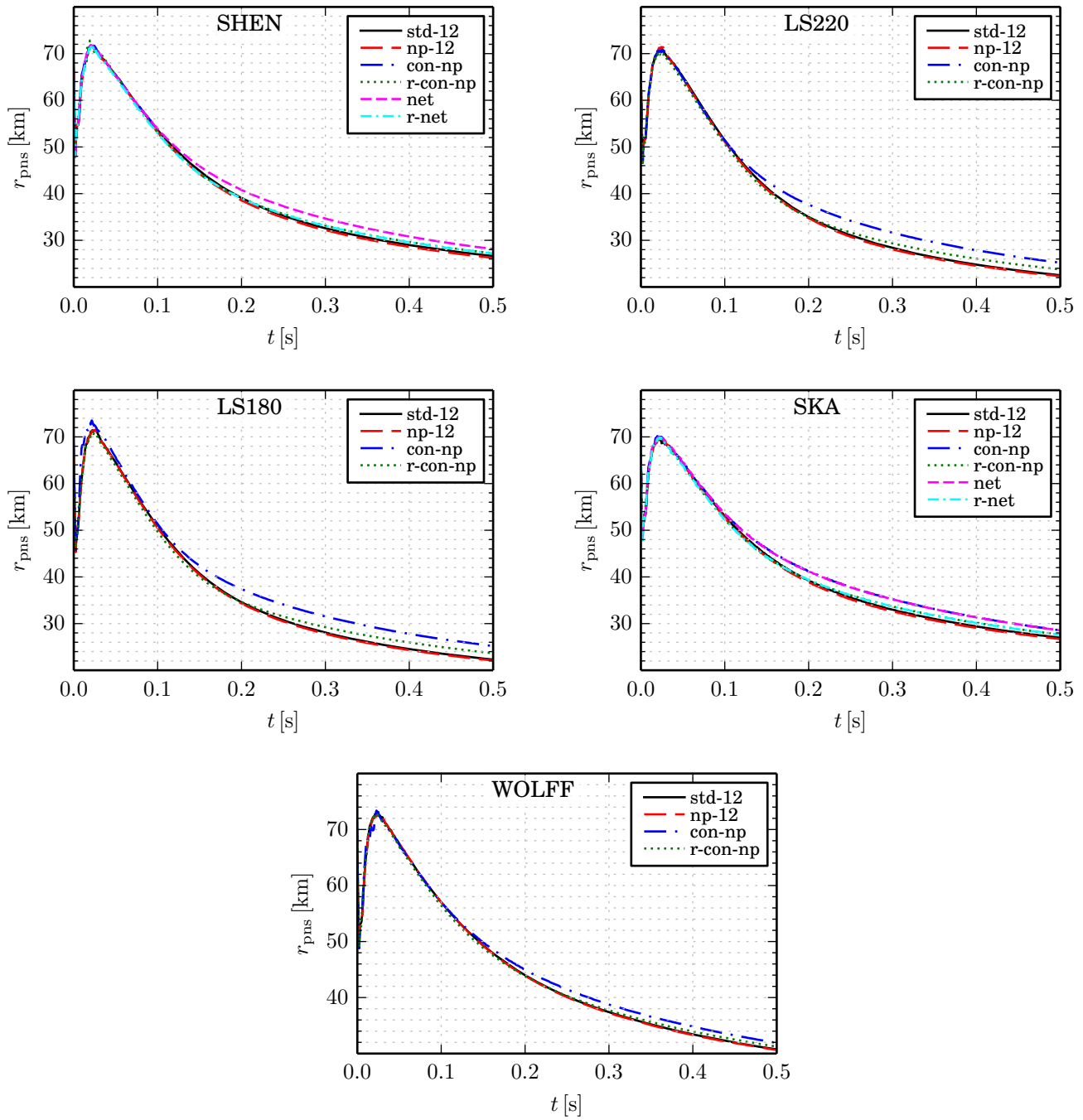


**Figure 3.22:** The proto neutron star radius for all models with the five different EoS in the first 500 ms.



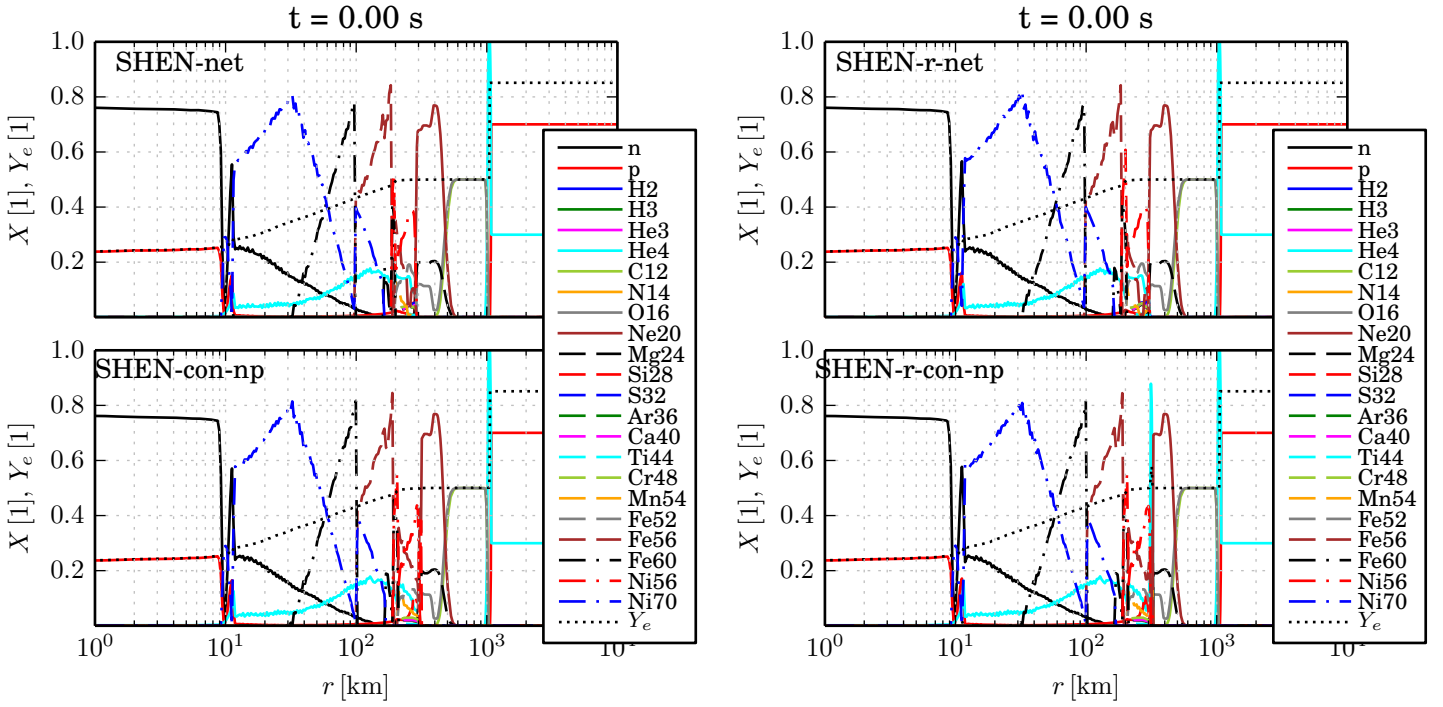


**Figure 3.23:** Comparing the mass fraction and  $Y_e$  of the models with and without network burning treatment at the time of bounce. Exemplary for the models with the SHEN EoS, at the moment of core bounce.

### 3.4.4 Network

The next step of improvement are simulations done with the full nuclear burning network instead of an approximative burning treatment, see Section 2.3. The neutrino signal of the simulations with the network shows almost no difference to the one with the approximative burning treatment, see Figure 3.20. Also the time averaged neutrino parameters over the first 0.5 s are nearly the same for the models with and without network, see Table 3.5.

During the collapse the initial elements of the progenitor get burned to heavier elements. In Figure 3.23 we show the mass fraction at the time of core bounce to see the difference between both burning models. In the upper panels we show the mass fraction of a model where we used the full nuclear burning network and the lower panels show simulations with the approximative burning treatment. We see that the approximative burning is quite good to reproduce the same abundances as the models with the full network. We get the same result for the models with the SKA EoS. In Table 3.4 we compare quantities at the moment of collapse of the model with and without network. We see that also the collapse quantities are in a good agreement with each other. The difference is within a 1% range. Differences appear however later, during the explosion. If we define the time of explosion to be



**Table 3.4:** Comparison of quantities at the moment of bounce for the models with the approximative burning treatment and the models with the full network, the shock radius ( $r_{\text{sh}}$ ), the enclosed mass ( $M_{\text{sh}}$ ) and the collapse duration  $t_{\text{col}}$ .

Model	SHEN		
	$r_{\text{sh}}$ [km]	$M_{\text{sh}}$ [ $M_{\odot}$ ]	$t_{\text{col}}$ [s]
con-np-1D	11.06	0.485	0.060
net-1D	11.10	0.486	0.061
r-con-np-1D	11.06	0.485	0.060
r-net-1D	11.06	0.485	0.061

Model	SKA		
	$r_{\text{sh}}$ [km]	$M_{\text{sh}}$ [ $M_{\odot}$ ]	$t_{\text{col}}$ [s]
con-np-1D	10.62	0.494	0.062
net-1D	10.59	0.492	0.063
r-con-np-1D	10.58	0.493	0.062
r-net-1D	10.58	0.493	0.063

when the shock radius reaches 500 km, we see that models with network explode a bit later than models with the approximative burning treatment. The highest difference, with 9 ms delay, is found for the models with the SKA EoS and the Newtonian convection criterion, see Table 3.11 and 3.12.

Fischer et al. (2010) use for their simulation of the ONeMg core also a nuclear reaction network. Comparing their mass fraction and  $Y_e$  at bounce with ours we actually find that our simulation with the approximate burning treatment agrees better with their result than our network simulation.

### 3.4.5 EoS

The neutron star Equation of State is one of the biggest uncertainties for supernova simulations. We saw in the sections above that we get quite different results for different EoS. By comparing the neutrino signal for the different EoS one might hope to find differences which could be detectable by neutrino detectors. Figure 3.24 shows the neutrino signal for the first 500 ms of five different EoS models with the relativistic convection. We see that for the luminosity the five EoS models have different  $\bar{\nu}_e$  and  $\nu_x$  maxima. This is also the case for the  $\nu_e$  burst, although it is difficult to see. The difference gets smaller at later times. The highest luminosities for the  $\nu_e$  burst is obtained by the model with the SKA EoS, followed by the models with the WOLFF and SHEN EoS. The models with the LS180 and LS220 EoS have the lowest luminosities for the  $\nu_e$  burst. For the maxima of the  $\bar{\nu}_e$  and  $\nu_x$ , the



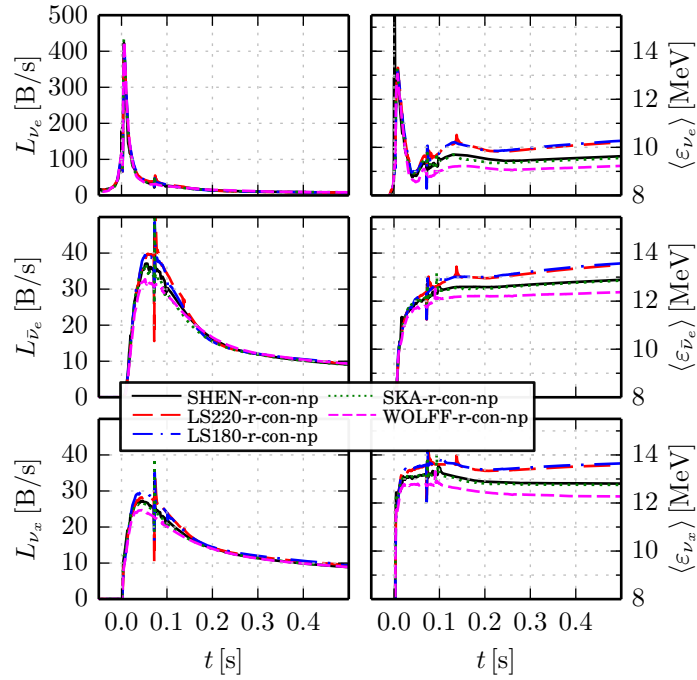


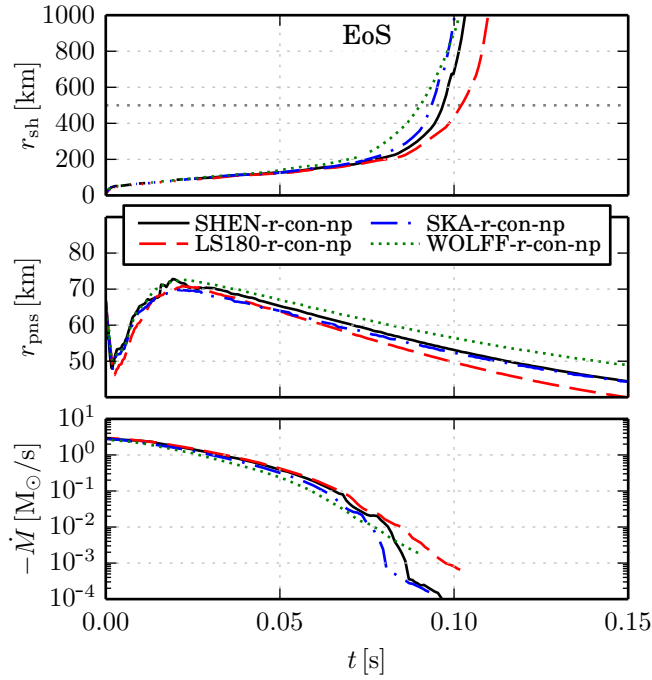
**Figure 3.24:** Neutrino signal for the relativistic convection models with five different EoS. Note the small irregularity at around 0.07s is due to a numerical artefact when we transform the co-moving neutrino signal into the observer frame.

models with the LS180 and LS220 show the highest luminosities followed by the models with the SKA and SHEN EoS. The model with the WOLFF EoS shows the lowest maxima for the  $\bar{\nu}_e$  and  $\nu_x$  luminosities.

Models of the ONeMg progenitor with the LS180 and the WOLFF EoS were also simulated by Kitaura (2007, Appendix II). He used the VERTEX code with a post-Newtonian effective gravitational potential and found that also for his models with the WOLFF EoS the  $\nu_e$  is higher than for his models with LS180. Also we find the maxima of the  $\bar{\nu}_e$  and  $\nu_x$  luminosities higher for the models with the LS180 than for the models with the WOLFF EoS. A similar behaviour as we found was seen by H udepohl (2009) who used models with the SHEN, LS180 and SKA EoS. (H udepohl (2009) also did simulations with the ONeMg progenitor and the VERTEX code with an effective gravitational potential.)

The mean energies on the right side of Figure 3.24 show a similar behaviour within all neutrino flavors. Over the whole first 0.5s the models with the LS180 and LS220 EoS show the highest energies closely followed by the SHEN and SKA EoS models. The WOLFF EoS model has always the lowest energies for all flavors. To set that into a relation, the relative difference between the LS180 model with the highest and WOLFF EoS model with the lowest mean energies is at 0.4s, 9%, 8%, and 10% for the  $\nu_e$ ,  $\bar{\nu}_e$ , and  $\nu_x$  mean energies. In the case that neutrinos

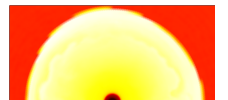




**Figure 3.25:** The upper panel shows the shock radius of the models with relativistic convection treatment and all five EoS. We define the point when the shock radius passes 500 km, gray dotted line, as the explosion time. The middle panel shows the proto neutron star radius and the lower panel the mass accretion, evaluated at 500 km, which ceases as soon as the explosion sets in.

would be observed at one could potentially infer something about the EoS. The behaviour of the different EoS models for the mean energies is also in agreement with the literature mentioned above.

Thompson et al. (2003) give a comparison of the neutrino signal for simulations done with the LS180 and LS220 EoS. They use a 1D Boltzmann neutrino radiation transport with Newtonian hydrodynamics and an  $11 M_{\odot}$  progenitor and find, as we do, that the neutrino signal is quite similar. Sumiyoshi et al. (2005) use a 1D general relativistic hydrodynamics code with a Boltzmann neutrino transport. They compare models with the LS180 and SHEN EoS with a  $15 M_{\odot}$  progenitor. Similar to us they find higher neutrino luminosities and mean energies for the model with the LS180 EoS than for the model with the SHEN EoS, although their luminosities show a higher difference between the two. This is probably due to the larger progenitor which has a longer accretion phase. Sumiyoshi et al. (2005) also claims that they find a significant difference in the proto neutron star radius and the shock radius. In Figure 3.25 we see in the upper panel the shock radius and in the middle panel the proto neutron star radius of our models with five different EoS. Comparing the shock radius to models done in 1D with other progenitor is



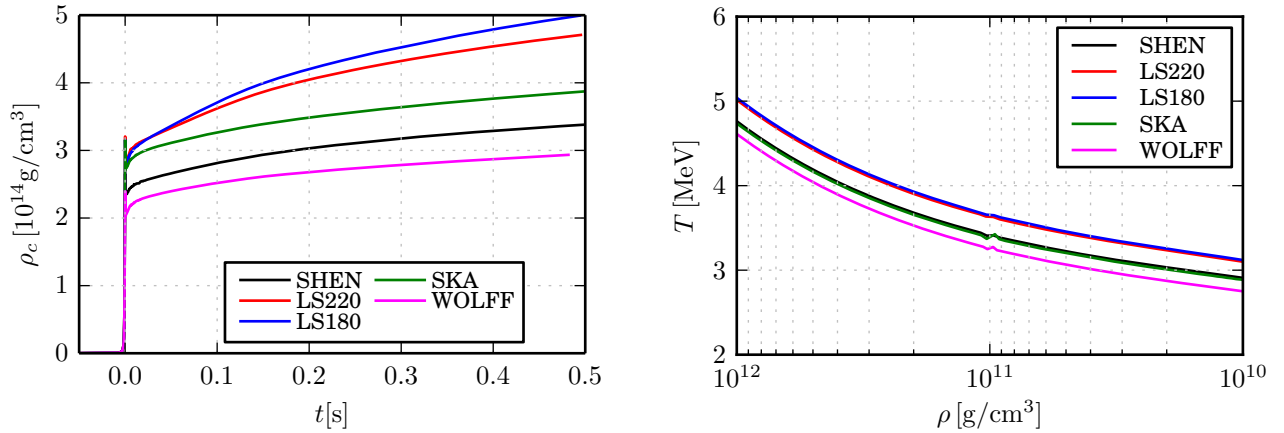


**Figure 3.26:** The left panel shows the central density of the models with the relativistic convection criterion. On the right panel we show the temperature, of the relativistic convection models, as a function of density, at 0.4 s post-bounce. Note that we define the proto neutron star radius to be at a density of  $10^{11} \text{ g/cm}^3$ , where we also switch from the high-density EoS to the low density prescription. This is the cause of the small defects visible around that density.

difficult, as they tend not to explode. Anyhow we see that the model with the WOLFF EoS explodes first followed by the models with the SKA, SHEN EoS. The model with the LS180 EoS explodes  $\sim 12$  ms after the model with the WOLFF EoS, see also Tables 3.9 and 3.8. We do not show the relativistic convection model with the LS220 EoS, as this is one of the models which showed an early explosion of the outer hull, see Figure 3.6.

The WOLFF EoS model has the highest proto neutron star radius, followed by the SHEN and LS180 EoS models with very similar radius and the SKA EoS model with lowest radius. After 0.2 s, the WOLFF EoS model has still the highest proto neutron star radius but the other models have changed places. The SKA EoS model has now a higher PNS radius than the SHEN and LS180 models, and the LS180 EoS model has now the lowest. As the WOLFF EoS model did not contract as fast as the other models, we can expect that we also have a colder proto neutron star with the WOLFF EoS. Having lower temperatures, less energetic neutrinos get emitted, hence the lower energies. Similarly, the proto neutron star of the LS180 EoS model is the hottest of all five EoS models as it contracted fastest. Here we find higher temperatures and thus more energetic neutrinos. This can be seen in Figure 3.26, where the time evolution of the central densities are shown. The temperature profile can be seen on the right hand side of Figure 3.26. We see that the WOLFF EoS has the lowest temperature around the proto neutron star radius. This is followed by the SKA and SHEN EoS models, as well as the LS220 and LS180 EoS models, which are almost on top of each other. At  $10^{11} \text{ g/cm}^3$  we see a small dip, more or less pronounced, for all models. This comes from the fact that



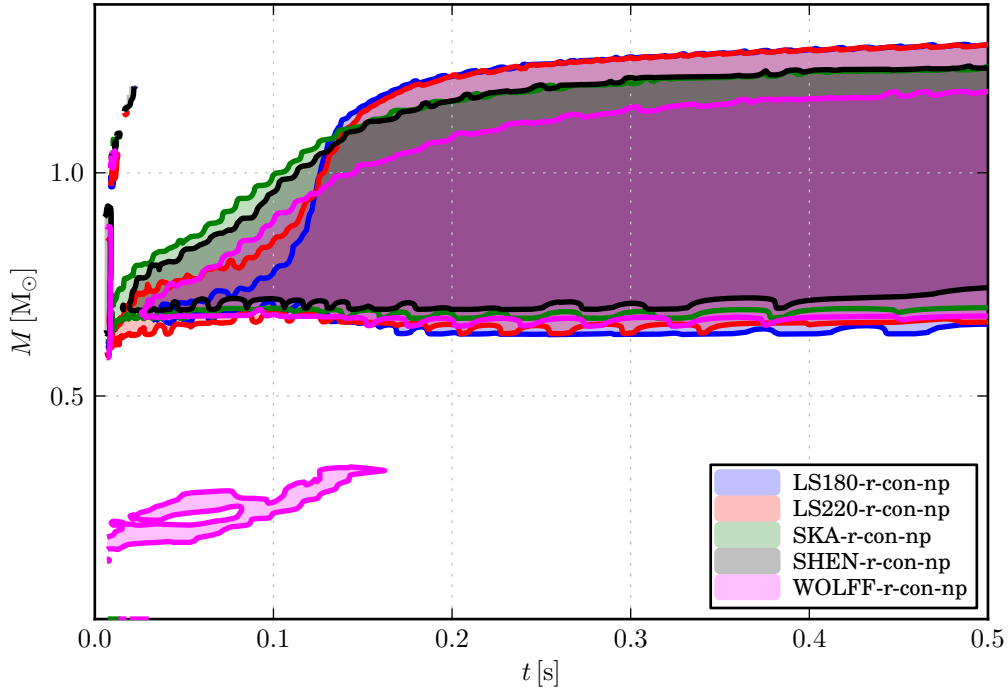


**Figure 3.27:** Regions of convective instability ( $\omega_{BV-GR} > 0$ ) for the various EoSs.

we change from high density EoS to low density EoS at this threshold.

Marek et al. (2009) compare in their 1D and 2D simulations, with the VERTEX code with an effective relativistic gravitational potential, models with the LS180 and WOLFF EoS of a  $15 M_{\odot}$  progenitor. They find similar behaviour between the models with those two EoS as we do for the proto neutron star radius and neutrino signal. Additionally they also compared the convectively unstable region of their 2D models. They see that the prompt convection for the WOLFF EoS model is larger than for the LS180 EoS model. They also say that the convective unstable region of the WOLFF EoS involves more mass and extends over larger radii. We saw in Section 3.4.3 that our mixing length approach does not cover the full extent of the convectively unstable region of a 2D model. But we still can make some approximate remarks about the extent of the convectively unstable region for the different EoS. In Figure 3.27 those areas shaded for each EoS. We see that in the first 0.1 s the SHEN and SKA EoS models cover a larger convectively unstable region than the other EoS models. After that, the unstable region of the two models lies between the one of the WOLFF EoS model and the LS180, LS220 models. Interesting is that the LS180 EoS model has the smallest unstable area at the beginning up to around 0.12 s after which it has the largest. This is also reflected in the neutrino signal, where we see the main effect of the convection



after 0.12 s. The convectively unstable region for the LS220 model is around the same as the one for the LS180 model. The WOLFF EoS model has the smallest unstable area during the first 0.5 s. Marek et al. (2009) show the first 700 ms of their simulations and we agree with them that for this timespan the convectively unstable region involves more mass for the model done with the WOLFF EoS than with the LS180 EoS.

Summarising for the early phase we show time averaged neutrino parameters of all our model and all five EoS for the first 0.5 s in in Tables 3.5 and 3.6. If we compare our values to the s11.2 models of H udepohl (2014), which have similar proto neutron star masses, we see very similar values. The neutrino mean energies of H udepohl (2014) are higher than in our models, due to the ongoing accretion of those models. The cumulatively emitted neutrino energies are also quite similar. On average, we see that the models with the LS180 and LS220 EoS have the highest mean energies and total emitted energies, whereas the models with the WOLFF EoS have the highest total emitted neutrino number. Other than that the models with the WOLFF EoS have the lowest mean energies, and the SKA EoS models have the lowest total emitted neutrino number and energies.



**Table 3.5:** Time averaged neutrino parameters of all models up to 0.5 s post-bounce. To get the total emitted energy we have to sum the energies of the  $\nu_e$ ,  $\bar{\nu}_e$  and four time the  $\nu_x$  as they only represent one of four heavy lepton neutrino kinds.

Model	LS180								
	$\langle \varepsilon \rangle_{\nu_e}$	$\langle \varepsilon \rangle_{\bar{\nu}_e}$	$\langle \varepsilon \rangle_{\nu_x}$	$N_{\nu_e}$	$N_{\bar{\nu}_e}$	$N_{\nu_x}$	$E_{\nu_e}$	$E_{\bar{\nu}_e}$	$E_{\nu_x}$
	[MeV]			$[10^{57}]$			[B]		
con-np-1D	10.5	12.7	13.5	0.98	0.42	0.38	16.4	8.6	8.2
np-12-1D	9.9	12.7	13.4	0.90	0.41	0.34	14.2	8.3	7.3
r-con-np-1D	10.1	12.8	13.5	0.92	0.42	0.36	15.0	8.6	7.7
std-12-1D	9.9	12.6	13.5	0.91	0.42	0.35	14.5	8.5	7.5
std-21-1D	10.1	12.7	13.5	0.91	0.42	0.35	14.8	8.5	7.5

Model	LS220								
	$\langle \varepsilon \rangle_{\nu_e}$	$\langle \varepsilon \rangle_{\bar{\nu}_e}$	$\langle \varepsilon \rangle_{\nu_x}$	$N_{\nu_e}$	$N_{\bar{\nu}_e}$	$N_{\nu_x}$	$E_{\nu_e}$	$E_{\bar{\nu}_e}$	$E_{\nu_x}$
	[MeV]			$[10^{57}]$			[B]		
con-np-1D	10.0	12.7	13.4	0.96	0.42	0.37	15.5	8.6	8.0
np-12-1D	9.8	12.7	13.4	0.90	0.41	0.33	14.2	8.4	7.2
r-con-np-1D	10.1	12.8	13.4	0.93	0.42	0.35	15.0	8.7	7.6
std-12-1D	9.9	12.6	13.5	0.91	0.42	0.34	14.4	8.5	7.4
std-21-1D	10.1	12.6	13.4	0.91	0.42	0.34	14.8	8.4	7.3

Model	SKA								
	$\langle \varepsilon \rangle_{\nu_e}$	$\langle \varepsilon \rangle_{\bar{\nu}_e}$	$\langle \varepsilon \rangle_{\nu_x}$	$N_{\nu_e}$	$N_{\bar{\nu}_e}$	$N_{\nu_x}$	$E_{\nu_e}$	$E_{\bar{\nu}_e}$	$E_{\nu_x}$
	[MeV]			$[10^{57}]$			[B]		
con-np-1D	9.8	12.4	12.9	0.94	0.41	0.36	14.9	8.1	7.6
net-1D	9.8	12.4	12.9	0.95	0.41	0.36	14.9	8.1	7.6
np-12-1D	9.6	12.4	12.9	0.88	0.40	0.33	13.6	7.9	6.8
r-con-np-1D	9.9	12.4	12.9	0.91	0.41	0.35	14.4	8.1	7.2
r-net-1D	9.9	12.4	12.9	0.91	0.41	0.35	14.5	8.2	7.2
std-12-1D	9.7	12.2	12.9	0.90	0.41	0.34	14.0	8.0	7.0
std-21-1D	9.9	12.3	12.9	0.90	0.41	0.34	14.4	8.0	6.9



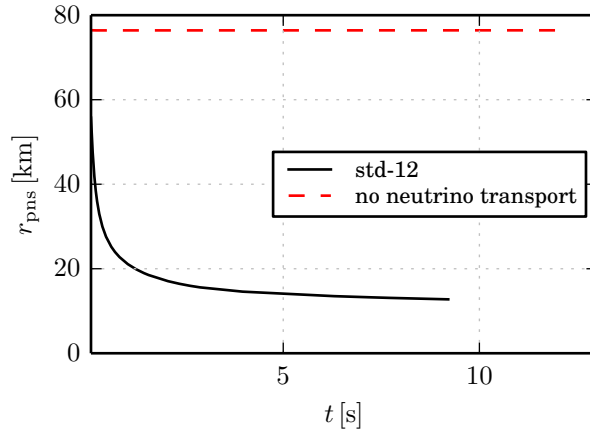
**Table 3.6:** Continuation of Table 3.5 but for the models with the SHEN and WOLFF EoS.

Model	SHEN								
	$\langle \varepsilon \rangle_{\nu_e}$	$\langle \varepsilon \rangle_{\bar{\nu}_e}$	$\langle \varepsilon \rangle_{\nu_x}$	$N_{\nu_e}$	$N_{\bar{\nu}_e}$	$N_{\nu_x}$	$E_{\nu_e}$	$E_{\bar{\nu}_e}$	$E_{\nu_x}$
	[MeV]			$[10^{57}]$			[B]		
net-1D	9.8	12.4	13.0	0.96	0.42	0.37	15.1	8.4	7.6
np-12-1D	9.6	12.4	13.0	0.90	0.41	0.33	13.8	8.1	6.9
r-con-np-1D	9.9	12.4	13.0	0.93	0.42	0.35	14.7	8.3	7.3
r-net-1D	9.9	12.4	12.9	0.93	0.42	0.35	14.7	8.4	7.3
std-12-1D	9.7	12.3	13.0	0.92	0.42	0.34	14.2	8.2	7.1
std-21-1D	9.9	12.3	12.9	0.92	0.42	0.34	14.6	8.2	7.0

Model	WOLFF								
	$\langle \varepsilon \rangle_{\nu_e}$	$\langle \varepsilon \rangle_{\bar{\nu}_e}$	$\langle \varepsilon \rangle_{\nu_x}$	$N_{\nu_e}$	$N_{\bar{\nu}_e}$	$N_{\nu_x}$	$E_{\nu_e}$	$E_{\bar{\nu}_e}$	$E_{\nu_x}$
	[MeV]			$[10^{57}]$			[B]		
con-np-1D	9.7	12.1	12.5	0.98	0.42	0.36	15.3	8.0	7.2
np-12-1D	9.5	12.0	12.5	0.95	0.42	0.34	14.4	8.0	6.8
r-con-np-1D	9.7	12.1	12.5	0.96	0.42	0.35	14.9	8.1	7.0
std-12-1D	9.5	11.9	12.5	0.96	0.42	0.34	14.6	8.0	6.9
std-21-1D	9.7	12.0	12.5	0.96	0.42	0.34	14.9	8.0	6.8





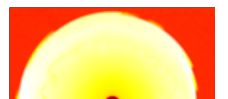
**Figure 3.28:** The proto neutron radius of models with and without neutrino interactions done with the SHEN EoS.

### 3.5 Cooling

After the explosion, the proto neutron star becomes exposed. Comparing Figure 3.4 and 3.5 we saw the huge difference of a simulation done with and without neutrino transport. We illustrate especially the effect the lack of neutrinos have on the proto neutron star in Figure 3.28, where we show the proto neutron star radius of a model with and without neutrino interactions. We see that the proto neutron star radius of the model without neutrino interactions stays constant, while it can cool and shrinks drastically for the other model. As the proto neutron star cools further, more and more trapped neutrinos can escape. The neutrinos still deposit some energy in the matter at the surface of the proto neutron star. This leads to a thermally driven mass outflow, called the neutrino driven wind (Duncan et al., 1986).

The cooling of the proto neutron star can also be treated with a steady state approach, as was done by e.g. Pons et al. (1999); Thompson et al. (2001); Roberts (2012). They treat the cooling as a diffusion process. This is reasonable in the proto neutron star itself as the density and optical depth are very high there and neutrinos are still trapped. But these simulations can not accurately simulate the region of decoupling near the proto neutron star surface and the outflow, where these conditions are not given anymore. They can therefore also not accurately predict the correct neutrino mean energies.

Simulations with a more accurate neutrino transport have been done by Fischer et al. (2010); Hüdepohl et al. (2010); Hüdepohl (2014). In this Section we will compare our results with Hüdepohl (2009) and look at the influence of the corrected neutrino nucleon opacities and convection for the cooling phase.



### 3.5.1 GR vs. Post-Newton

As our models with the higher energy resolution have not progressed far enough so far, we therefore have to compare the long time simulations from H udepohl (2009) with our standard models which have, with 12 energy bins, a lower energy resolution. As the relative effects of the difference between GR and non-GR is greater than that of the energy resolution, see Section 3.3, it is probably justified to use the 12 energy bin models.

In Figure 3.29 we compare the neutrino signal over several seconds for the models with and without GR for the available three EoS. We see that the luminosities for the GR models are lower than for the post-Newtonian models for the first few seconds. In case of the models done with the LS180 EoS around 3 s post-bounce, the luminosities of the GR model than gets higher than those of the p-newt model, for all three flavors. This behaviour is seen in all three EoS only the point of time when the luminosities of the GR model getting higher than those of the post-Newtonian model differ. The behaviour of the mean energies is similar. The GR models have lower energies at the beginning and higher mean energies at the end of the simulations, compared to the post-Newtonian models. This is seen in all three flavors and all three EoS. Again the point when the energies of the GR model gets higher than the p-newt model differs between the EoS.

This is expected, as the total emitted energy is the same for both models the gravitational binding energy of the proto neutron star. (H udepohl (2009) found that also the effective potential approach reproduces this very well.) The luminosity of a model which starts with a higher value therefore must, at some point, drop below the other one. M uller et al. (2010) see similar results for the first 4 s in their Figure 11.

In Table 3.7 we show values of the neutrino signal and the proto neutron star radius for each EoS at 1.8 s. We choose this point as around this time the LS180 and SKA EoS models have their maxima for the mean energies We see that the relative differences between the GR and post-Newtonian models of those two models are similar, both for the luminosities and the energies. The relative differences are around half as much for the SHEN EoS model. The higher luminosities of the p-newt models can be partially explained by their higher proto neutron star radius, see middle panels of Figure 3.30. The mean energies are also higher and we would therefore expect even higher luminosities for the post-Newtonian models. Another effect could be due to the different contraction of the proto neutron star with and without GR.

In Figure 3.30 we show the shock radius, top panels, and proto neutron star radius, middle panels. Additionally we can see the mass outflow rate of the out streaming matter from the proto neutron star in the bottom panel. We see that the shock radius of the GR models is lower than for the post-Newtonian model. This is due to the large velocities of the post-Newtonian models which can be up to 5 c. It also shows that the GR model explodes slightly later than the post-Newtonian model. The mass outflow of the GR models is for the first 2 s lower than in the



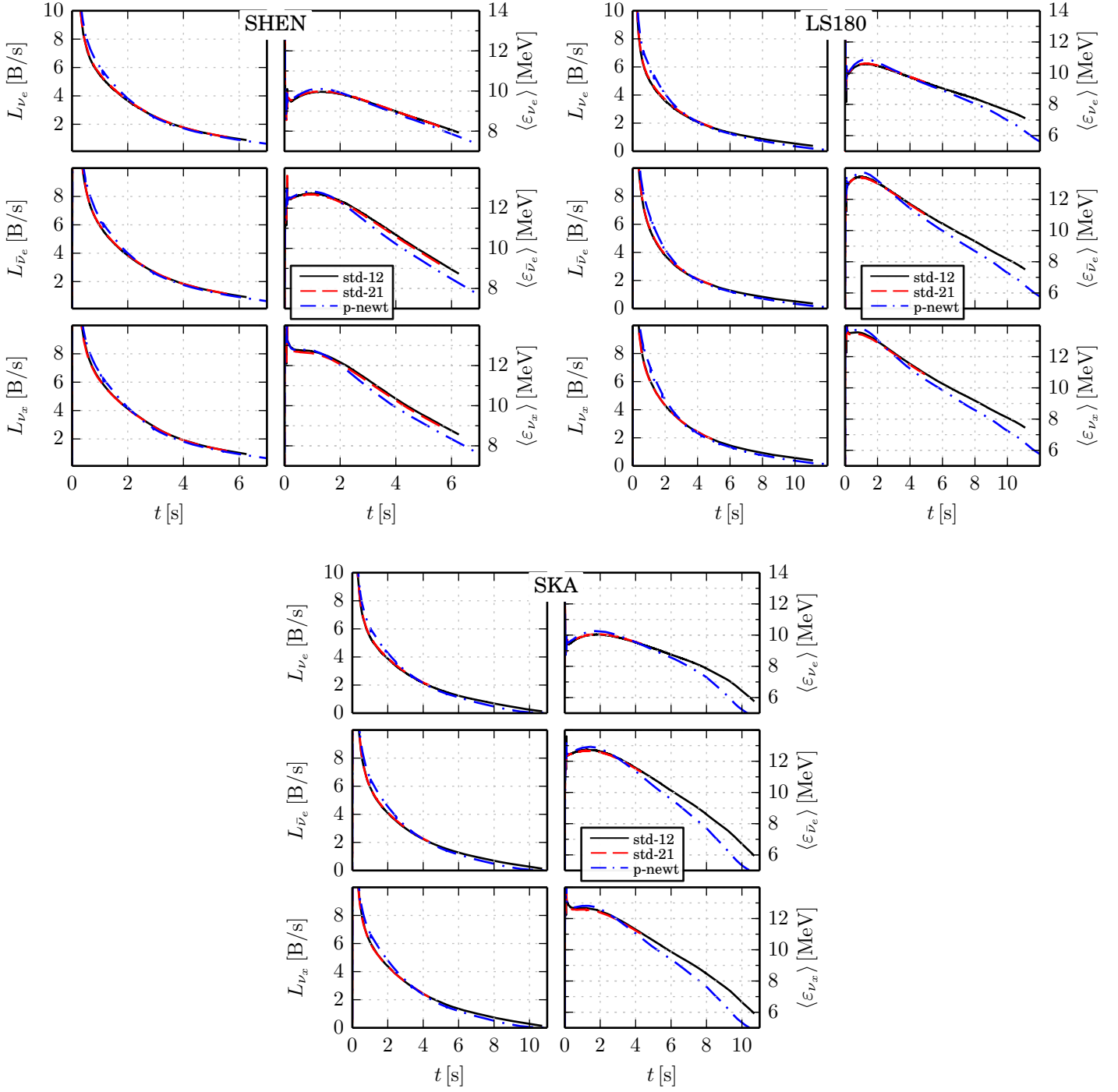


**Figure 3.29:** The neutrino cooling signal of the GR and post-Newtonian models.



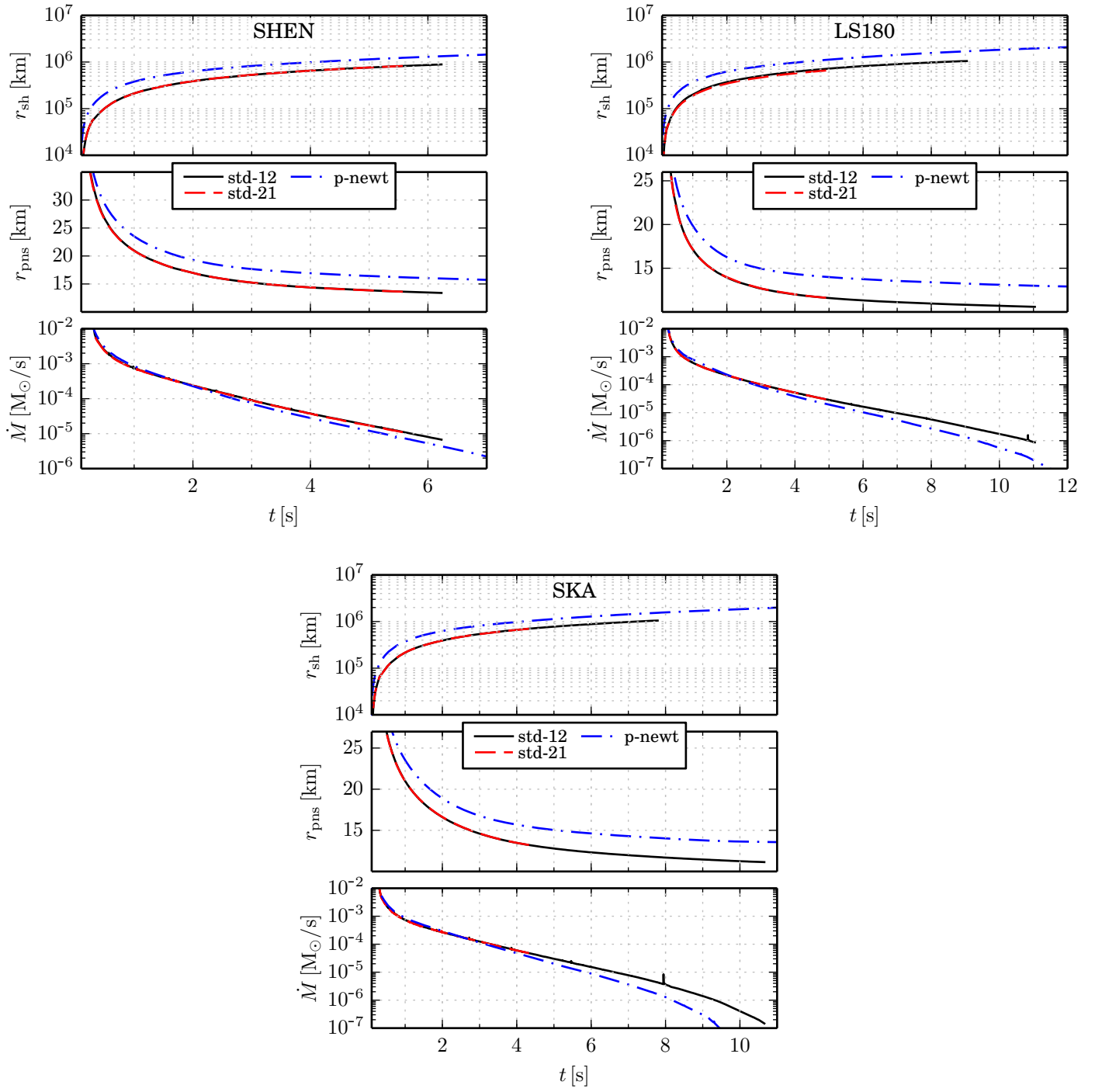


**Figure 3.30:** Shock radius, proto neutron star radius and mass outflow rate during the cooling phase for the GR and post-Newtonian models.



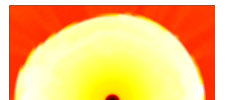
**Table 3.7:** The values of the luminosities and mean energies at 1.8 s, for the GR and post-Newtonian models.

Model	LS180							
	$L_{\nu_e}$ [B/s]	$L_{\bar{\nu}_e}$ [foe/s]	$L_{\nu_x}$ [foe/s]	$\langle \varepsilon_{\nu_e} \rangle$ [MeV]	$\langle \varepsilon_{\bar{\nu}_e} \rangle$ [MeV]	$\langle \varepsilon_{\nu_x} \rangle$ [MeV]	$r_{\text{pns}}$ [km]	$t$ [s]
p-newt-1D	4.42	4.61	5.17	10.78	13.39	13.29	16.71	1.8
std-12-1D	3.84	4.07	4.61	10.51	13.16	13.11	14.33	1.8
Model	SHEN							
	$L_{\nu_e}$ [B/s]	$L_{\bar{\nu}_e}$ [foe/s]	$L_{\nu_x}$ [foe/s]	$\langle \varepsilon_{\nu_e} \rangle$ [MeV]	$\langle \varepsilon_{\bar{\nu}_e} \rangle$ [MeV]	$\langle \varepsilon_{\nu_x} \rangle$ [MeV]	$r_{\text{pns}}$ [km]	$t$ [s]
p-newt-1D	4.18	4.40	4.62	10.01	12.48	12.23	19.84	1.8
std-12-1D	3.96	4.16	4.45	9.91	12.49	12.31	17.46	1.8
Model	SKA							
	$L_{\nu_e}$ [B/s]	$L_{\bar{\nu}_e}$ [foe/s]	$L_{\nu_x}$ [foe/s]	$\langle \varepsilon_{\nu_e} \rangle$ [MeV]	$\langle \varepsilon_{\bar{\nu}_e} \rangle$ [MeV]	$\langle \varepsilon_{\nu_x} \rangle$ [MeV]	$r_{\text{pns}}$ [km]	$t$ [s]
p-newt-1D	4.59	4.89	5.13	10.26	12.87	12.71	19.52	1.8
std-12-1D	4.10	4.36	4.64	10.04	12.69	12.56	17.19	1.8

post-Newtonian case and after that higher (depending on the EoS). This fits with the lower proto neutron star radius and the lower mean energy for the first seconds.

### 3.5.2 Nucleon potentials

In Figure 3.31 and Figure 3.32 we see the comparison of the models with (np-12) and without (std-12) the corrected neutrino nucleon opacities for each EoS, over several seconds. We see that the trend we observed in Section 3.4.2 for the luminosities continues also for the first few seconds. The luminosities of all three flavors are lower for the model with the corrections than for the std-12 model. Also the mean energies for the np-12 model of the  $\nu_e$  and  $\nu_x$  stay below the std-12 model. We stated in Section 3.4.2 that in the case of the  $\langle \varepsilon_{\bar{\nu}_e} \rangle$  the energies are higher for the model with than for the model without corrected nucleon opacities after the first 0.5 s. We see now that around 1 s, depending on the EoS, the energy of the model with the correction drops below the model without them. We see that over the long timescale the luminosities and mean energies of the two models are coming closer together again. Eventually, the np-12 model ends up with higher luminosities and mean energies than the std-12 model. The point when this happens depends on the EoS. But all EoS models have in common that it happens earlier for the  $\bar{\nu}_e$  and  $\nu_x$  than for the  $\nu_e$ . This behaviour of the models with and without the



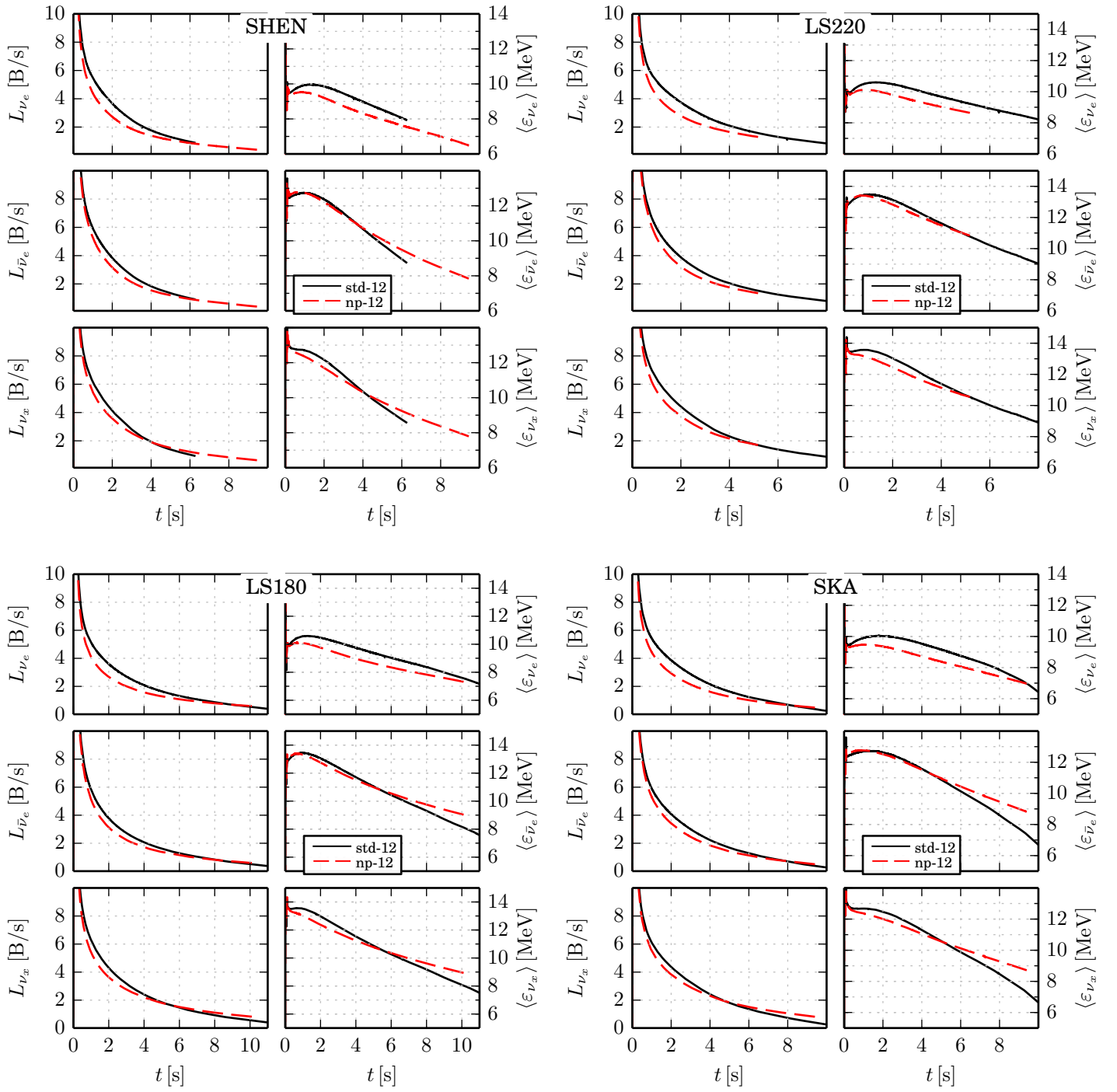


**Figure 3.31:** Comparing the neutrino signal for the models done with and without corrected neutrino nucleon opacities.



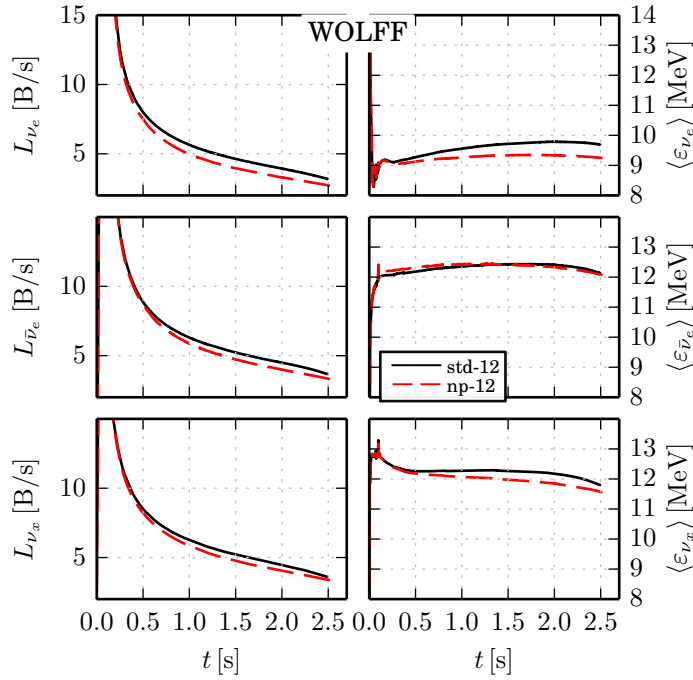


**Figure 3.32:** As Figure 3.31 but for the WOLFF EoS.

corrected neutrino nucleon opacities is also seen by H\"udepohl (2014), see his Figure 5.9.

The models with the WOLFF EoS, Figure 3.32 build a small exception as the EoS is not tabulated in such a large parameter space as the other EoS are so we were only able to simulate up to  $\approx 2.5$  s, where parts of the simulation started to exceed the tabulated region. In this case the luminosities and mean energies of the model with the corrected opacities are still below the model without them.

Summarising, we see that the cooling time for the corrected neutrino nucleon opacities models differs from std-12 model, this is also found by Mart\'inez-Pinedo et al. (2012); Roberts et al. (2012a); H\"udepohl (2014). In difference to Mart\'inez-Pinedo et al. (2012) we see that the mean energies for the anti-electron neutrinos can also be decreased rather than increased for the corrected opacity models. This agrees with H\"udepohl (2014), here we can make a more direct comparison as he has also done simulations with a lower mass star (s11.2), whereas the 15 solar mass star of Mart\'inez-Pinedo et al. (2012) has also a more massive proto neutron star. Also Roberts (2012c) comes to this result after they fixed a numerical bug in their implementation of Roberts (2012). But overall, all agree that the main influence of the corrected opacities is on the electron neutrinos and by that also on the wind electron fraction. We can see the effect of the nuclear potentials on the electron neutrinos also in Figure 3.33. Here the corrected model shows a higher  $Y_e$  and  $Y_{\nu_e}$ , especially at 2 s, than the model without corrected neutrino nucleon opacities. We



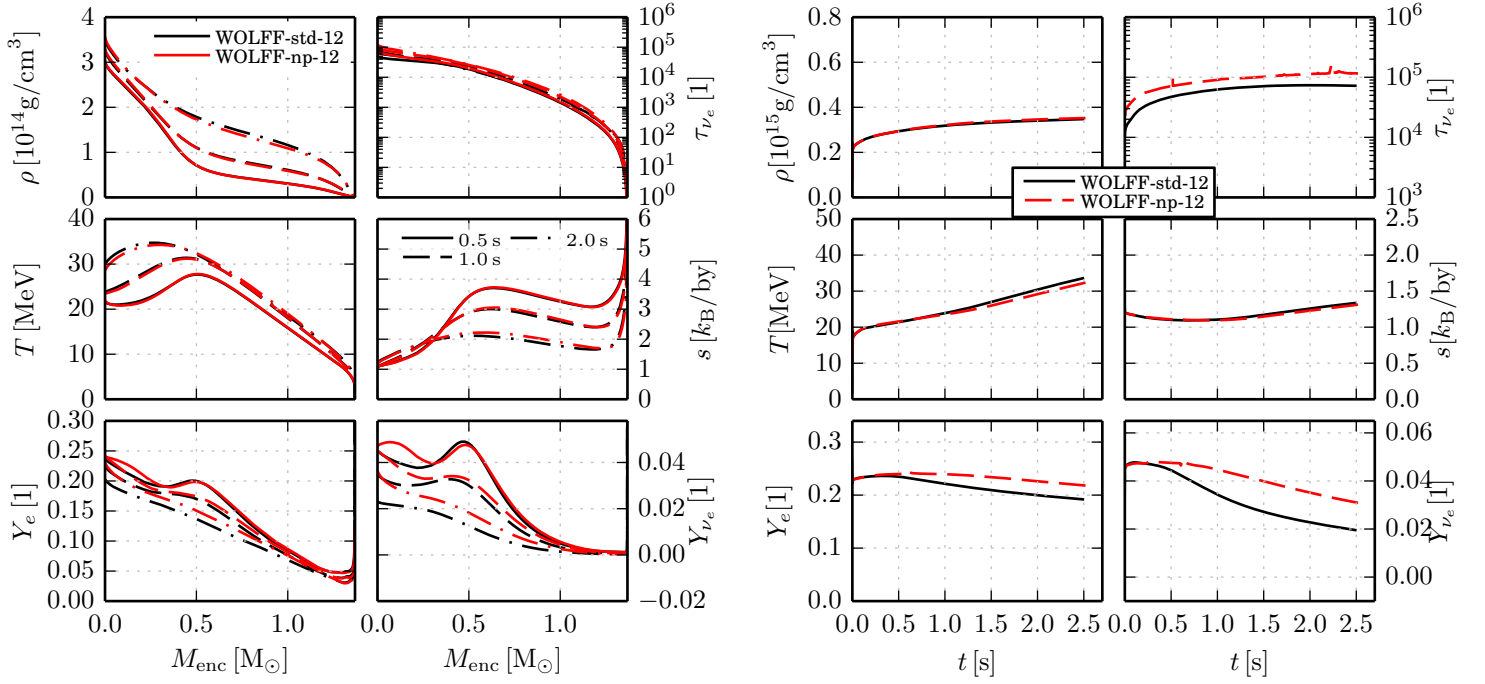


**Figure 3.33:** The left hand side shows the time-evolution of profiles of the matter density  $\rho$ , temperature  $T$ , electron fraction  $Y_e$ , electron neutrino optical depth  $\tau_{\nu_e}$ , matter entropy  $s$ , and net electron neutrino per baryon fraction  $Y_{\nu_e}$ , while the right hand side shows the central values of those quantities.

also see that the other quantities are in a good agreement for both models.

### 3.5.3 Convection

Hüdepohl (2014) noted that the difference between a standard model and the corrected neutrino nucleon opacities is bigger than the difference between simulations done with convection and with both convection and corrected opacities for the EoSs he used. A suitable set of models to look at this is only available for the WOLFF EoS, as we see in Figure 3.34. The WOLFF EoS is quite stiff and the effect on the different models less pronounced compared to the other EoS. We do not see the difference as clearly as Hüdepohl (2014). In this case the difference between the models with convection (con, con-np) is similar to the difference of the models without convection (std-12, np-12). The same is true if we consider the relativistic convection treatment.

In Figure 3.35 we look directly at the cooling of the proto neutron star. We see that the matter density, the electron neutrino optical depth  $\tau_{\nu_e}$ , and temperature are fairly similar for all shown models. In the case of the entropy we see that the convection treatment smoothes out the entropy gradient. This is done more



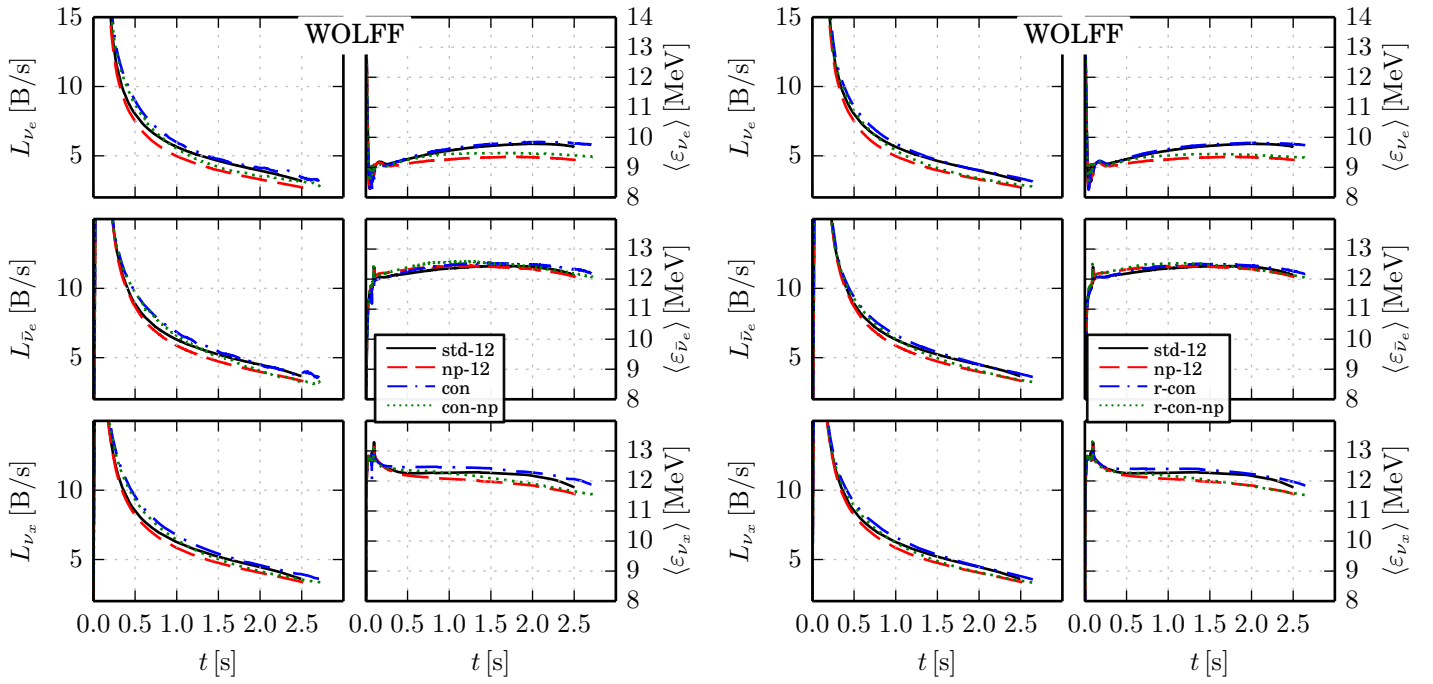
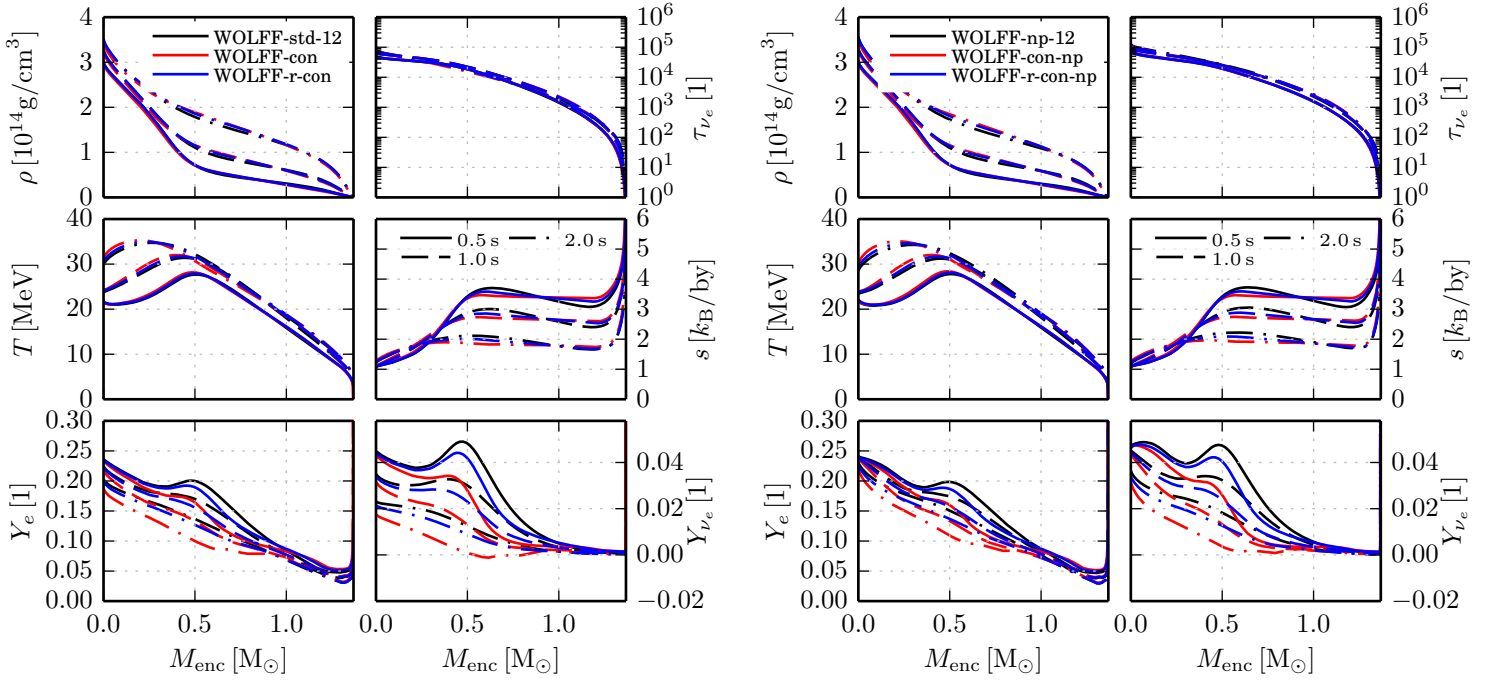


**Figure 3.34:** Comparison of the neutrino signal of models with (np-12) and without (std-12) the corrected neutrino nucleon opacities to models with Newtonian convection (right panels) and relativistic convection (left panels), also with and without corrected opacities.

efficiently by the model with the Newtonian convection treatment than by the model with the relativistic convection treatment. We also see that for the models with convection the  $Y_e$  shrinks faster than without convection, left panel, and this effect is a little bit reduced for the models with convection and with corrected neutrino nucleon opacities, right panel. This is also nicely seen for the central  $Y_e$  and  $Y_{\nu_e}$  in Figure 3.36.

In Figures 3.37 – 3.38 we display the neutrino signal of all available models with the five different EoSs. Note that from here on the convective (con-np/ r-con-np) model and the non-convective (np-12) model, which we will compare with each other, are both simulated with the corrected neutrino nucleon opacities. We see that the luminosities, for all flavors, of the convective models are higher than the one of the non-convective model for at least the first second, for all EoSs. The same is true for all flavors for the mean energies. After the first second the behaviour of the convective models more strongly depend on the EoS. In case of the SHEN EoS the convective models have not progressed much further than the first second. For the LS220 we see that as long as the simulations last the luminosities of the convective models are higher than the non-convective model, for all flavors. The luminosities of the Newtonian convective model stays even higher than the one

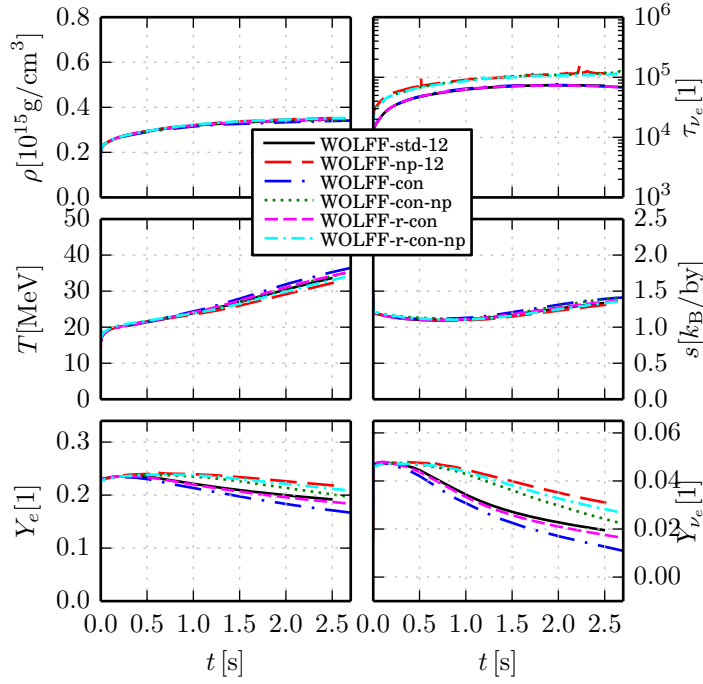




**Figure 3.35:** Comparing the hydrodynamical evolution of the models with the WOLFF EoS, with and without (Newtonian and relativistic) convection. On the left hand side we show the models without corrected neutrino nucleon opacities, on the right hand side models with the correction.

without convection and corrected neutrino nucleon opacities (std-12). Note that the relativistic convective model with the LS220 EoS is one of the models where the outer hull exploded during the collapse, but we do not really expect to see a sign of that in the neutrino cooling signal, especially at this late times. For the luminosities it nearly follows the std-12 model and has values which are between the values of the Newtonian convective and non-convective models. For the mean energies we see the same picture. The convective models stay above the non-convective models for the simulated time. Also for the anti-electron and heavy-lepton neutrinos the energies of the Newtonian convection model is higher than the std-12 model. The energies for the relativistic convection model are between the values of the Newtonian convection and the non-convective models. A similar behaviour is also seen for the LS180 EoS models. The SKA EoS models shows a different picture: The convective models do not stay above the non-convective or std-12 model for the simulated time. Actually the luminosities of the Newtonian convection model are lower after  $\sim 3$  s than the non-convective model, for all flavors. (The convection model with the relativistic treatment could not be simulated that long.) Also the energies of the model with the Newtonian convection criterion are first higher and after around  $\sim 3$  s below the non-convective model, for all flavors. In the case of

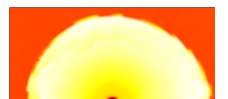




**Figure 3.36:** Central quantities for models with and without convection, and with and without corrected neutrino nucleon opacities, for the WOLFF EoS models.

the WOLFF EoS all models have reached the end of the possible simulation time. The models with the WOLFF EoS are quite similar to each other. The luminosities of the convective model are higher than those of the model without convection but come quite close if not equal to the end of the simulation. This is also the case for the mean energies.

The different behaviour of the convection models with different EoS was also found by Roberts et al. (2012b) and Hüdepohl (2014). Roberts et al. (2012b) states that the convection region is sensitive to the behaviour of the symmetry energy of the EoS, specifically the parameter  $J$  of Table 2.1.



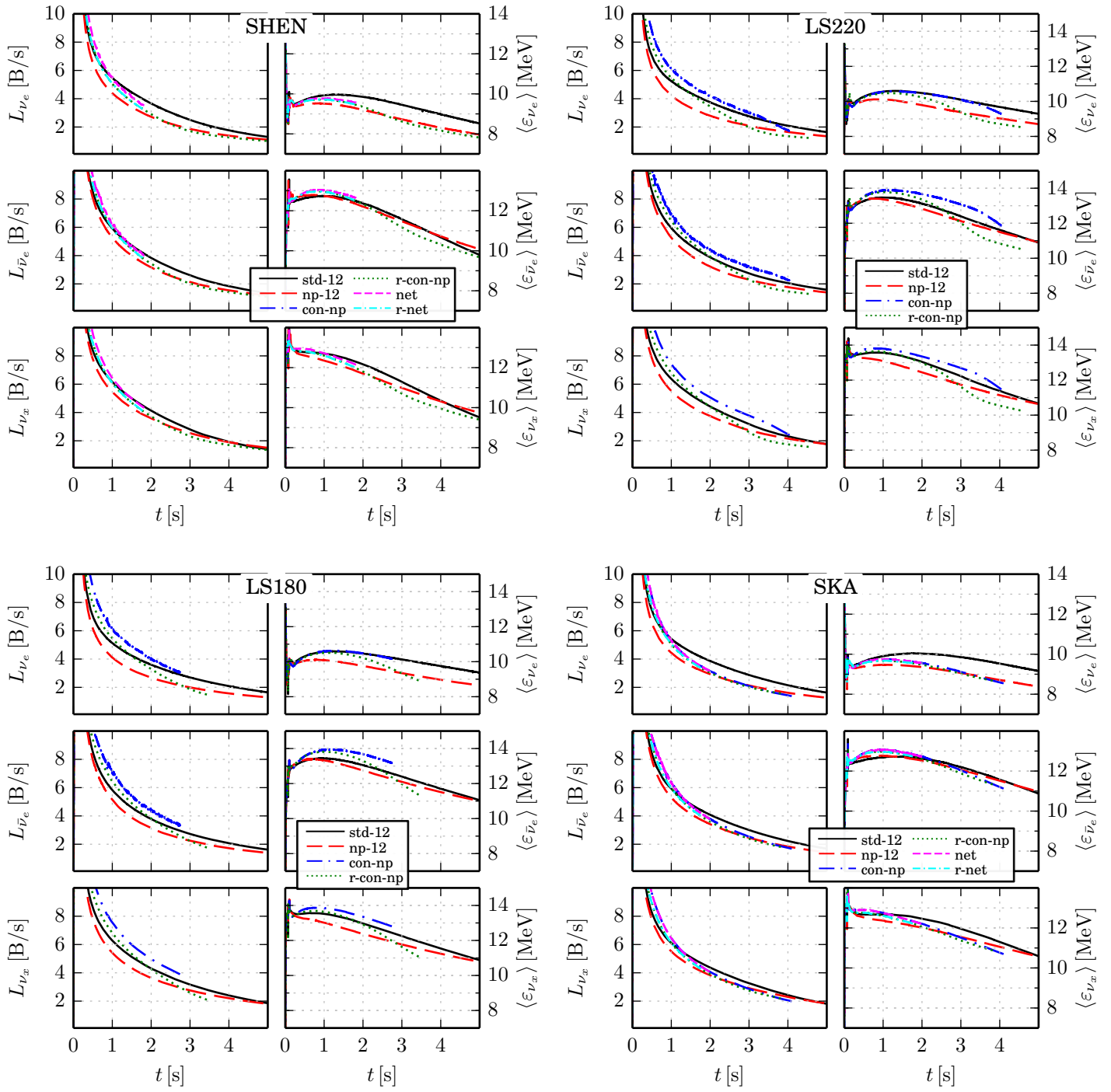
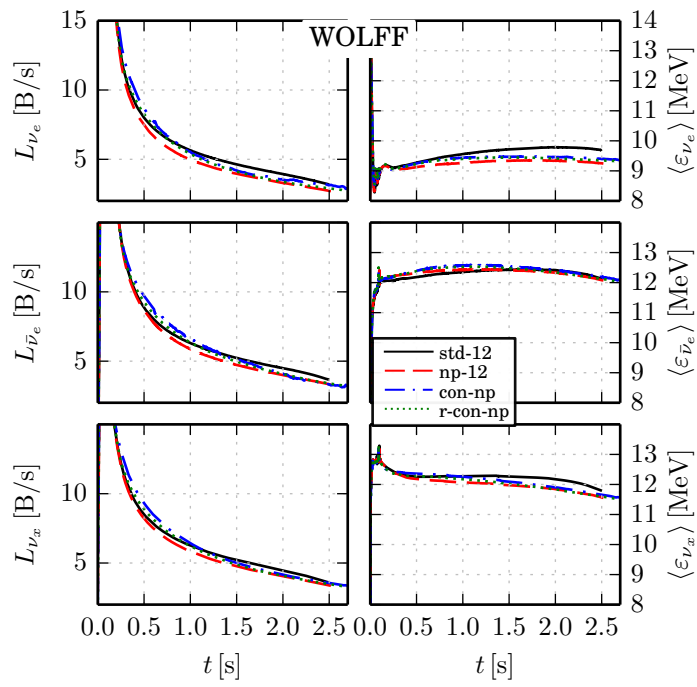


Figure 3.37: Neutrino signal for all models of four different EoS





**Figure 3.38:** As Figure 3.37 but for the WOLFF EoS.



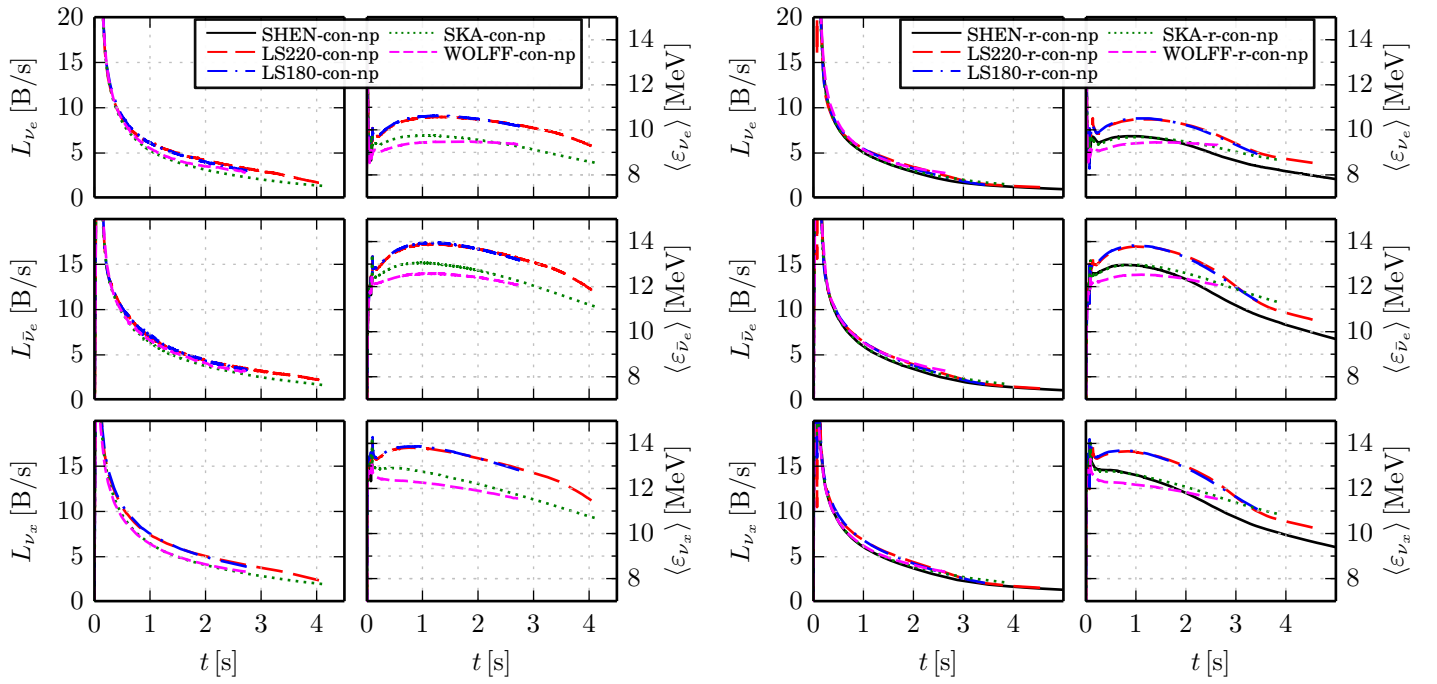


**Figure 3.39:** Comparing the effect of different EoS on the neutrino signal for the best physics models.

### 3.5.4 EoS

Finally we also want to make a direct comparison of the EoS to each other. In Figure 3.39 we show the neutrino signal for the models with the convective treatment and all five EoS. On the left hand side we show the models with the Newtonian convective treatment. We see that the luminosities for the different EoS models are very similar for the first  $\sim 0.5$ s. After that, the luminosities of the models evolve differently to each other but in the same manner for each flavor. At the end of the simulation the models with the LS220 and LS180 EoS are very similar to each other and they have the highest luminosities, for all flavors. The model with the WOLFF EoS lies between the luminosities of the models with the LS180 and LS220 EoS followed closely by the model with the SKA EoS.

The LS180 and LS220 EoS models have also very similar mean energies, again the highest of all models. The model with the SKA EoS has at the beginning higher mean energies than the model with the WOLFF EoS. But for the electron neutrinos the mean energy of the WOLFF EoS model gets higher than the SKA EoS model at the end of the simulation.

For the models with the relativistic convection treatment we see a slightly different behaviour, see right panel of Figure 3.39. Additionally, the model with the SHEN EoS has progressed further for this case and we can see that at the end of



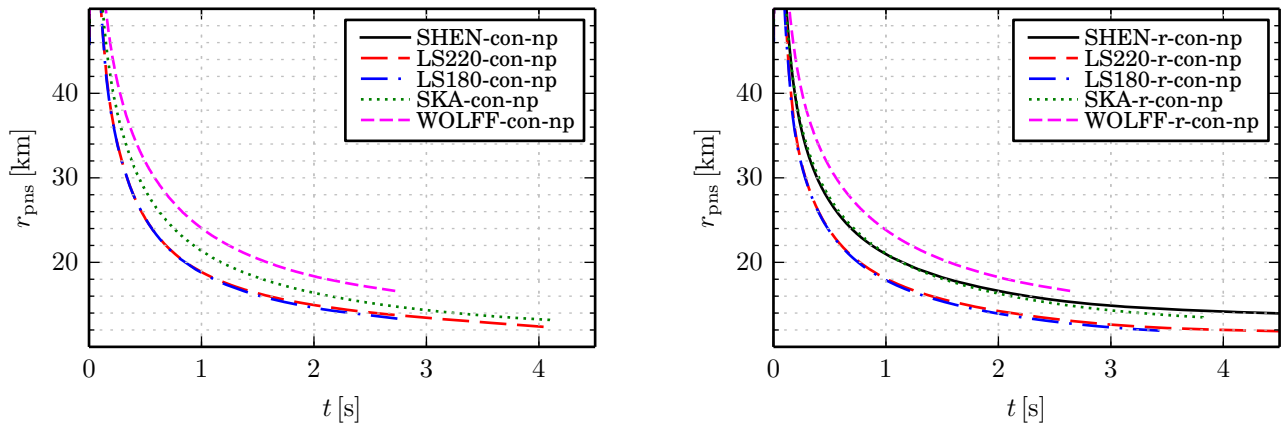


**Figure 3.40:** Comparing the effect of different EoS on the proto neutron star radius.

the simulations it has the lowest luminosities and mean energies. We see that the models with the LS180 and LS220 EoS get lower luminosities and mean energies earlier than in the Newtonian convection case.

We can see this behaviour also for the proto neutron star radii, see Figure 3.40. The proto neutron star for the LS180 and LS220 EoS models contracts faster in the case of the relativistic convection treatment than in the Newtonian convection treatment. In contrast to that is the behaviour of the other EoS models, which are more similar in both cases. Additionally we see in Figure 3.40 the influence of the different EoS itself on the proto neutron star radius. The model with the stiffest EoS (WOLFF) has the highest radius whereas the model with the softest EoS (LS180) has the lowest radius.

In Figure 3.41 we see the evolution of certain central quantities. We see how the different EoS influence the central density and entropy very strongly. Also we see how the Newtonian convection treatment model reaches the maximal core temperature faster for the LS220 EoS model than the other EoS models and also faster than in the relativistic convection treatment.

Table 3.8 and 3.9 give a summary about interesting quantities of the simulations. The proto neutron star mass is e.g. needed by Blaschke et al. (2014) to constrain their Equation of State. As we define the proto neutron star radius at an arbitrary density contour of  $\rho = 10^{11}$  g/cm<sup>3</sup> we also give values for the density contour of  $\rho = 10^9$  g/cm<sup>3</sup> to assess the influence of this definition. We see that with the convection the cooling proceeds much more rapidly. Note that for the WOLFF EoS no completely cold configuration could be used.

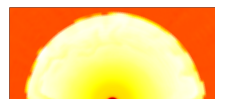


**Table 3.8:** This tables sums up the properties of the proto neutron star at the end of the simulations .  $t_{\text{end}}$  gives the end of the simulated time,  $r_{\text{pns}}$  the proto neutron star radius defined as the density contour of  $\rho = 10^{11} \text{ g/cm}^3$ ,  $M_{\text{pns}}$  the associated baryonic proto neutron star mass,  $M_{\text{G}}$  the associated baryonic gravitational mass.  $r'_{\text{pns}}$  gives the proto neutron star radius defined as the density contour of  $\rho = 10^9 \text{ g/cm}^3$ ,  $M'_{\text{pns}}$  the associated baryonic proto neutron star mass,  $M'_{\text{G}}$  the associated baryonic gravitational mass. (Note that we use in our code a baryon mass of  $1.66 \cdot 10^{-24} \text{ g}$ )  $E_{\nu}$  is the total emitted neutrino energy for all flavors up to  $t_{\text{end}}$ , and  $N_L$  total radiated net Lepton number, in brackets also as a fraction of the available gravitational binding energy for an ideal TOV solution with that baryon mass.

Model	LS180									
	$t_{\text{end}}$ [s]	$r_{\text{pns}}$ [km]	$M_{\text{pns}}$ [ $M_{\odot}$ ]	$M_{\text{G}}$ [ $M_{\odot}$ ]	$r'_{\text{pns}}$ [km]	$M'_{\text{pns}}$ [ $M_{\odot}$ ]	$M'_{\text{G}}$ [ $M_{\odot}$ ]	$E_{\nu}$ [ $B$ ]	$N_L$ [1]	$N_L$ [ $10^{56}$ ] [1]
con-np-1D	2.742	13.3	1.3658	1.2891	16.0	1.3659	1.2892	137 (0.70)	6.49	(0.94)
np-12-1D	10.100	10.8	1.3695	1.2738	11.8	1.3695	1.2739	171 (0.86)	6.20	(0.90)
r-con-np-1D	3.432	11.9	1.3689	1.2945	13.6	1.3689	1.2946	133 (0.67)	5.70	(0.83)
std-12-1D	11.041	10.6	1.3687	1.2641	11.5	1.3688	1.2641	187 (0.95)	6.79	(0.99)
std-21-1D	4.914	11.6	1.3686	1.2835	13.3	1.3686	1.2835	152 (0.77)	6.20	(0.90)

Model	LS220									
	$t_{\text{end}}$ [s]	$r_{\text{pns}}$ [km]	$M_{\text{pns}}$ [ $M_{\odot}$ ]	$M_{\text{G}}$ [ $M_{\odot}$ ]	$r'_{\text{pns}}$ [km]	$M'_{\text{pns}}$ [ $M_{\odot}$ ]	$M'_{\text{G}}$ [ $M_{\odot}$ ]	$E_{\nu}$ [ $B$ ]	$N_L$ [1]	$N_L$ [ $10^{56}$ ] [1]
con-np-1D	4.042	12.4	1.3669	1.2777	14.3	1.3670	1.2778	159 (0.82)	6.81	(0.97)
np-12-1D	5.179	11.9	1.3707	1.2926	13.5	1.3707	1.2927	140 (0.72)	5.73	(0.82)
r-con-np-1D	4.534	11.8	1.3718	1.2908	13.3	1.3718	1.2909	145 (0.74)	5.89	(0.84)
std-12-1D	8.008	11.3	1.3685	1.2705	12.5	1.3685	1.2706	175 (0.90)	6.73	(0.96)
std-21-1D	4.686	12.1	1.3686	1.2846	13.8	1.3686	1.2846	150 (0.77)	6.28	(0.90)

Model	SKA									
	$t_{\text{end}}$ [s]	$r_{\text{pns}}$ [km]	$M_{\text{pns}}$ [ $M_{\odot}$ ]	$M_{\text{G}}$ [ $M_{\odot}$ ]	$r'_{\text{pns}}$ [km]	$M'_{\text{pns}}$ [ $M_{\odot}$ ]	$M'_{\text{G}}$ [ $M_{\odot}$ ]	$E_{\nu}$ [ $B$ ]	$N_L$ [1]	$N_L$ [ $10^{56}$ ] [1]
con-np-1D	4.099	13.2	1.3667	1.2889	15.0	1.3668	1.2889	139 (0.75)	6.12	(0.91)
net-1D	1.983	16.4	1.3664	1.3078	19.9	1.3666	1.3079	105 (0.56)	5.88	(0.87)
np-12-1D	9.399	11.7	1.3692	1.2756	12.8	1.3692	1.2756	167 (0.90)	6.29	(0.93)
r-con-np-1D	3.818	13.5	1.3682	1.2954	15.5	1.3682	1.2955	130 (0.70)	5.81	(0.86)
r-net-1D	1.762	17.0	1.3701	1.3169	20.8	1.3703	1.3171	95 (0.51)	5.49	(0.81)
std-12-1D	10.657	11.1	1.3680	1.2679	11.9	1.3680	1.2680	179 (0.96)	6.72	(0.99)
std-21-1D	4.330	13.2	1.3680	1.2878	15.3	1.3681	1.2878	143 (0.77)	6.31	(0.93)



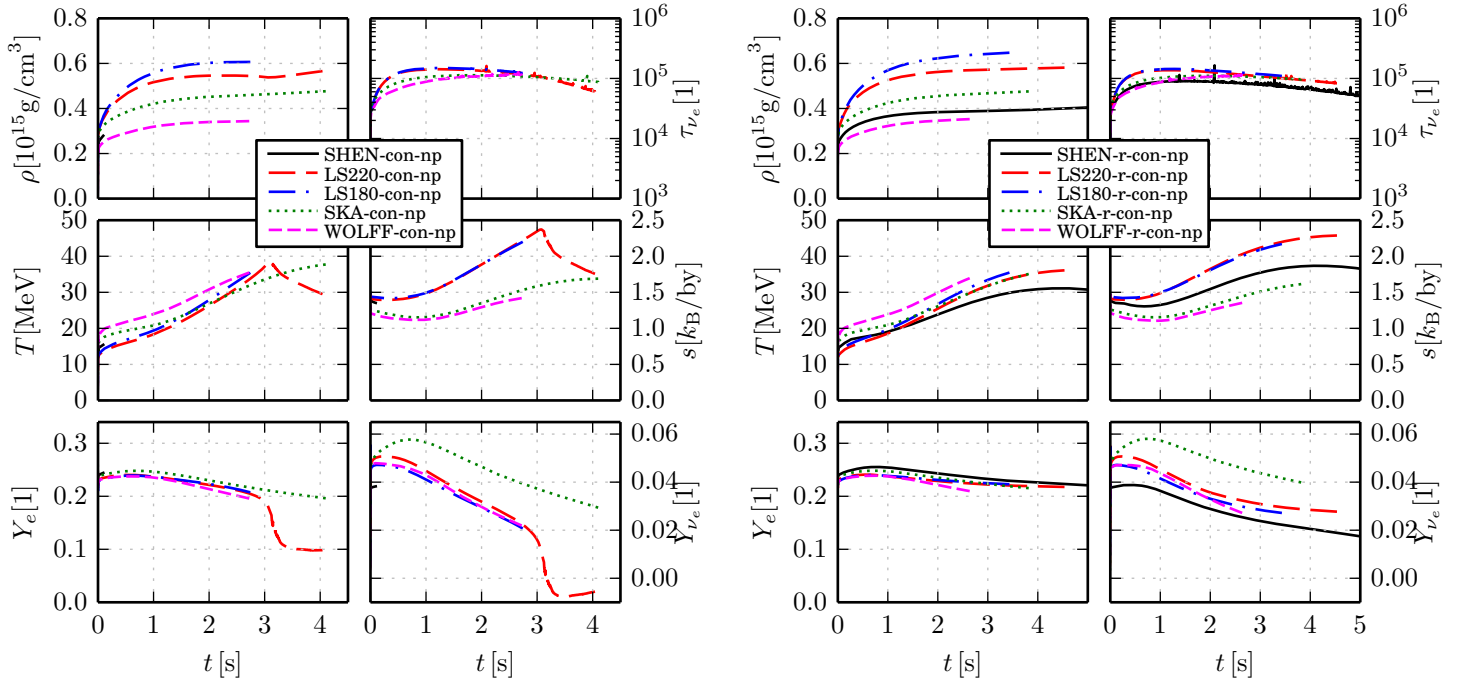


**Figure 3.41:** Time evolution of the central values of the matter density  $\rho$ , temperature  $T$ , electron fraction  $Y_e$ , electron neutrino optical depth  $\tau_{\nu_e}$ , matter entropy  $s$ , and net electron neutrino per baryon fraction  $Y_{\nu_e}$ , for the convective models with different EoS.



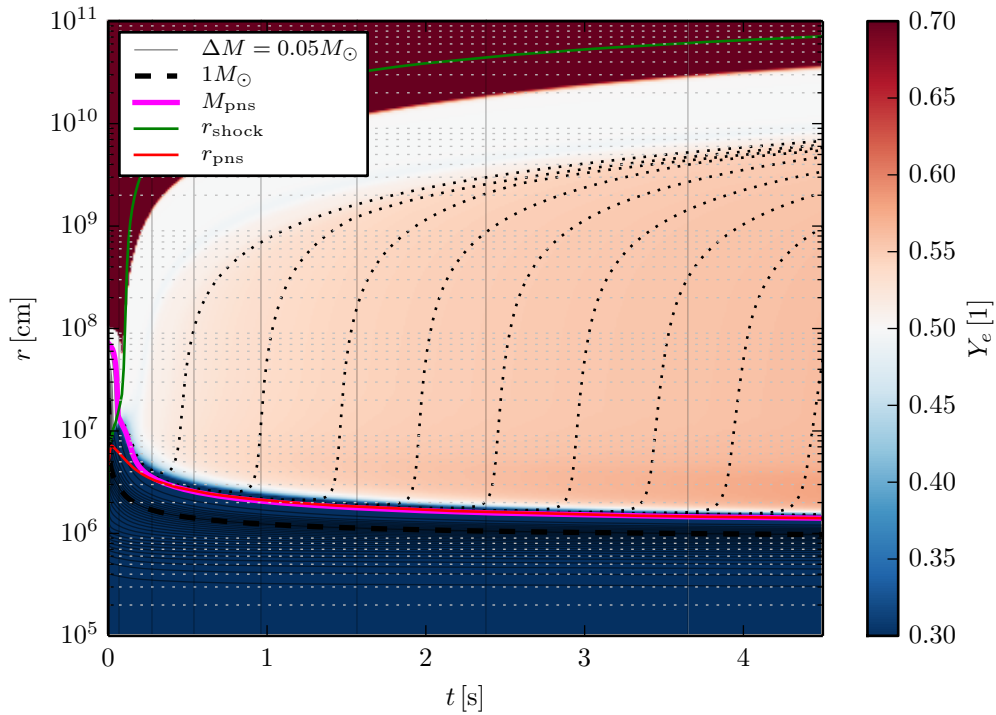
**Table 3.9:** As Table 3.8 but for the SHEN and WOLFF EoSs

Model	SHEN										
	$t_{\text{end}}$ [s]	$r_{\text{pns}}$ [km]	$M_{\text{pns}}$ [ $M_{\odot}$ ]	$M_{\text{G}}$ [ $M_{\odot}$ ]	$r'_{\text{pns}}$ [km]	$M'_{\text{pns}}$ [ $M_{\odot}$ ]	$M'_{\text{G}}$ [ $M_{\odot}$ ]	$E_{\nu}$ [ $B$ ]	[1]	$N_L$ [ $10^{56}$ ]	[1]
net-1D	1.822	17.5	1.3673	1.3104	21.4	1.3675	1.3106	102	(0.60)	6.00	(0.91)
np-12-1D	9.447	12.9	1.3664	1.2793	14.0	1.3665	1.2794	156	(0.92)	6.20	(0.94)
r-con-np-1D	5.286	13.7	1.3688	1.2910	15.3	1.3688	1.2911	139	(0.82)	6.00	(0.91)
r-net-1D	1.780	17.2	1.3703	1.3166	21.0	1.3704	1.3168	96	(0.57)	5.55	(0.84)
std-12-1D	6.231	13.4	1.3681	1.2827	15.0	1.3681	1.2828	153	(0.90)	6.49	(0.98)
std-21-1D	5.572	13.6	1.3671	1.2841	15.3	1.3672	1.2841	148	(0.88)	6.45	(0.97)

Model	WOLFF										
	$t_{\text{end}}$ [s]	$r_{\text{pns}}$ [km]	$M_{\text{pns}}$ [ $M_{\odot}$ ]	$M_{\text{G}}$ [ $M_{\odot}$ ]	$r'_{\text{pns}}$ [km]	$M'_{\text{pns}}$ [ $M_{\odot}$ ]	$M'_{\text{G}}$ [ $M_{\odot}$ ]	$E_{\nu}$ [ $B$ ]	[1]	$N_L$ [ $10^{56}$ ]	[1]
con-np-1D	2.723	16.6	1.3643	1.2970	20.0	1.3645	1.2972	120	(0.69)	6.49	(0.97)
np-12-1D	2.518	16.9	1.3679	1.3070	20.4	1.3681	1.3072	109	(0.62)	5.95	(0.89)
r-con-np-1D	2.638	16.6	1.3659	1.3013	20.0	1.3661	1.3015	115	(0.66)	6.13	(0.92)
std-12-1D	2.489	16.8	1.3661	1.3023	20.5	1.3663	1.3024	114	(0.65)	6.17	(0.92)
std-21-1D	2.457	16.9	1.3639	1.3006	20.6	1.3641	1.3008	113	(0.65)	6.19	(0.93)





**Figure 3.42:** Evolution of mass shells over time for the SHEN std-12 model. Colour coded is the electron fraction  $Y_e$  over time. The green line represents the radius of the explosion shock, the black dotted lines are mass shell at a distance of 0.5 s and are  $M_{pns} + (138.2, 73.8, 46.2, 30.5, 21.1, 15.2, 11.6, 9.3) \cdot 10^{-5} M_{\odot}$ , the dark red line is the proto neutron star radius and the magenta line indicates the mass shell of the final proto neutron star mass.

### 3.6 Neutrino Driven Wind

When the proto neutron star cools mass gets ejected, called the neutrino driven wind (Duncan et al., 1986). To illustrate the wind, we show in Figure 3.42 the mass outflow and its  $Y_e$  with selected mass shells. We see how mass from the surface of the proto neutron star radius gets ejected. The proto neutron star itself is of course very neutron rich and the neutrino driven wind carries matter directly from the proto neutron star's surface. It is natural to assume that this could be a site for r-process nucleosynthesis to occur.

Hoffman et al. (1997); Meyer and Brown (1997); Freiburghaus et al. (1999) found that the necessary conditions for an r-process to occur are high entropies, a low expansion timescale (i.e. a fast ejection of matter) and  $Y_e < 0.5$ . Qian (2008) gives a very nice overview of those conditions.



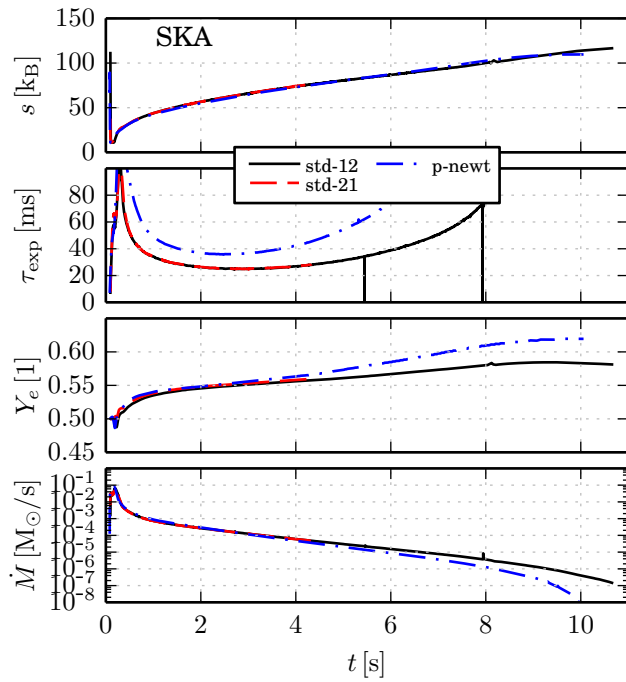
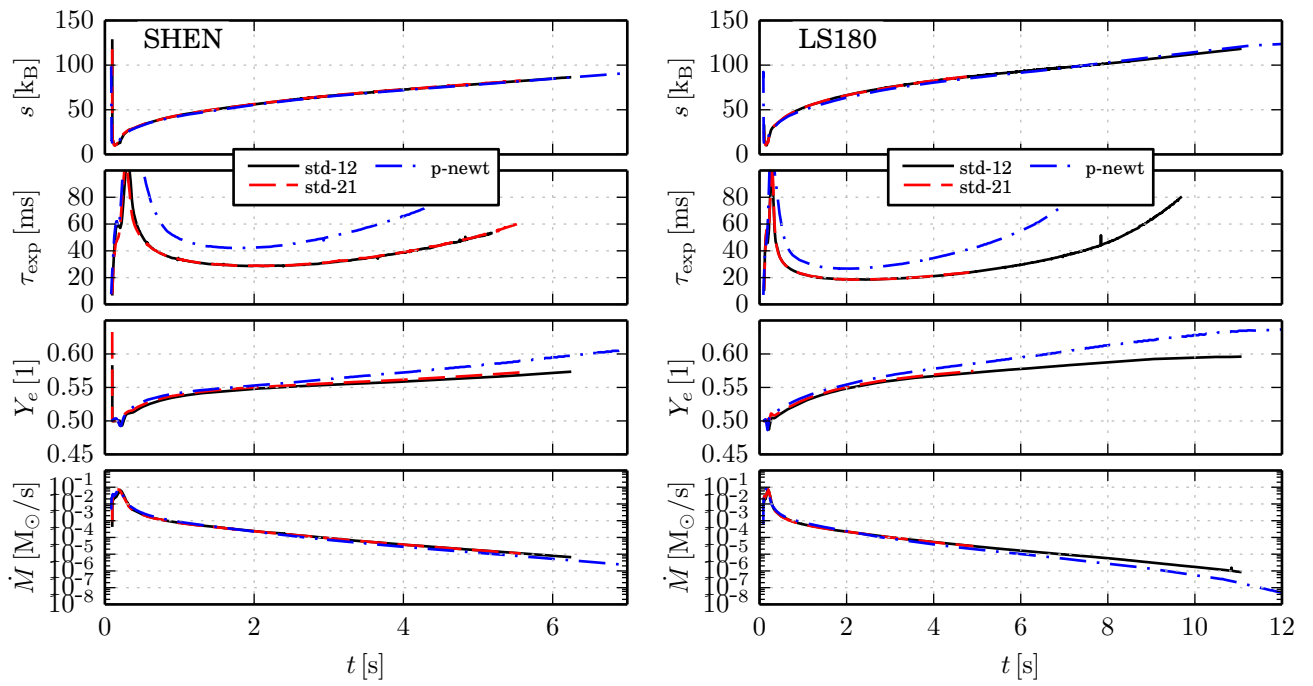


**Figure 3.43:** Properties relevant for the r-process, taken at 500 km. Shown are the entropy  $s$ , expansion timescale  $\tau_{\text{exp}}$ , electron fraction  $Y_e$  and the mass outflow, only values with positive  $\dot{M}$  are shown.

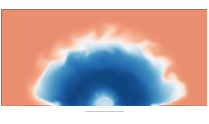


**Table 3.10:** The minimum ejected  $Y_e$  and corresponding values of the entropy and  $\tau_{\text{exp}}$  as well as the time of that minimum value.

Model	LS180			
	$t$ [s]	$Y_e$ [1]	$s$ [k <sub>B</sub> ]	$\tau_{\text{exp}}$ [ms]
p-newt-1D	0.161	0.485	18.49	38.46
std-12-1D	0.189	0.487	18.61	40.77
std-21-1D	0.189	0.500	18.88	42.54

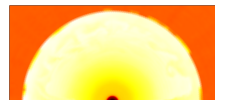
Model	SHEN			
	$t$ [s]	$Y_e$ [1]	$s$ [k <sub>B</sub> ]	$\tau_{\text{exp}}$ [ms]
p-newt-1D	0.180	0.491	18.02	51.84
std-12-1D	0.202	0.493	18.72	44.94
std-21-1D	0.183	0.493	18.74	42.63

Model	SKA			
	$t$ [s]	$Y_e$ [1]	$s$ [k <sub>B</sub> ]	$\tau_{\text{exp}}$ [ms]
p-newt-1D	0.164	0.485	17.59	38.62
std-12-1D	0.198	0.487	19.31	41.24
std-21-1D	0.196	0.499	18.11	46.74

### 3.6.1 GR vs. Post-Newton

In Figure 3.43 we show the interesting quantities for the r-process. In contrast to Otsuki et al. (2000) and Thompson et al. (2001) we don't see a remarkable difference in the entropies of the post-Newtonian and GR models. Otsuki et al. (2000) and Thompson et al. (2001) compared Newtonian and GR simulations. Cardall and Fuller (1997) compared his general relativistic results with the post-Newtonian results of Qian and Woosley (1996) and also find a good agreement of the entropies, as we did. This shows that the post-Newtonian simulations are a relatively good approximation. We also see that the mass loss rate of the GR models is relatively similar to the post-Newtonian model for all three EoSs. In the GR case we have significantly lower expansion timescales than in the post-Newtonian case. This was also found by the tree papers mentioned above. We expected this, as in the post-Newtonian case the velocities can become higher than five times the speed of light, see Figure 3.12, which is of course not possible in the GR case. Interesting is that also the  $Y_e$  has lower values in the GR case than in the post-Newtonian case, at later times. Interestingly we see even some wind matter with  $Y_e < 0.5$  at very

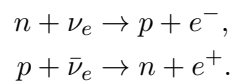


early times after the explosion, while later we get only values above 0.5, indicating a proton rich wind. In Table 3.10 we show the minimal values of  $Y_e$  of each model and EoS. We see that the post-Newtonian models have a lower  $Y_e$  than the GR models. Fuller and Yong-Zhong (1996) wrote that the  $Y_e$  in the relativistic case tends to be closer to 0.5 as a result of the different effect of redshift of the emitted  $\nu_e$  and  $\bar{\nu}_e$ , due to the different locations of their neutrinospheres. Even though, also the post-Newtonian models of Hüdepohl (2009) take redshift into account, the slightly deeper gravitational well in GR thus might be responsible for the difference we see.

Also, the GR models with 21 energy bins have a slightly higher  $Y_e$  than the models with 12 energy bins. The corresponding entropy, during the short time we have a neutron rich wind, is too low and the expansion timescale too high for a classical r-process to occur, cf. Hoffman et al. (1997) and Woosley et al. (1997)

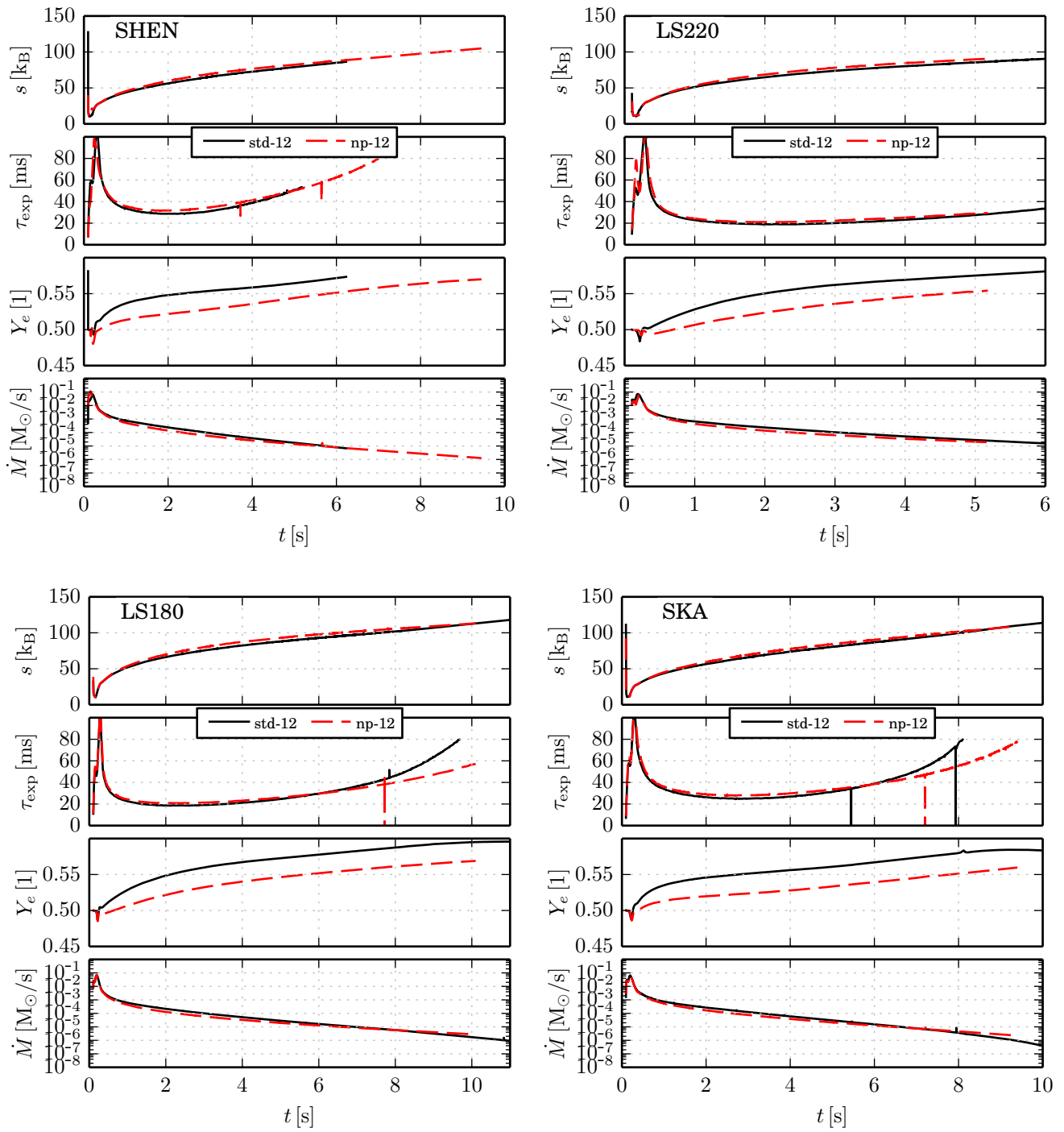
### 3.6.2 Nucleon potentials

We mentioned in Section 3.5.2 that the corrected neutrino nucleon opacities have an influence on the electron fraction. In Figures 3.44 and 3.45 we can see this influence, they show the comparison between the models with and without corrected neutrino nucleon opacities. We see also that the entropies for all five EoS are slightly higher for the models with corrected opacities than for the models without. Also, the  $\tau_{\text{exp}}$  is higher for the np-12 than the std-12 models for all five EoS, up to very late times. In case of the SHEN, LS180 and SKA EoS we see that after around 6 s the expansion time of the np-12 models gets smaller than in the std-12 models. The  $\dot{M}$  of the corrected neutrino nucleon opacity models is lower than for the models without correction for all five EoS for the first  $\sim 7$  s. Also here we see that the mass loss rate for the np-12 model gets slightly higher than in the std-12 models after that point. For the  $Y_e$  we see a huge influence: It is lower for the models with corrected neutrino nucleon opacities, for all five EoS, than for the models without corrections. We expected such a lower values as  $Y_e$  depends on the luminosity and mean energies of electron and anti-electron neutrinos due to  $\beta$ -reaction with matter in the wind,



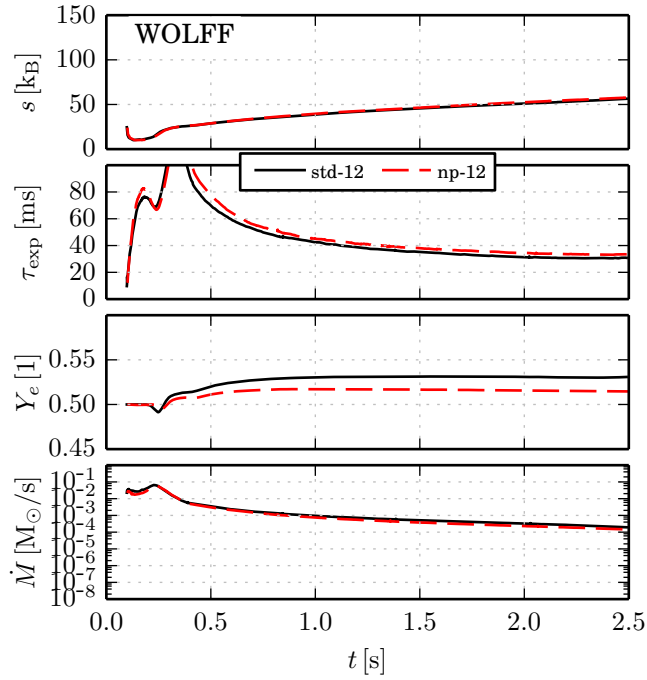
We found in Section 3.5.2 that in most cases the  $\bar{\nu}_e$  and  $\nu_x$  mean energies are higher for the np-12 models than for the std-12 models. This was also found by Roberts (2012c), and Hüdepohl (2014). In the case of the WOLFF EoS we see that the  $Y_e$  of the np-12 model shows a small tendency to get to lower values at the end of the simulation. Sadly, the WOLFF EoS is not tabulated in a large enough parameter space, that we could simulate further. This highlights that with the inclusion of the nuclear potentials, the electron fraction is much more EoS dependent. In Figures 3.44 and 3.45 we see that for the models with corrected opacities we again





**Figure 3.44:** As Figure 3.43 but a comparison between the models with and without corrected neutrino nucleon opacities.

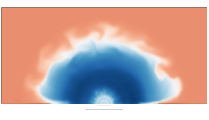




**Figure 3.45:** As Figure 3.44 but with the WOLFF EoS.

have slightly neutron rich early ejecta, also over a longer time than in the case without the corrected opacities. To investigate this further we show in Figures 3.46 and 3.47 mass histograms of the entropy  $s$  and electron fraction  $Y_e$  of the ejecta. We see that we get the necessary high entropies for r-process conditions only for matter which also has  $Y_e > 0.5$ , for all EoS. For only neutron rich ejecta the LS220 model has the highest entropy with  $\sim 42 \text{ k}_B$ . The SHEN EoS model the lowest  $Y_e$  of  $\sim 0.48$ , but at a corresponding entropy of  $\sim 20 \text{ k}_B$ .

Again here the entropy is not high enough for a classical r-process nucleosynthesis. Wanajo (2013), however, states that a “weak r-process” might be possible under those conditions.



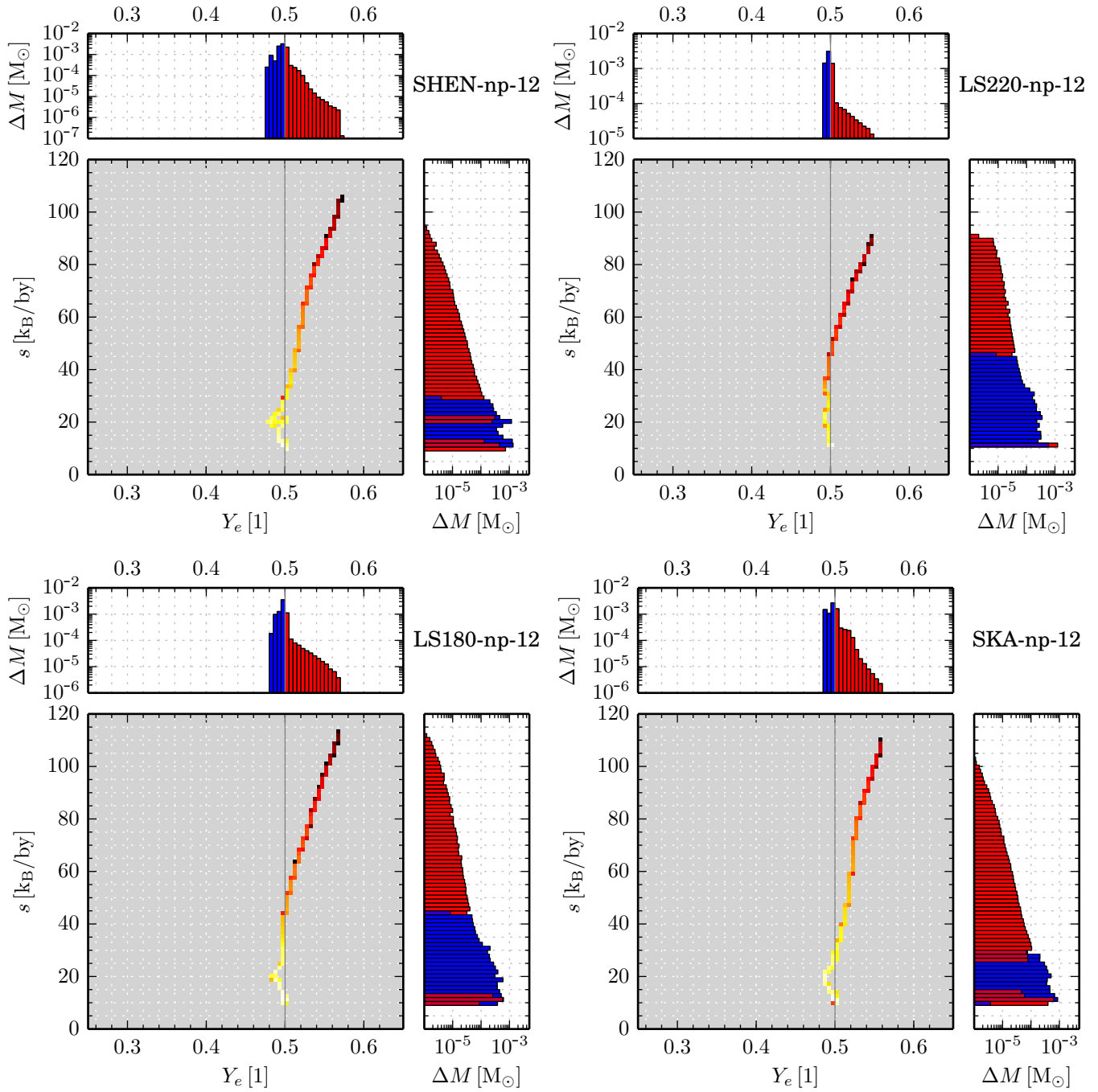


**Figure 3.46:** The upper sub-panel of each four plots shows a histogram of the ejected mass by  $Y_e$ , with a bin width of 0.005. The right sub-panel shows a histogram of the ejected mass by entropy  $s$ , with a bin width of  $1.5 k_B$ . Matter with  $Y_e < 0.5$  (blue) and  $> 0.5$  (red) is summed individually and shown as two separate histograms there. The histograms were created by recording all matter streaming through a radius of 250 km. The central panels show the colour coded amount of matter as a function of both electron fraction and entropy at the same time.



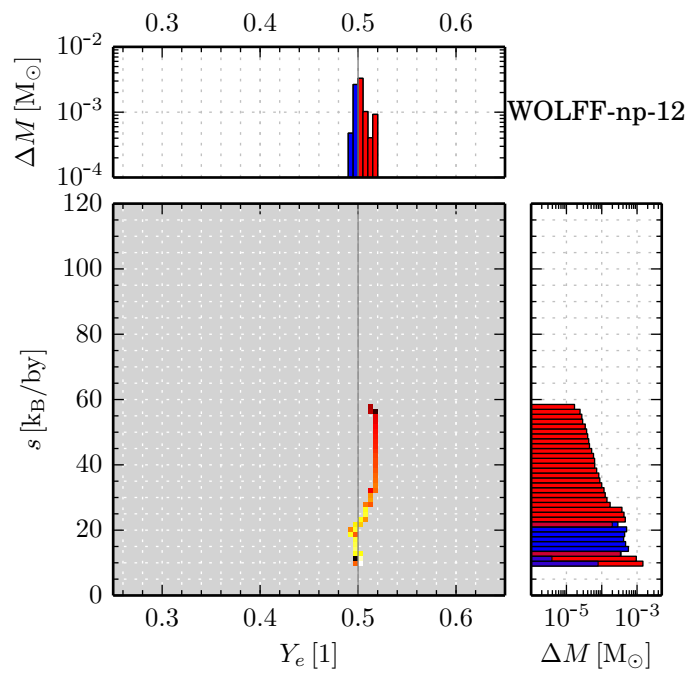


**Figure 3.47:** As Figure 3.46 but for the WOLFF EoS.



### 3.6.3 Convection

In Figures 3.48 and 3.49 we show the comparison with the physically next best model, the models where we added a convection treatment. For this purpose we only show the time range where we also have data for those models. We see that the entropy of the convection models is very similar to the non-convective models. Also the expansion time scales of the convection models are fairly similar to the non-convective models, as is the mass outflow rate. In the case of  $Y_e$ , we see that for the models with convection (both Newtonian and relativistic criterion) we find no more neutron rich early ejecta. In fact, there the wind is always proton rich. While the  $Y_e$  of the convection models has at the beginning higher values than the non-convective models, they tend to lower values at late times. H\"udepohl (2014) also found that all his models with convection and corrected nucleon opacities (marked with co) were proton rich, probably due to the inclusion of weak magnetism (which we also include). The models with the LS220, LS180 and SKA EoS show proton rich early ejecta. This is in agreement with the luminosities. Before  $\sim 250$  ms the luminosity of the  $\nu_e$  are higher for the convection models, while the luminosities of the  $\bar{\nu}_e$  are lower, than in the non-convective case. This leads to a higher  $Y_e$ . It seems that the convection affects the neutrinospheres of the  $\nu_e$  and  $\bar{\nu}_e$  differently.

### 3.6.4 Network

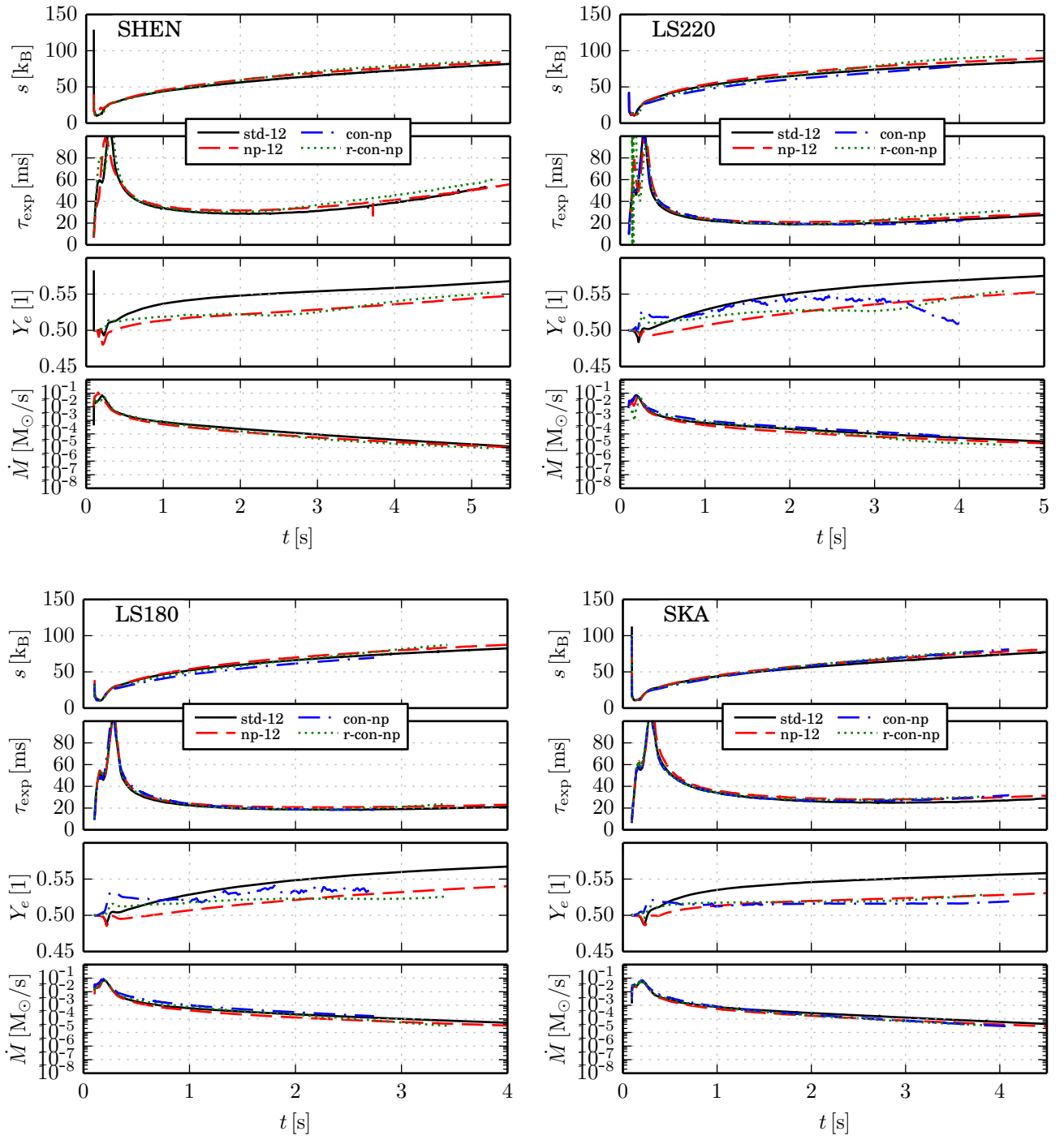
In Figure 3.50 we show a comparison of the r-process relevant quantities for models done with the full nuclear reaction network and models with the same physics but and approximate burning treatment. We see that the quantities beside the expansion timescale are fairly similar for all shown models and EoS. H\"udepohl (2009); H\"udepohl et al. (2010) slightly overestimated their calculated  $Y_e$  by ignoring the so called  $\alpha$ -effect: In the wind outflow equal parts of free proton and neutrons form  $\alpha$ -particles, which have a very low neutrino interaction cross-section and remain stable (or form even heavier elements). This leaves only the remaining particle kind, either neutrons or protons. Meanwhile the neutrinos change a part of those remaining particles in  $\beta$ -reactions, ultimately driving the  $Y_e$  towards 0.5 from any initial value (Fuller and Meyer, 1995). To model that, we lowered for the models with the approximate burning treatment the NSE temperature threshold to  $0.4 \text{ MeV}/k_B$ , in order to fully account for  $\alpha$ -particle formation.

In Figure 3.51 we see profiles of the mass fractions and  $Y_e$  at one second. We see that for the model without the full network we can not fully model the formation of intermediate mass elements. But the  $\alpha$ -effect is well captured, as we also see in Figure 3.50, the amount of free nucleons (protons here) is very similar.

### 3.6.5 EoS

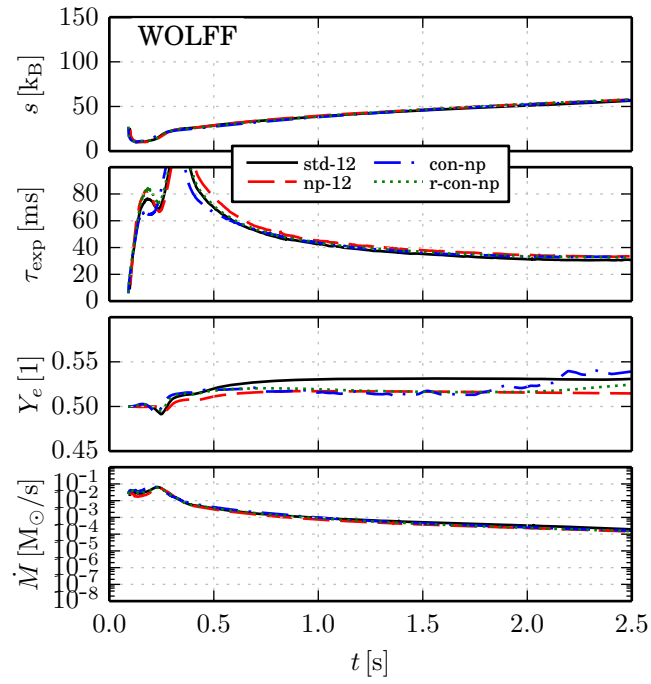
In Figure 3.52 we show a comparison of the different EoS for our best physics models with the Newtonian convection treatment and with the relativistic convection treatment which both include the corrected nucleon opacities, as mentioned before.





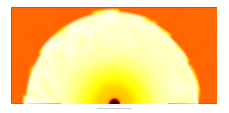
**Figure 3.48:** As Figure 3.43 but a comparison between the models with and without convection, using both the Newtonian and the relativistic convection criterion.





**Figure 3.49:** Same as Figure 3.48 but for the WOLFF EoS.

We see that the  $Y_c$  of the models with the relativistic convection treatment varies less than that of the Newtonian convection criterion. Also, here the expansion timescale and the entropy of the convection models show a strong dependence on the EoS.



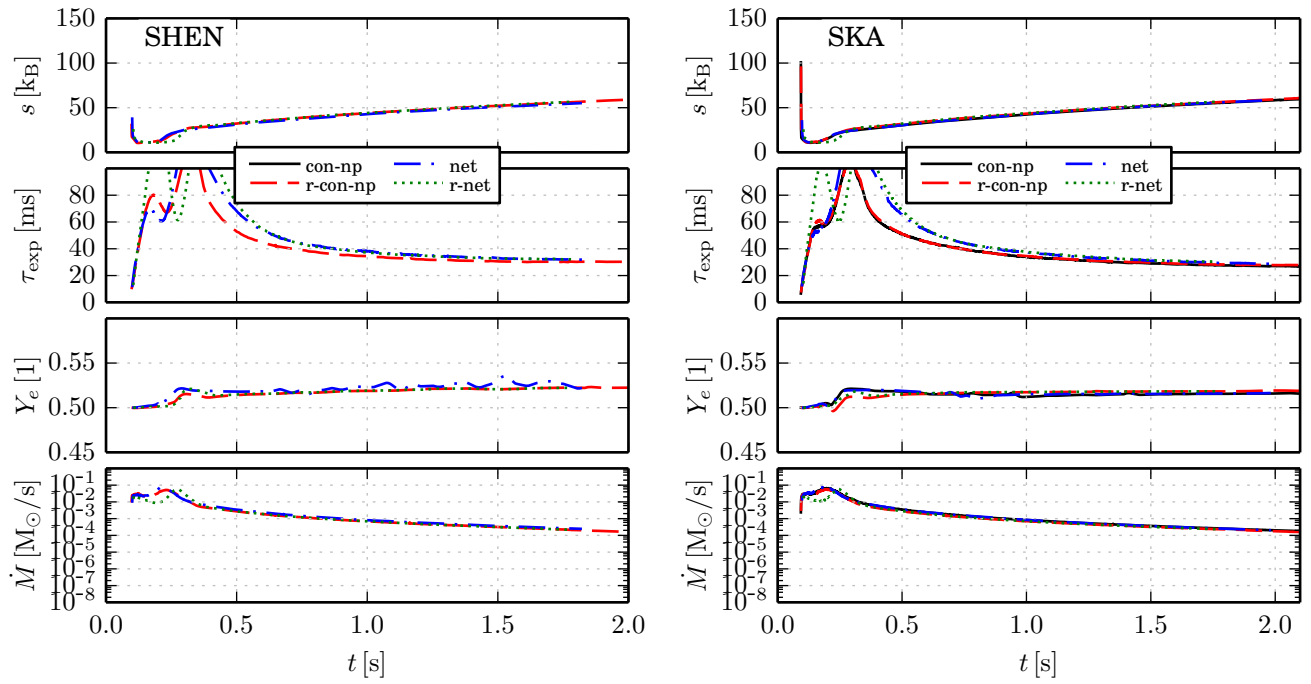


**Figure 3.50:** As Figure 3.43, here we compare for the SHEN and SKA EoS the models done with a full nuclear network and with approximate burning treatment, for the version with Newtonian and relativistic convection criterion. Note that we show only the first 2 s here.



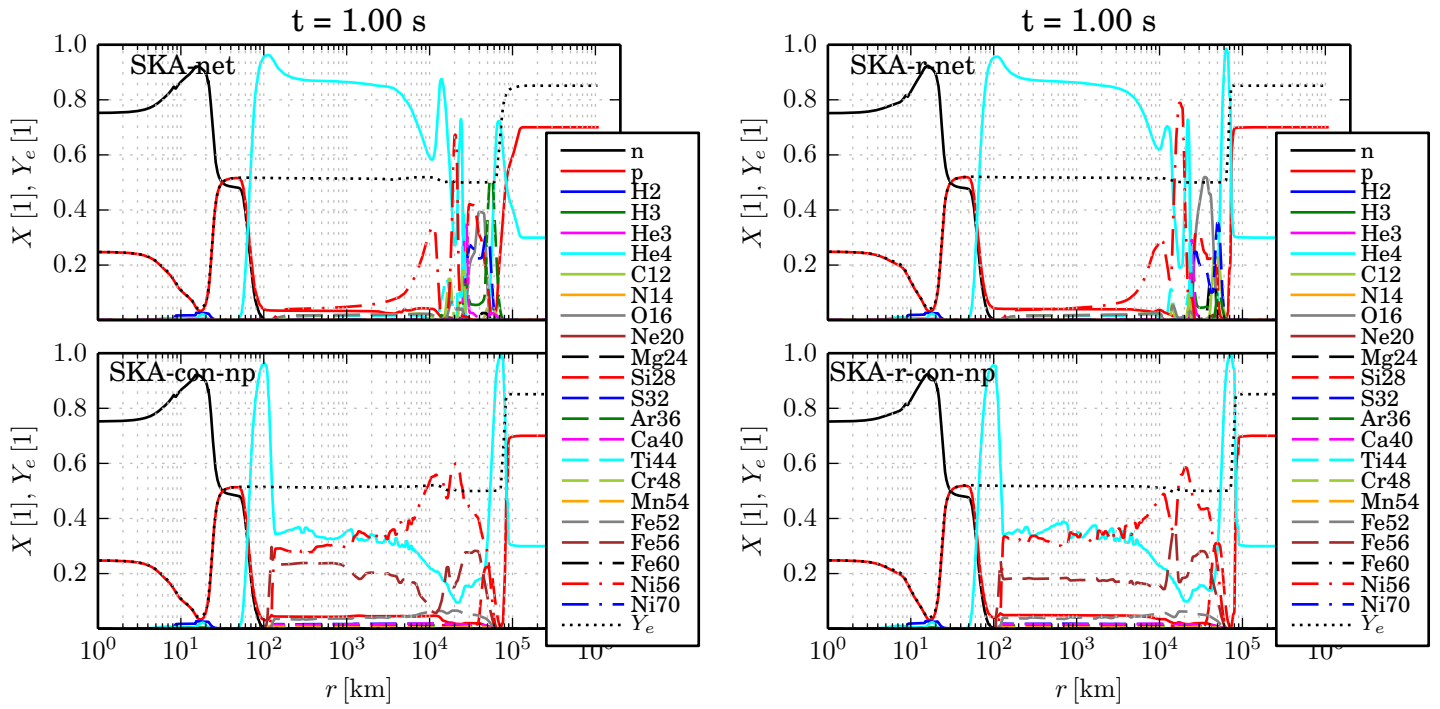


**Figure 3.51:** Profiles of the mass fraction and  $Y_e$  of the models with and without a full nuclear reaction network at 1 s post-bounce. On the left hand side we show the model which also have Newtonian convection treatment and on the right hand side models with relativistic convection treatment.



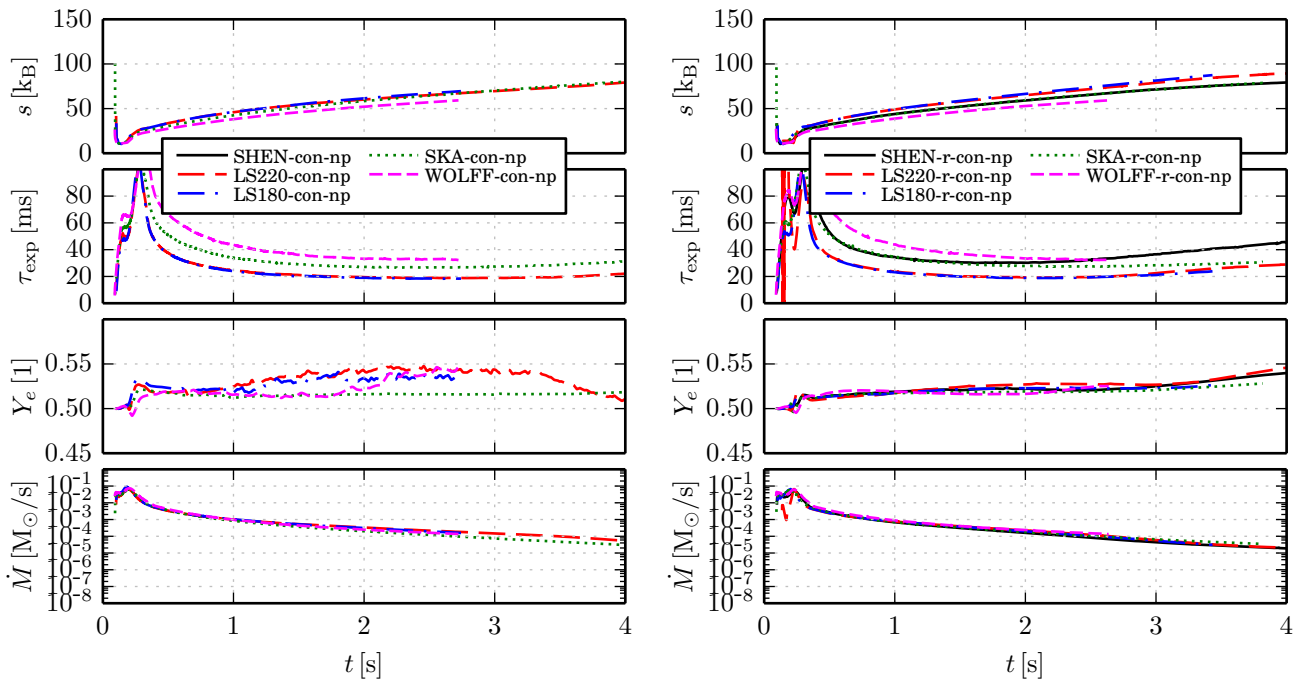


**Figure 3.52:** A comparison of r-process relevant quantities in the wind for our best physics models with Newtonian and relativistic convection treatment for all five EoS.



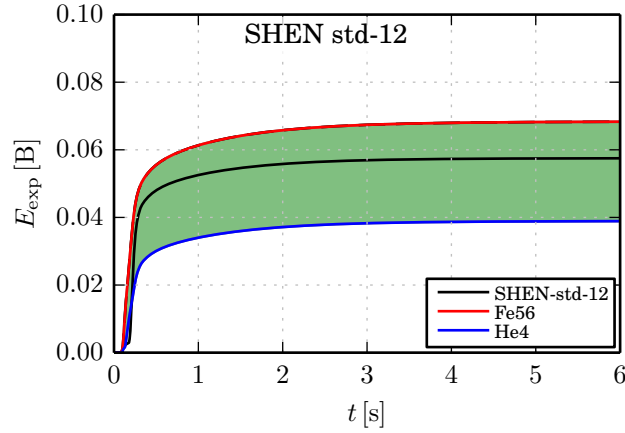


**Figure 3.53:** The upper, red line indicates the explosion energy when we assume that all ejected matter is burned to Fe56. The lower, blue line indicates the explosion energy when we assume that everything ends up as He4. These two lines can be seen as the maximal and minimal reachable explosion energies. The line in the middle shows the diagnostic explosion energy with the calculated mass fractions from the simulation.

### 3.7 Explosion Energy

From a supernova remnant observation an estimate of the explosion can be drawn. The ONeMg progenitor was therefore suggested as a progenitor for the supernova 1054 that caused the Crab Nebula, as a weak explosion could explain the observed properties (Nomoto et al., 1982). The explosion energy would be low as the progenitor has only a thin, loosely bound outer shell. We define a diagnostic "explosion energy" as the sum of the binding energy of all ejected matter. The binding energy is defined as the sum of the thermal and degeneracy energy, i.e. the specific internal energy  $\epsilon$ , the kinetic energy and the (negative) gravitational energy  $\Phi$ ,

$$E_{\text{bin}} = \rho \cdot (\epsilon + E_{\text{kin}} + \Phi), \quad (3.8)$$

cf. Equation (27) and (28) in Buras et al. (2006) and Equation (3) in Müller et al. (2012a). For the relativistic case we use a pseudo-Newtonian potential  $\Phi = (\alpha - 1) \cdot c^2$ , where  $\alpha$  is the lapse function, see Eq.(2.18) and for the specific internal energy we use the internal energy directly from the EoS. The explosion energy is then obtained by

$$E_{\text{exp}} = \int_{E_{\text{bin}} > 0} E_{\text{bin}} dV, \quad (3.9)$$

where  $dV$  is the volume element for the curved space time metric, cf. Equation (29) in Buras et al. (2006) and Equation (4) in Müller et al. (2012a).

Figure 3.53 shows the explosion energy for the std-12 model with the SHEN EoS. We see that around 0.1 s the explosion energy rises steeply up to around 0.3 s. This is obtained when the matter which is heated by neutrinos before the onset of the



explosion has gained enough energy to overcome the gravitational binding energy. From 0.3s on the explosion energy flattens and rises slower. Here, the additional energy comes from the neutrino driven wind, see Janka et al. (2008). As the ejected matter will still undergo nuclear reactions and thereby release energy, we show two extreme cases in Figure 3.53. The red line shows the explosion energy when we assume that all the matter is burned to Fe56. During this process energy gets released, resulting in higher explosion energy. Conversely, if we assume that all ejected matter is split up into He4, we get the lower blue line for the explosion energy. The green shaded area indicates therefore the region where the values of the explosion energy could be. The black line in Figure 3.53 is the explosion energy which we get by using the mass fraction as calculated by the code. We will use this particular explosion energy for the rest of our Figures, the extreme values can be interpreted as a very cautious error estimate.

The behaviour of the other models and EoSs is very similar. In Tables 3.11 and 3.12 we give the values of the other models of the three explosion energies shown in Figure 3.53.

### 3.7.1 GR vs. Post-Newton

In Figure 3.54 we show the comparison of our relativistic models with the post-Newtonian models, for the three different EoS. We see that for the SHEN EoS model the behaviour of the explosion energy is different than for the other two EoS models. First of all there is a notable difference between the model with 12 energy bins and the one with 21 energy bins. The 21 energy bin model has a higher explosion energy than the 12 energy bin one. Both models have a higher explosion energy than the post-Newtonian model, for the SHEN EoS. We do not see this behaviour for the LS180 and SKA EoS models, where the order of the explosion energies of the different models is the other way round. For the LS180 and SKA EoS models the explosion energies of the 12 and 21 energy bin models are quite similar. Both relativistic models have a lower explosion energy than the post-Newtonian models.

The main difference between the models is the gradient of the steep rise at the onset of the explosion energy. We know that the steep rise comes from the matter which is heated by the neutrinos. The heating rate is given by Janka (2001) in Equation (28),

$$Q_{\nu}^{+} \propto \langle \varepsilon_{\nu e}^2 \rangle L_{\nu e}. \quad (3.10)$$

With this we find that the matter from the 21 energy bin model of the SHEN EoS is heated up to 20%, more than the matter of the 12 energy bin model, during the first 70 ms. This is also the reason why more mass is ejected for the std-21 model, as we see in Table 3.11. We see that for the LS180 and SKA EoS models the ejected mass of the std-21 and std-12 models are relatively similar, as is their explosion energy.

Comparing the GR model with 21 energy bins and the post-Newtonian models we observe again that the matter of the std-21 model of the SHEN EoS was heated



**Table 3.11:** Interesting properties for the explosion energy at the end of each simulation ( $t_{\text{end}}$ ). With  $t_{\text{expl}}$  we denote the time when the explosion energy is 0.001 B,  $t_{\text{shock}}$  the time when the shock reaches 500 km,  $M_{\text{ej}}$  is the total ejected mass,  $E_{\text{expl}}$  the diagnostic explosion energy,  $E_{\text{expl, He}}$  the explosion energy if we assume that all ejected matter is He4, and  $E_{\text{expl, Fe}}$  is the explosion energy if we assume that all the matter is burned to Fe56.

Model	LS180						
	$t_{\text{end}}$ [s]	$t_{\text{expl}}$ [s]	$t_{\text{shock}}$ [s]	$M_{\text{ej}}$ [ $10^{-3}M_{\odot}$ ]	$E_{\text{expl, He}}$ [B]	$E_{\text{expl}}$ [B]	$E_{\text{expl, Fe}}$ [B]
con-np-1D	2.742	0.103	0.104	11.5	0.064	0.086	0.101
np-12-1D	10.100	0.105	0.108	0.1	0.039	0.056	0.064
p-newt-1D	15.998	0.088	0.088	11.5	0.073	0.069	0.110
r-con-np-1D	3.432	0.103	0.106	8.5	0.044	0.061	0.071
std-12-1D	11.041	0.105	0.108	8.6	0.047	0.064	0.074
std-21-1D	4.914	0.103	0.104	8.8	0.046	0.063	0.073

Model	LS220						
	$t_{\text{end}}$ [s]	$t_{\text{expl}}$ [s]	$t_{\text{shock}}$ [s]	$M_{\text{ej}}$ [ $10^{-3}M_{\odot}$ ]	$E_{\text{expl, He}}$ [B]	$E_{\text{expl}}$ [B]	$E_{\text{expl, Fe}}$ [B]
con-np-1D	4.042	0.101	0.104	10.4	0.057	0.077	0.091
np-12-1D	5.179	0.108	0.123	6.7	0.032	0.046	0.053
std-12-1D	8.008	0.105	0.105	8.9	0.047	0.065	0.075
std-21-1D	4.686	0.103	0.106	8.8	0.046	0.063	0.074

Model	SHEN						
	$t_{\text{end}}$ [s]	$t_{\text{expl}}$ [s]	$t_{\text{shock}}$ [s]	$M_{\text{ej}}$ [ $10^{-3}M_{\odot}$ ]	$E_{\text{expl, He}}$ [B]	$E_{\text{expl}}$ [B]	$E_{\text{expl, Fe}}$ [B]
net-1D	1.822	0.100	0.106	10.1	0.043	0.052	0.075
np-12-1D	9.447	0.098	0.097	10.9	0.052	0.076	0.086
p-newt-1D	8.874	0.085	0.084	11.0	0.060	0.045	0.095
r-con-np-1D	5.286	0.098	0.099	8.6	0.032	0.049	0.059
r-net-1D	1.780	0.104	0.112	7.1	0.028	0.035	0.050
std-12-1D	6.231	0.099	0.102	9.3	0.039	0.057	0.068
std-21-1D	5.572	0.098	0.100	10.2	0.046	0.067	0.078

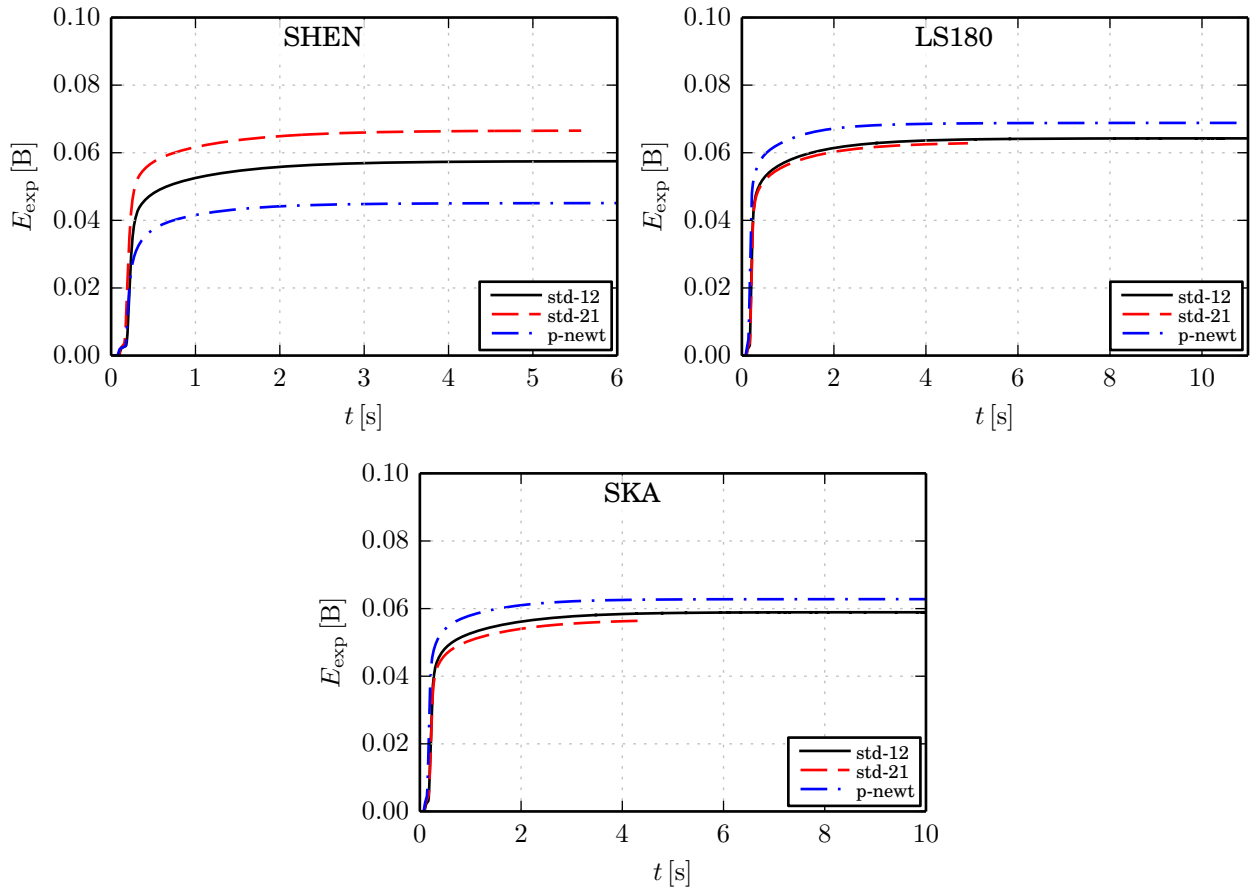
  

Model	SKA						
	$t_{\text{end}}$ [s]	$t_{\text{expl}}$ [s]	$t_{\text{shock}}$ [s]	$M_{\text{ej}}$ [ $10^{-3}M_{\odot}$ ]	$E_{\text{expl, He}}$ [B]	$E_{\text{expl}}$ [B]	$E_{\text{expl, Fe}}$ [B]
con-np-1D	4.099	0.093	0.095	10.6	0.045	0.067	0.080
net-1D	1.983	0.098	0.106	10.9	0.049	0.058	0.084
np-12-1D	9.399	0.096	0.099	8.2	0.031	0.049	0.057
p-newt-1D	14.665	0.082	0.082	11.8	0.064	0.063	0.101
r-con-np-1D	3.818	0.094	0.097	9.2	0.037	0.056	0.066
r-net-1D	1.762	0.103	0.111	7.3	0.029	0.037	0.052
std-12-1D	10.657	0.095	0.098	0.1	0.040	0.059	0.070
std-21-1D	4.330	0.094	0.095	9.3	0.038	0.056	0.068

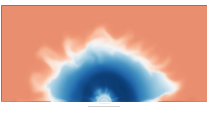


**Table 3.12:** As Table 3.11 but for the model with the WOLFF EoS.

Model	$t_{\text{end}}$ [s]	$t_{\text{expl}}$ [s]	$t_{\text{shock}}$ [s]	$M_{\text{ej}}$ [ $10^{-3}M_{\odot}$ ]	$E_{\text{expl, He}}$ [B]	$E_{\text{expl}}$ [B]	$E_{\text{expl, Fe}}$ [B]
con-np-1D	2.723	0.091	0.012	13.1	0.046	0.074	0.088
np-12-1D	2.518	0.100	0.104	9.4	0.029	0.049	0.058
r-con-np-1D	2.638	0.091	0.091	11.5	0.036	0.060	0.073
std-12-1D	2.489	0.098	0.100	11.2	0.038	0.061	0.073
std-21-1D	2.457	0.092	0.092	13.4	0.052	0.081	0.094



**Figure 3.54:** Time evolution of the diagnostic explosion energy, for the GR models and the post-Newtonian models, for the three different EoS for which we were provided with a post-Newtonian model.



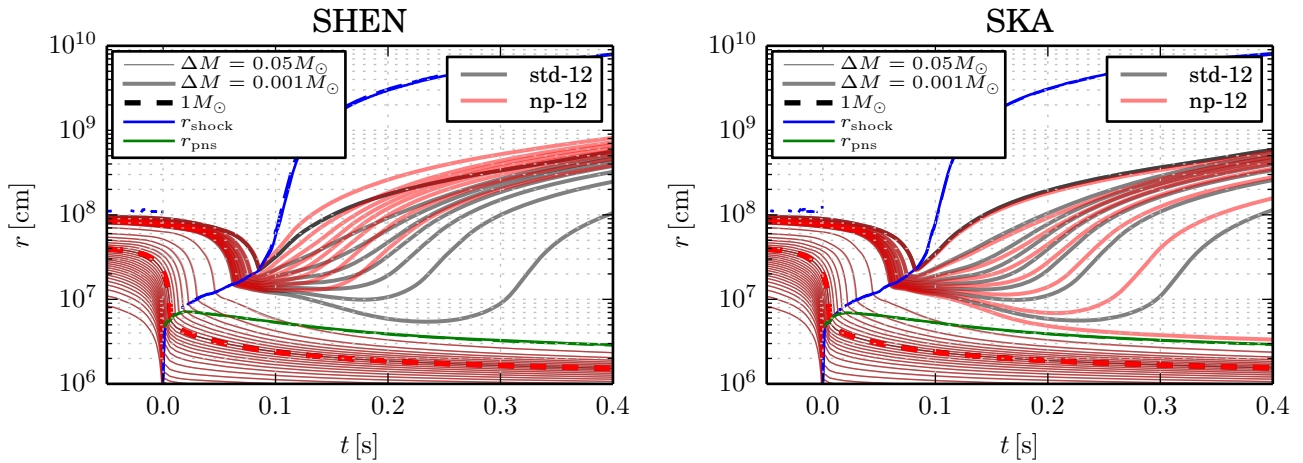


**Figure 3.55:** Time evolution of mass shells for the models with and without corrected nucleon potentials. The blue line indicates the shock radius, solid for the model without nucleon potentials and dashed for the model with nucleon potentials. The green line shows the proto neutron star radius.

more and over a longer time than the p-newt model. This leads to the higher explosion energy of the std-21 model. The opposite is the case for the models with the LS180 and the SKA EoS models.

Kitaura et al. (2006) and Janka et al. (2008) published results of the explosion energy with the ONeMg progenitor. They also assumed the positive binding energy to be the explosion energy. They used a Newtonian code with an effective relativistic potential and published results with the LS180 as high-density EoS. As an extrapolation of the explosion energy, they assume for their 1D model a value of 0.15 B. Judging from the curve of the explosion energy, we see that the behaviour is similar to our case when we assume that the whole matter is burned to Fe56. Also, their plateau part of the explosion energy rises slightly steeper than ours, indicating a stronger wind in their models, which results in the higher end value. We can assume that in our case the explosion energy of the post-Newtonian model with the LS180 EoS has reached its saturation and is 0.11 B, if we assume everything is burned to Fe56, see Table 3.11.

### 3.7.2 Nucleon potentials

Our next step is to compare the models with and without corrected neutrino nucleon opacities. For this, one has to compare from Figure 3.56 always the solid black line (std-12) with the blue dash-dotted line (np-12). We see, in the upper right panel of Figure 3.56, that for the SHEN EoS the model with corrected nucleon opacities has a higher explosion energy than the std-12 model. In fact it even has the highest explosion energy of all SHEN EoS models. For all the other four EoS



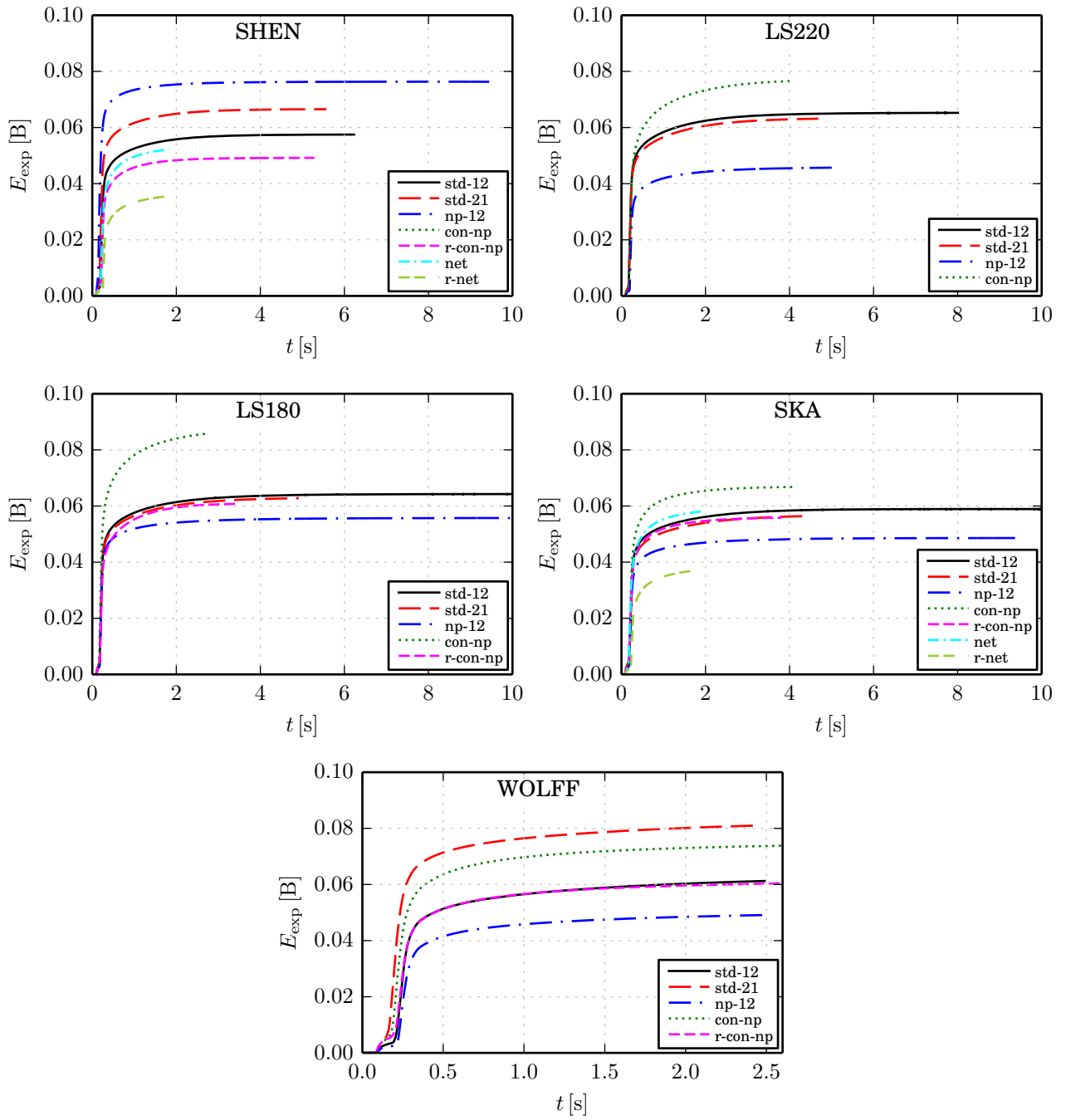


**Figure 3.56:** The diagnostic explosion energy for all models with all the five different EoS.

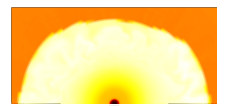


the np-12 model is always below the std-12 model. The late saturation of the explosion energy is for the std-12 and np-12 models similar for all EoSs. Also here the main difference is the height of the initial, steep rise during the explosion. In Figure 3.55 we compare the behaviour of the model with and without corrected neutrino nucleon opacities for the SHEN and, representative for the other four EoS, the SKA EoS. We see, with the help of selected mass shells, that in the SHEN EoS case (left panel of Figure 3.55) the np-12 and the std-12 model behave very similar up to the time of bounce. After that the corrected model explodes earlier than the model without the corrected opacities, which is indicated by the red coloured mass shells rising earlier than the grey ones. This seems to be the cause of the higher explosion energy, even though the matter of the std-12 model gets heated over a longer period. In the case of the SKA EoS (right panel of Figure 3.55) we do not see such a drastic difference between the explosion time of the models with and without the inclusion of the nucleon potentials. We see that here the std-12 model explodes before the model with corrected neutrino nucleon opacities. Additionally, we see that both models with the SKA EoS explode later than the np-12 model with the SHEN EoS, see also Figure 3.58.

### 3.7.3 Convection

In Figure 3.56 we also see the comparison between the models with (con-np/r-con-np) and without convection (np-12). Again we differentiate between the Newtonian convection treatment (green dotted line) and the relativistic convection treatment (magenta short dashed line). We should keep in mind that the convective models were simulated with 21 energy bins and the non-convective models with 12 energy bins. At least for the models with the SHEN EoS this has some impact, as we saw in Section 3.7.1. We see that the Newtonian convection models have the highest explosion energies, except for the SHEN and WOLFF EoS. In case of the models with convection treatment, the proto neutron star loses its energy faster than in the non-convective treatment. More energy is released in the first second, making the explosion energy higher than in the non-convective case. In the case of the SHEN EoS our convection model with the Newtonian criterion could not be simulated far enough to calculate an explosion energy. For the WOLFF EoS, the 21 energy bin model without convection and without corrected neutrino nucleon opacities (std-21) has the highest explosion energy, followed by the model with Newtonian convection treatment (con-np). Also here the std-21 model explodes earlier than the con-np model.

In case of the relativistic convection models we see that for the LS180, SKA, and WOLFF EoS the explosion energies are higher than the non-convective models (np-12). For the SHEN EoS, the relativistic convection model has a lower explosion energy than the non-convective model (np-12). We do not show the explosion energy of the r-con-np model with the LS220 EoS in the upper right panel of Figure 3.56, as this is one of the cases where the outer shell explodes during the collapse.



We find that the explosion energy of the relativistic convection model with the SKA EoS lies at early times between the models with 12 and 21 energy bins. After around 3s the explosion energy of the relativistic convection model becomes flat while the explosion energy of the 21 energy bin model rises above it. This suggest that the energy gained from the neutrino driven wind is different in both cases. For the WOLFF EoS the explosion energy of the relativistic convection model is nearly the same as for the model with 12 energy bins. At later time it starts to differ, from around 1.5s on, after which the explosion energy of the r-con-np model becomes lower than the std-12 model. Also here the energy gained from the neutrino driven wind seems to be different.

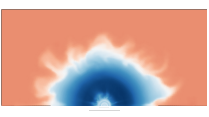
### 3.7.4 Network

The explosion energies from the model done with the burning network have not reached saturation. For the SHEN EoS, we can only compare the models with the relativistic convection treatment. We see that the explosion energy of the model with the network is lower then for the model without the network. This is also the case for the models with the SKA EoS. Here we can compare the models with Newtonian convection treatment. The explosion energy of the model with the network is below the model with out the network, as well.

Interesting is that even if we assume that all the matter gets burn to Fe56 the explosion energy, is lower for the model with the network than of those without, see Table 3.11. In the upper two panels of Figure 3.57 we compare the behaviour of the mass shells for the model with and without the network. On the left hand side we see that the models are very similar, whereas the models on the right hand side differ a lot. This might come from a different amount of nucleons in the heating region we therefore examine them in the lower two panels of Figure 3.57 at the time the explosion sets in. We do see a slightly different amount. Note that this is not necessarily a result of the network itself, but can also be due to the different NSE temperature threshold with and without the network, as indicated by the grey shaded areas.

### 3.7.5 EoS

We saw in the Sections above that there is a huge difference of the explosion energy between the EoS. In this Section we want to compare the explosion energy of the models with different EoS directly. It is always a hope that with the help of observations one could infer constraints on the EoS, as the explosion energy is a somewhat observable quantity. In Figure 3.58 we show the explosion energy of the different EoS. We see in the upper left panel the comparison of the models without convection and without corrected neutrino nucleon opacities with different EoS. In this case the explosion energies are quite similar to each other. The explosion energy of the LS220 EoS model, which has the highest explosion energy, is  $\sim 14\%$  higher than the one of the SHEN EoS model, which has the lowest energy. Kitaura et al.



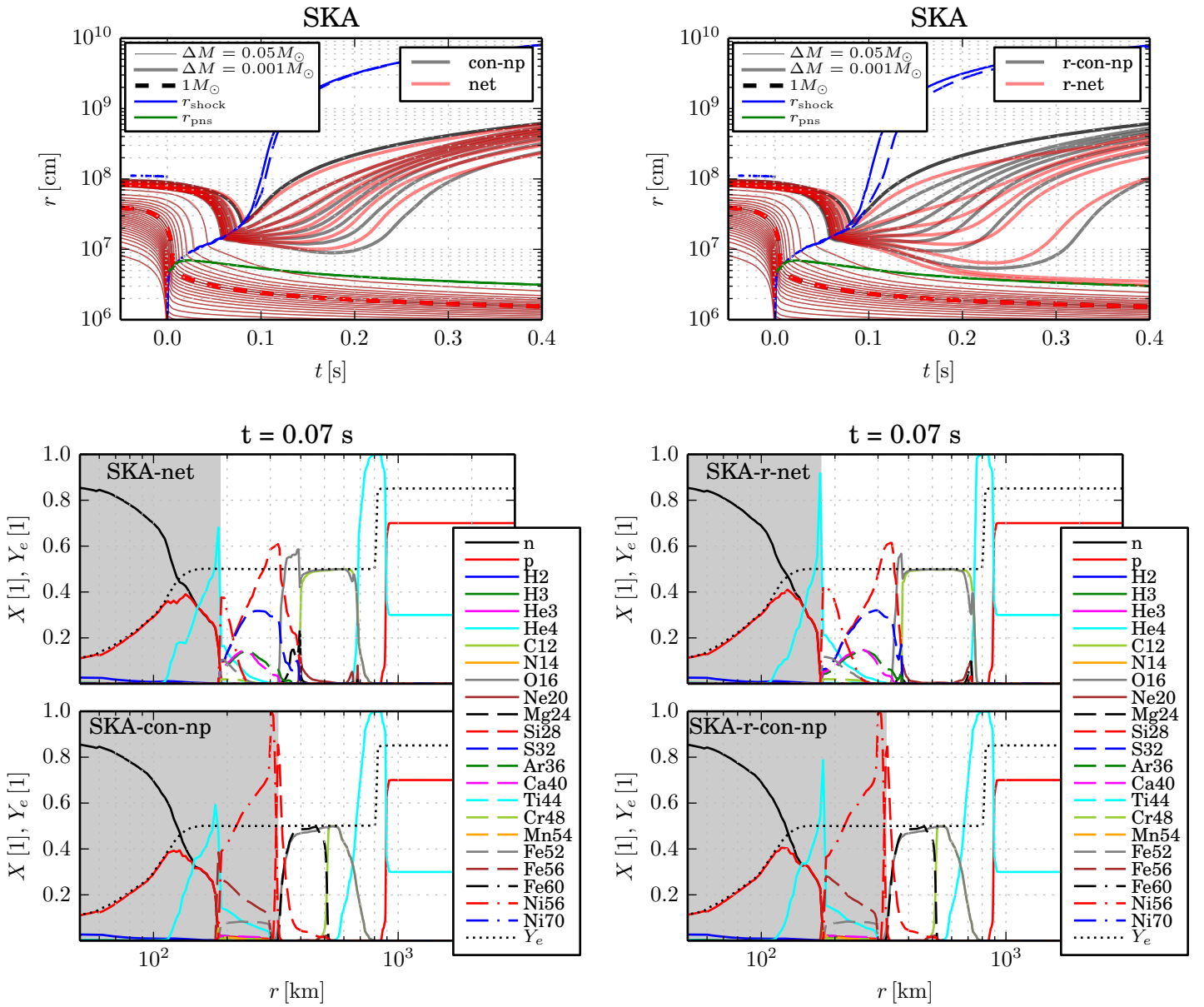


**Figure 3.57:** The upper two panels are the time evolution of mass shells for the models with and without network burning treatment. On the left hand side are the models with the Newtonian convection criterion, on the right hand side are the models with the relativistic convection criterion. The blue line indicates the shock radius, solid for the model without network and dashed for the model with network. The green line shoes the proto neutron star radius. The lower two panels are the comparing the mass fraction and  $Y_e$  of the SKA EoS models with and without the network. On the left hand side we show the models with the Newtonian convection criterion and the right hand side we show the model with the relativistic convection criterion. The gray shaded area indicates where NSE temperature is reached.



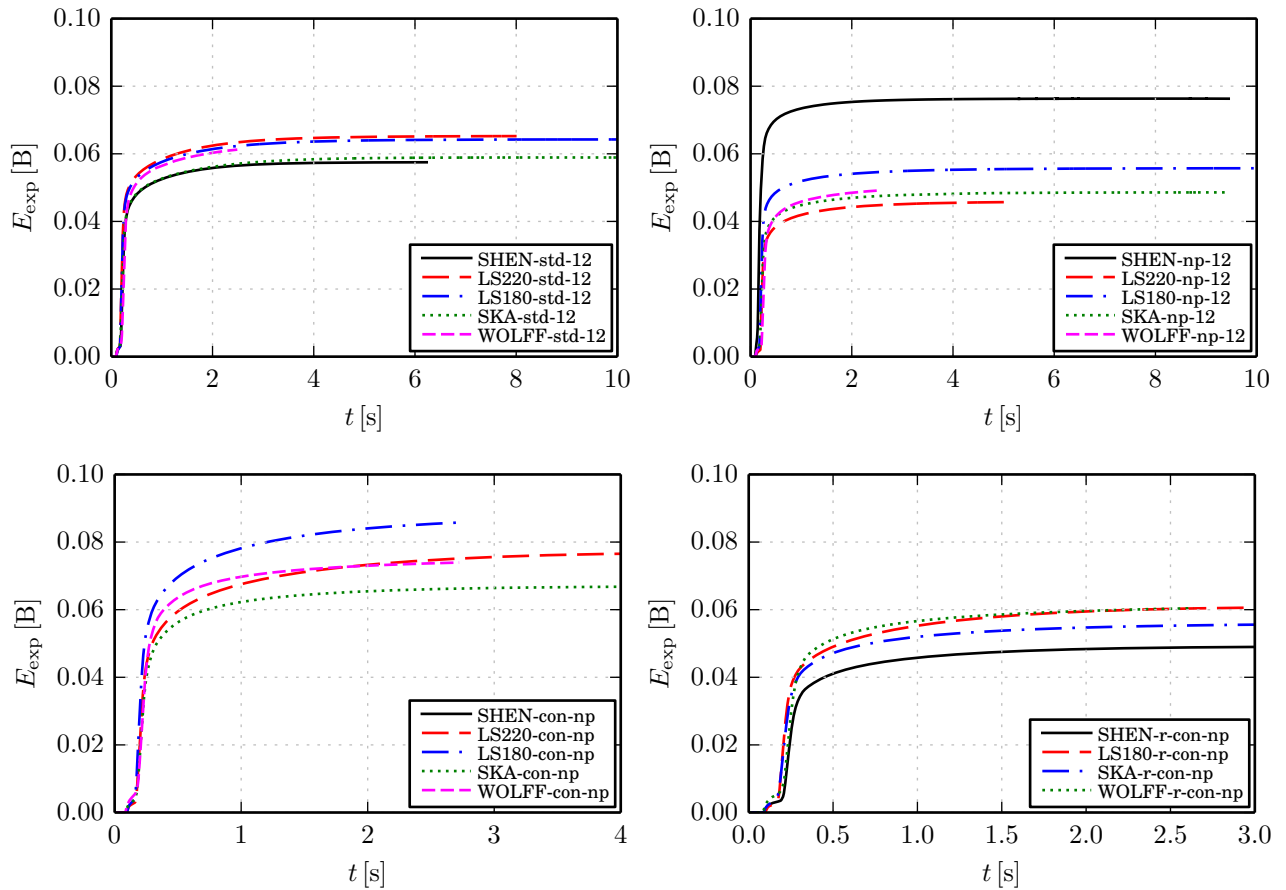


**Figure 3.58:** Comparing the diagnostic explosion energy between the models with different EoS. Note the different timescales.

(2006) compares the explosion energy of a LS180 EoS model (labeled L&S) with one done with the WOLFF EoS (labeled W&H). They find that the WOLFF EoS model has a lower explosion energy than the LS180 EoS model. By extrapolating they claim that the explosion energy of the LS180 EoS model will be  $\sim 50\%$  larger than the WOLFF EoS model. In our case the models with the WOLFF and LS180 EoS are fairly similar to each other, and the quantitative values we get for the explosion energy are below those calculated by Kitaura et al. (2006)

In the case of the models with the corrected neutrino nucleon opacities, upper left panel of Figure 3.58, we see a wider spread of the explosion energy. Here, the SHEN EoS model has the highest energy, followed by the LS180, WOLFF, SKA and LS220 EoS models. The relative difference of the explosion energy of the SHEN EoS model to the LS220 EoS model is  $\sim 65\%$ . Even compared to the LS180 EoS models with the second highest explosions energy the SHEN EoS model has a  $\sim 36\%$  higher explosion energy.



If we look at the difference in the explosion energies of our best physics models we see that they are again not that large, see the lower panels of Figure 3.58. In case of the Newtonian convection criterion, the LS180 EoS model has the highest explosion energy. This model has also the highest explosion energies of all our available models and is still rising. The lowest explosion energy here has the SKA EoS model and is around 21 % lower than the LS180 EoS model. In the case of the relativistic convection the WOLFF EoS model has the highest explosion energy for the first 1.5 s after which the LS180 gets higher. The SHEN EoS has the lowest explosion energy here and has an, around 20 %, lower explosion energy than the LS180 EoS model.

We have therefore to conclude that no sufficiently accurate predictions about explosion energies from our models can be made. Slight differences during and before the explosion seem to be able to alter the explosion energy to a very large extent.

We see that the relative differences between the EoS for the best physical models, meaning the convection models, are low. Therefore we assume that it would be very hard to be able to eliminate EoS with the help of the explosion energy.

Additionally the issue about the correct criterion for convection would have to be resolved. We would argue that the Newtonian criterion is appropriate. It reproduces our 2D results very nicely as we will show in the next chapter.

We can see in Table 3.11 that in most cases the explosion energy does coincide with the ejected mass. When the model explodes slightly earlier, more mass gets ejected. But when and how the models explodes seems to be very sensitive and we found that it depends on even minor numerical changes.





## 4 Axially Symmetric Simulations (2D)

Have no fear of perfection,  
you'll never reach it

---

*(Salvador Dali)*

In this Chapter we will discuss the results of our axially symmetric (2D) simulations. Multi dimensional simulations are considered to be necessary, despite the higher computational costs: Observations of SN1987A show that there is some indication for a non spherical explosion (Catchpole 2012, Sinnott et al. 2013). Also, 1D models typically do not explode. The non-spherical convective motions in the accretion layer seem to be necessary to boost the neutrino heating efficiency, for more massive progenitors.

In the literature, multi dimensional simulations are usually discussed mostly in regard to the feasibility to produce an explosion. In our case, the used progenitor even explodes in spherical symmetry, however it is still expected that the details of the explosion will be changed in a multi dimensional simulation.

The help of multidimensional effects was already suggested by Epstein (1979), and based on this simulated by Bethe (1990). One such multi dimensional effect is convection. We saw in Section 3.4.3 and 3.5.3 that 1D simulations, even with a mixing length treatment for the convective flows, can not reproduce the PNS convection of the 2D results completely. For typical, more massive progenitors it was found that the increase in luminosity by proto neutron star convection is not enough to trigger an explosion, see Dessart et al. (2006) and Burrows et al. (2007). Another multi dimensional effect is the neutrino-driven convection in the accretion layer between the proto neutron star and the shock radius. Like in boiling water, neutrino heated matter is rising from above the proto neutron star upwards near to the shock front. At the same time, cooler matter streams downwards, (Janka and Müller, 1996). This is also interesting in another aspect, recent 2D simulations have shown that electron-capture supernovae could be a possible source of (weak) r-process elements (Wanajo et al., 2011): In contrast to 1D simulations, in 2D the mushroom shaped convective bubbles (see their Figure 1) can be expanded fast enough to also eject matter with low  $Y_e$  (see their Figure 2), before neutrinos can change the  $Y_e$  to higher values.

Our 2D simulations are also done with a general relativistic treatment, as the expansion timescale is very important for the r-process freeze-out. The simulations are performed as a  $180^\circ$  setup (i.e. the whole sphere), with 128 as well as 140 and 280 angular zones, to test the angular resolution dependence of the lowest values of  $Y_e$  and their ejecta mass distribution. In contrast to simulations done with the



VERTEX code, we do not map a spherically symmetric calculation onto a 2D grid after collapse. We do, however, calculate the innermost 300 zones as a spherically symmetric core during collapse. This is justified, as the collapse should be almost perfectly spherically symmetric. After the collapse, we reduce this number to only the innermost 6 zones ( $\sim$  the innermost km), to avoid very small time steps, see Marek (2007).

In this chapter we will concentrate on the possibility of r-process elements from the early ejected matter, and the effects of proto neutron star cooling, as we performed the first long-time multi dimensional cooling simulations with the VERTEX-CoCoNuT code.

Unfortunately, due to pre-existing numerical problems in the CoCoNuT module of VERTEX only one 2D model could be simulated for an appreciable amount of time (2.2 s for the WOLFF 2D-128 model). Only very recently we succeeded to produce a number of additional models, which so far have only reached a very short simulated time. These models were also done with the corrected neutrino nucleon opacities, which were discussed in Section 2.5. In Table 2.4 we find a list of the model names used. The model WOLFF 2D-128 is the only 2D model which was simulated without the corrected nucleon potentials and with only 12 energy bins. The simulations are still ongoing and could possibly be explored more in the future. The model without the corrected nucleon potentials has run longest (2.2 s) and we will therefore have to concentrate much of the discussion on this model (WOLFF 2D-128).

## 4.1 Angular resolution

In the case of 2D simulations we have now another dimension to resolve, the angular direction. 2D simulations are computationally expensive and take a long time. For this reason most of our 2D simulation have not progressed as far as the 1D simulations. A full comparison can sadly thus not yet be done. The simulations we compare here were done with 140 angular bins on a  $180^\circ$  setup, which corresponds to an angular resolution of  $1.3^\circ$ , and with 280 angular bins and thus  $0.6^\circ$  angular resolution. In contrast to Marek (2007) we didn't change the radial grid for the simulation with the higher resolution, both were done with an initial grid of 1400 radial zones, with a periodical refinement as was done in 1D, see Section 3.3.2

In Figures 4.1 we show the comparison of the neutrino signal of those two versions. As the behaviour is quite similar we will discuss the angular resolution on the basis of the models with the SHEN EoS, as both models have progressed the farthest of the 2D models with different resolutions. The effect we can see up to the simulated time is that the  $L_{\nu_e}$  burst of the better resolved model is slightly higher than those of the less resolved one. After that, the luminosities of the model with the higher angular resolution are slightly below the lower angular resolution model, for all neutrino flavors. We compare in Figures 4.1 the angular averaged mean energies of the models with each other, see Eq. (3.5). The mean



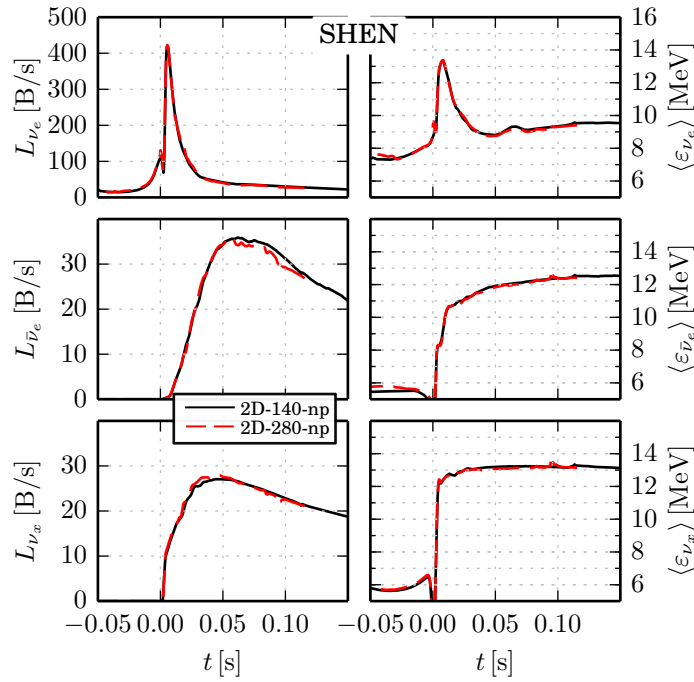


**Figure 4.1:** Compare neutrino signal for two SHEN EoS models with different angular resolution. The mean energy shown is averaged over the angels.

energies of the 2D-280-np model are slightly lower than for the 2D-140-np model. A similar behaviour was also seen by Marek (2007), he compared two models with an angular resolution of  $0.94^\circ$  and  $1.41^\circ$ . Marek (2007) claims that the observed difference were due to the different initial radial grid he used. This is not so in our case as we used the same initial grid for both models, and must therefore be an effect of the different angular resolution. In Figure 4.2 we show the spread of mean energies depending on the angle of the SHEN EoS model. We see that in the accretion phase the neutrino mean energies of the high resolution model are spread over a broader range than in the low resolution model.

We found that the angular resolution has an influence on the explosion. In Figure 4.3 we show mass shell plots color-coded with the velocity evolution. We see that both models are similar to around 0.05s. From there on we see that in the outer shells of the model with 280 angular zones collapse inwards normally. However, in the 140 zone model the outer shells stop collapsing, even expand into another shock front. There we obtain a nuclear burning explosion of the outer shells, before the actual neutrino driven explosion sets in, similar as in Figure 3.6. We also observe this for the lower angular resolution model with the SKA EoS. This is not the case for the WOLFF-2D-128 model, even though it has even less angular resolution. But one should keep in mind that this model was done without the corrected neutrino nucleon opacities. We have no comparative simulations



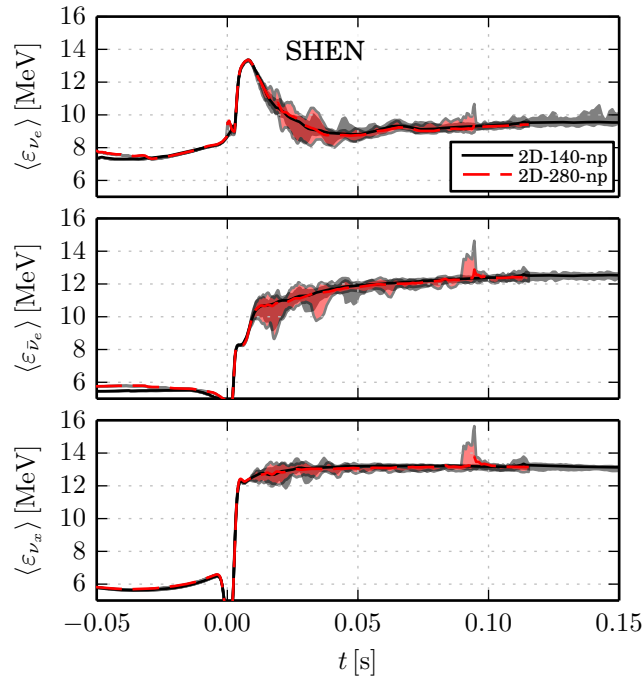


**Figure 4.2:** The angular spread of neutrino mean energies for the two SHEN EoS models with different angular resolution. The lines show the angle-averaged mean values.

done with the other EoS and the simulations with the corrected neutrino nucleon opacities and the other WOLFF EoS models are not that far developed. The model with the SHEN EoS and the high angular resolution does not show an explosion of the outer shell. On the other hand the actual explosion of the model with 280 angular zones sets in much faster than for the model with the 140 angular zones.

We also want to look at the influence of the angular resolution on the convective regions, as this is important for the ejecta composition. In Figure 4.4 we show therefore the lateral velocities as a measurement of the convection. We see that for the first 0.01 s the flow is relatively similar. But it already starts to differ at 0.02 s. On the right hand side the flow looks a bit more fine grained than on the left hand side, as would be expected from a model with higher angular resolution. At 0.05 s we can already see the explosive burning of the outer shell of the model with 140 angular zones. At the snapshot of 0.1 s the explosion of the model with 280 angular zone has set in and we see a high velocity slosh in the upper half of the panel.

The lateral velocity and therefore the convection is influenced by the premature outer shell explosion in the low resolution model. We also see the already indicated faster explosion of the high resolution model acting up here. Marek (2007) saw in his comparison also an inhomogeneous behaviour of the convectively unstable regions. But his simulations did not have the very early explosion as we see them



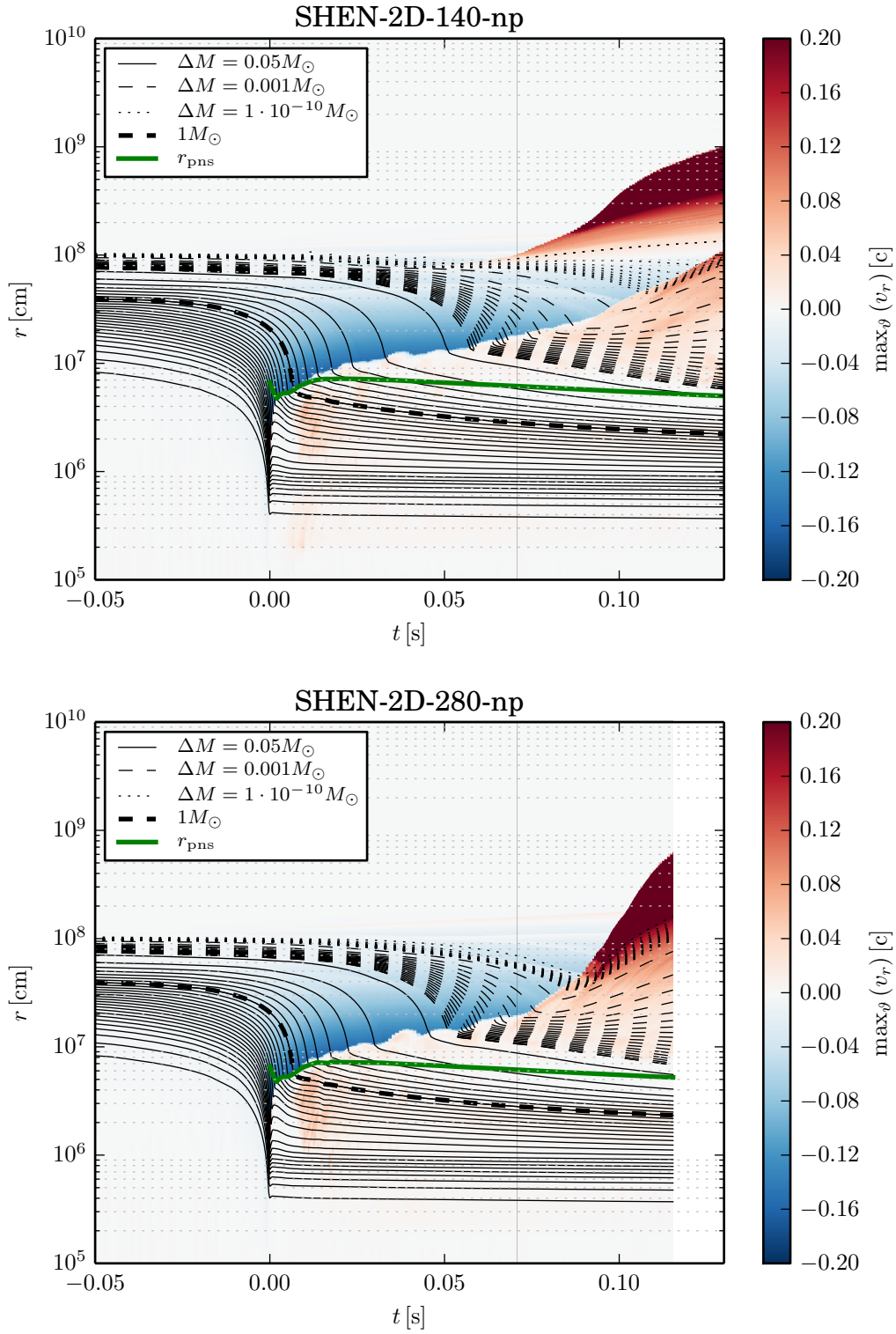


**Figure 4.3:** Evolution of mass shells over time for the SHEN EoS model with the lower angular resolution (upper panel) and the SHEN EoS model with the higher angular resolution (lower panel). Colour coded is the  $\vartheta$ -maximum of the radial velocity.



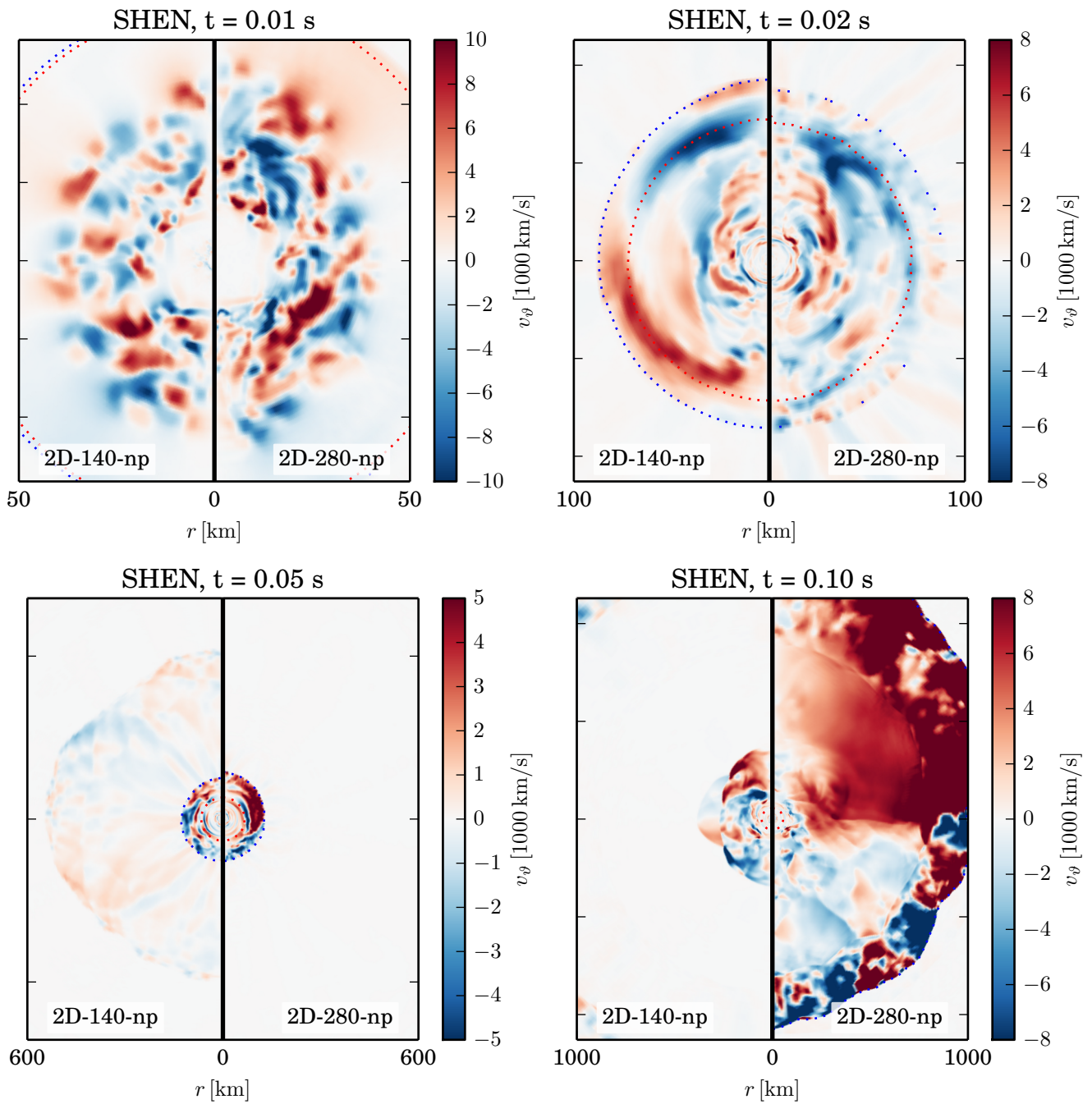
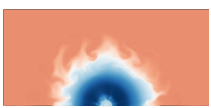


**Figure 4.4:** Comparing the lateral velocities ( $v_\phi$ ) of the SHEN models with different angular resolution, at different times. The model with lower angular resolution is always on the left hand side and the model with higher angular resolution on the right hand side. The dotted red line indicates the proto neutron star radius and the dotted blue line accretion the shock radius.



in our models.

It would be very interesting to see the long term effects of the different angular resolutions on the proto neutron star convection, but unfortunately our simulations have not progressed far enough yet.



**Table 4.1:** Time of the end of the simulation for all 2D models.

Model	LS180	LS220	SHEN	SKA	WOLFF
	$t$ [s]	$t$ [s]	$t$ [s]	$t$ [s]	$t$ [s]
128-2D	-/-	-/-	-/-	-/-	2.229 s
140-np-2D	0.079 s	0.006 s	0.337 s	0.157 s	0.011 s
280-np-2D	0.083 s	0.005 s	0.115 s	0.070 s	0.010 s

## 4.2 Neutrino signal for different EoS

In Figure 4.5 we show the neutrinos signal of all our 2D models in comparison with a suitable 1D model. We see that sadly most of our 2D simulations did not run very long yet, see also Table 4.1 where we show the post-bounce time at the end of the simulations. For the models with the LS220 EoS, which are the least progressed 2D simulations, we see a good agreement between the 2D models with the different angular resolution and the 1D model. This is expected as the collapse is spherically symmetric. The high angular resolution models of the WOLFF ran a little bit further and we see that for the  $\nu_e$  luminosity burst the model with the least angular resolution has a lower peak than the two other 2D models. Also we see some differences to the 1D models in the luminosities. For the models with the LS180 EoS we see that both 2D models are in a good agreement and have in comparison to the 1D model a lower luminosity for all flavours. The mean energies of the 2D models are a bit higher than the 1D model, with the exception of the maxima of the  $\nu_e$ . For the SKA EoS models the 2D models are also in a good agreement with each other but here the luminosities are higher than for the 1D model, while the mean energies are fairly similar.

The progenitor we use explodes usually around 70 ms. Therefore we are only interested in the models which were simulated longer than that. This leaves us with the models: WOLFF-2D-128, SHEN-2D-140-np, SHEN-2D-280-np, and SKA-2D-140-np. In Figure 4.6 we compare the neutrino signal and proto neutron star (PNS) radius of those models with each other. We see that the WOLFF EoS model has the lowest luminosity and mean energy. This was also observed for the 1D models. The SHEN and SKA EoS models show very similar luminosities and mean energies for the time shown. Also this is similar as in the 1D case. The model with the WOLFF EoS has the highest PNS radius. The different angular resolution models with the SHEN EoS have the same PNS radius with is a little bit higher than the PNS radius of the model with the SKA EoS. This behaviour is also seen for the 1D simulations.



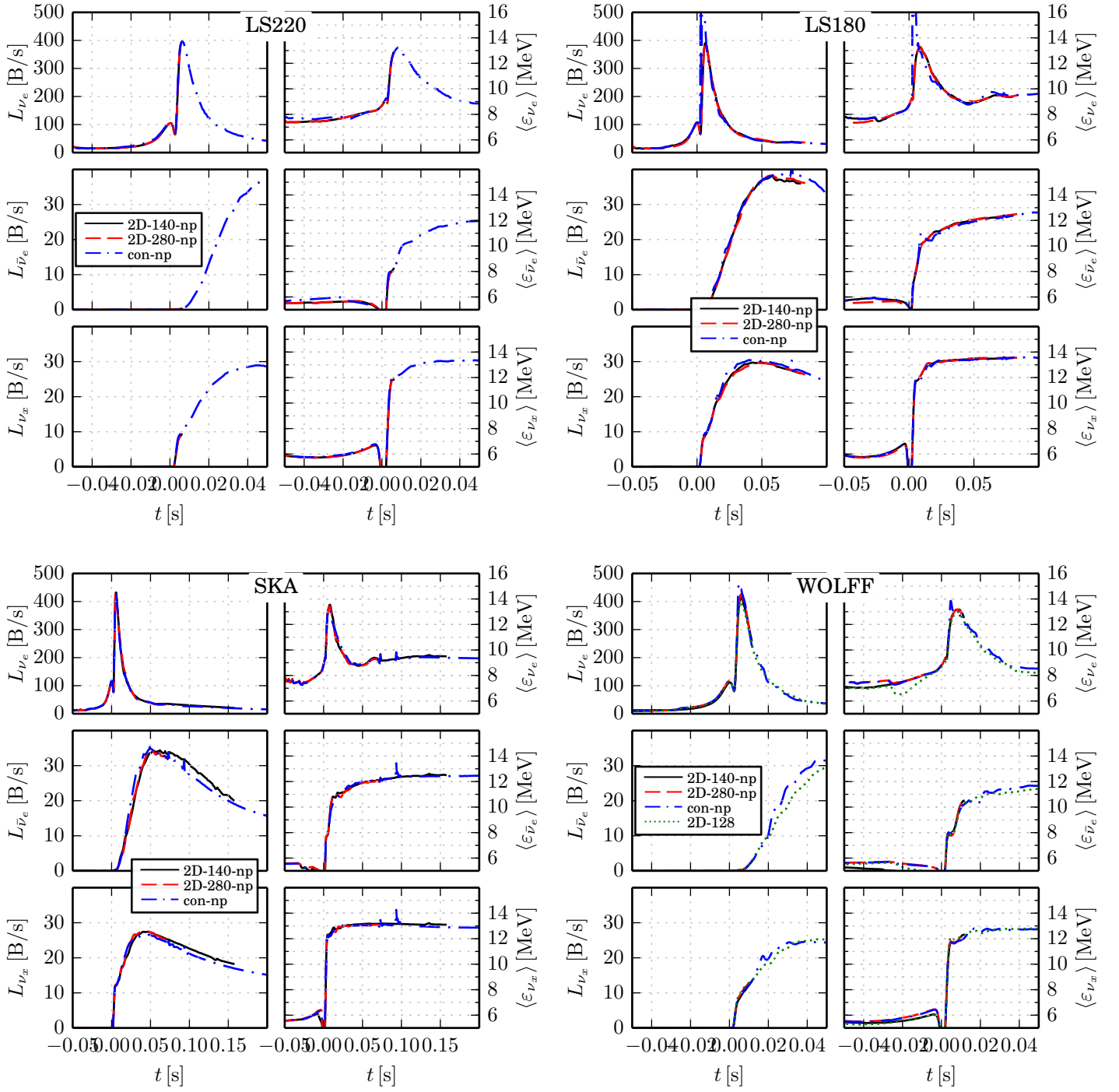


**Figure 4.5:** The neutrino signal of 2D models with different angular resolution and a comparable 1D model, for four different EoS.



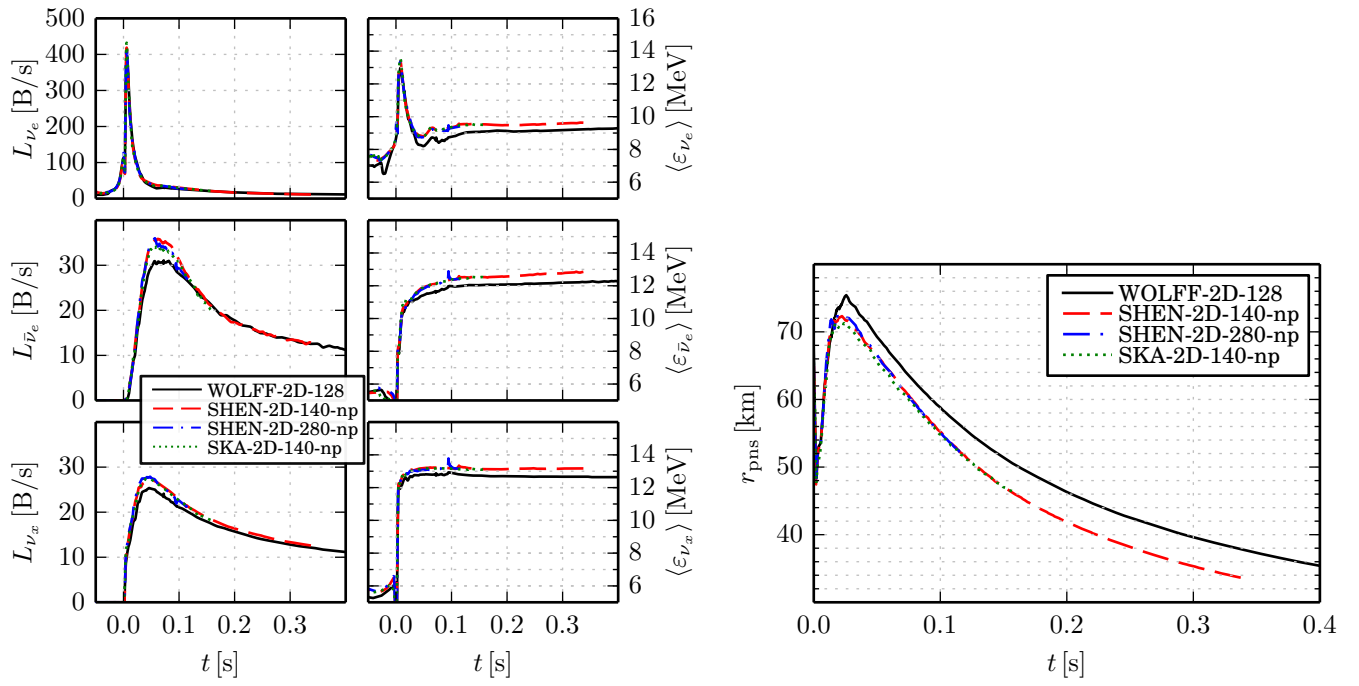


**Figure 4.6:** The neutrino signal, left hand side, and proto neutron star radius, right hand side, of the 2D models with different EoS, that could be simulated long enough for an explosion to occur. The mean energy shown is averaged over the angle.



### 4.3 Early Ejecta

Wanajo et al. (2011, 2013a) showed with 2D simulations from Janka et al. (2012) that early ejected matter from relativistic 2D simulations with the ONeMg progenitor could produce some r-process elements. In Figure 4.7 up to Figure 4.11 we show the entropy and  $Y_e$  of our 2D models for different EoS. Figures 4.7 and 4.8 show snapshots of the early ejecta for the WOLFF EoS models. In the snapshot at 0.05 s we see how the matter falls onto the proto neutron star (PNS) and gets slowed down by the accretion shock. With the help of streamlines we can see the convection inside and outside the PNS. One can see the beginning of Rayleigh-Taylor instabilities within the shock radius. Matter gets more neutron rich on its way down to the proto neutron star. However, the convection is able to lift some of this matter back up again and eject it in the following explosion. From 0.08 s to 0.5 s we can see how the shock moves further out. At 0.5 s we see the neutrino driven wind developing and the expansion of the mushroom shaped convective bubbles. For the  $Y_e$ , we see in the lower left corner neutron rich matter getting ejected, at the same time we see in the upper corner how the neutrino driven wind already starts to make the ejected matter proton rich. At 2.2 s we can see this proton rich wind even better.

In Figure 4.9 we see snapshots for the model with the SKA EoS. Comparing with the WOLFF EoS, we see that that the SKA EoS model explodes a bit later than the WOLFF EoS model. The lower left panel shows the last possible snapshot for the SKA model. We see that it shows a quadrupolar explosion. For the models with the SHEN EoS, Figure 4.10 and 4.11, we find for the model with the low angular resolution at 0.3 s a very neutron rich outflow in the north hemisphere. But this model is one where we saw that the outer shell showed explosive burning, cf. Figure 4.3. This outer shell explosion takes away infalling matter and thereby the matter from around the PNS might be able to flow out easier. This could influence the dynamics of the explosion and thereby the ejecta composition.

The explosions with an ONeMg progenitor are quite fast. Due to the steep density profile the explosion sets in quickly and with very high outflow velocities. Therefore, neutron rich pockets can be ejected outwards fast enough to avoid changes in composition by neutrinos.



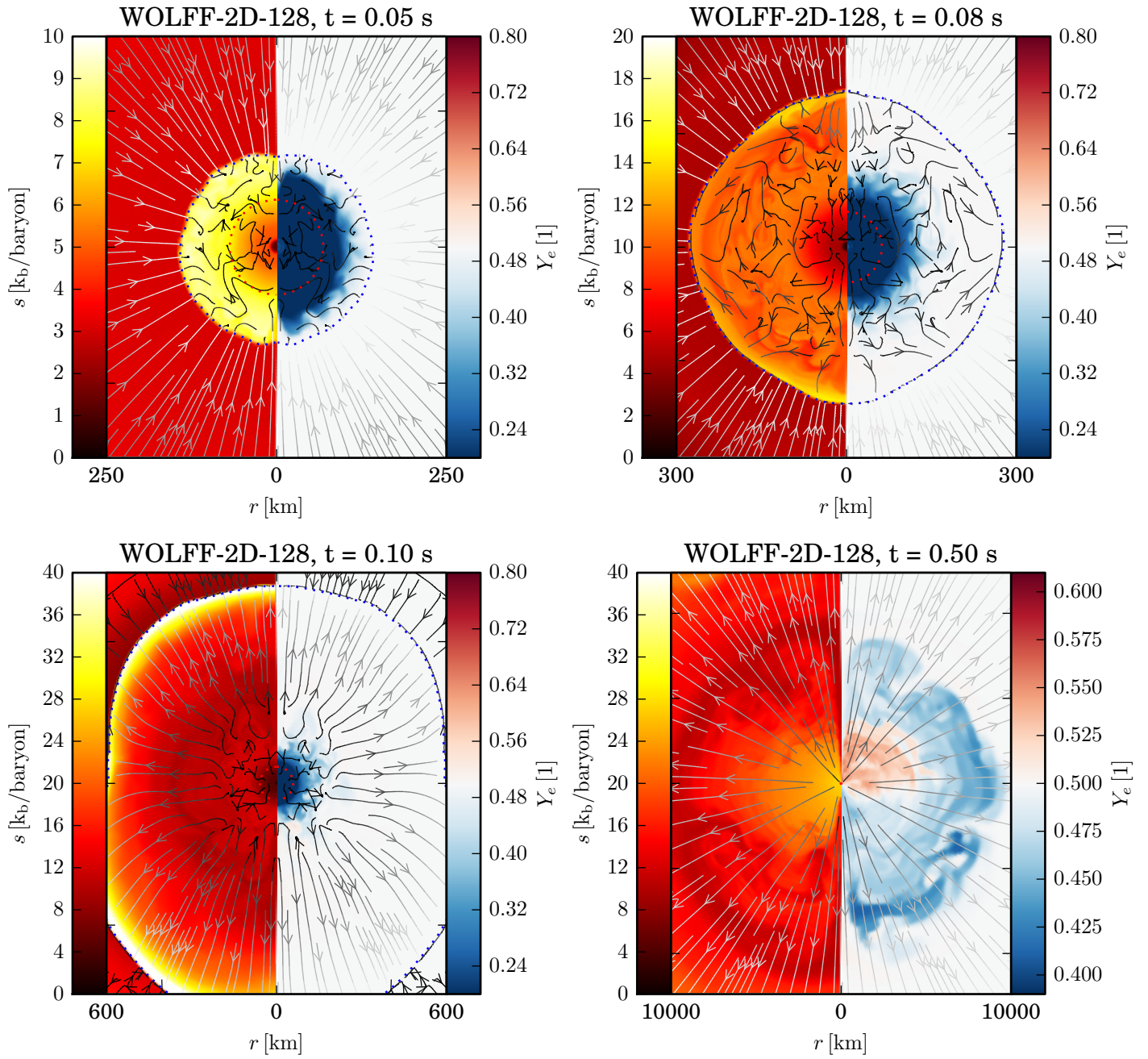


**Figure 4.7:** Two dimensional plots with colour coded entropy per nucleon at the left hand side and  $Y_e$  on the right hand side, at different times for the WOLFF EoS model. The arrows are streamlines, that is lines tangential to the momentary velocity field (which is not to be confused with particle trajectories). The colour of the streamlines indicates the (relative) velocity magnitude, white for large, black for smaller velocities. The red dotted line indicates the proto neutron star radius, and the blue dotted line the shock radius.



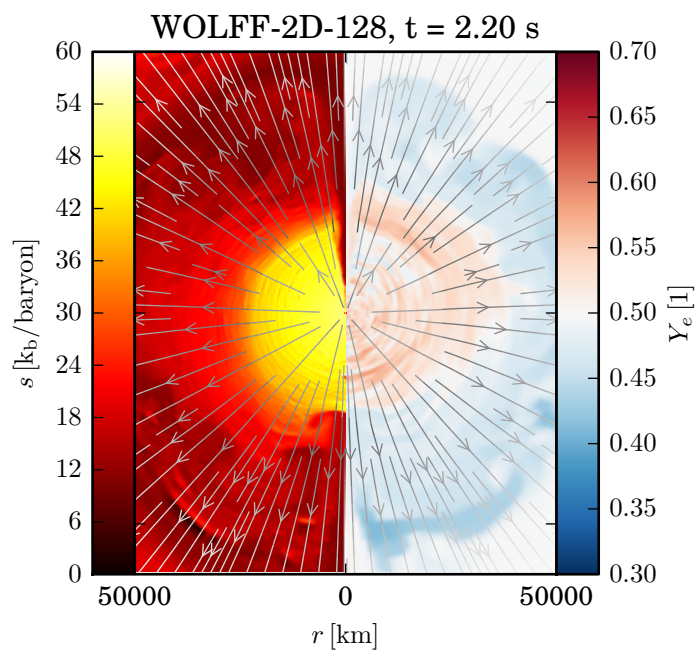


**Figure 4.8:** As Figure 4.7 for the model with the WOLFF EoS at the last simulated time. Nicely seen is the appearance of a proton rich neutrino driven wind from the center.



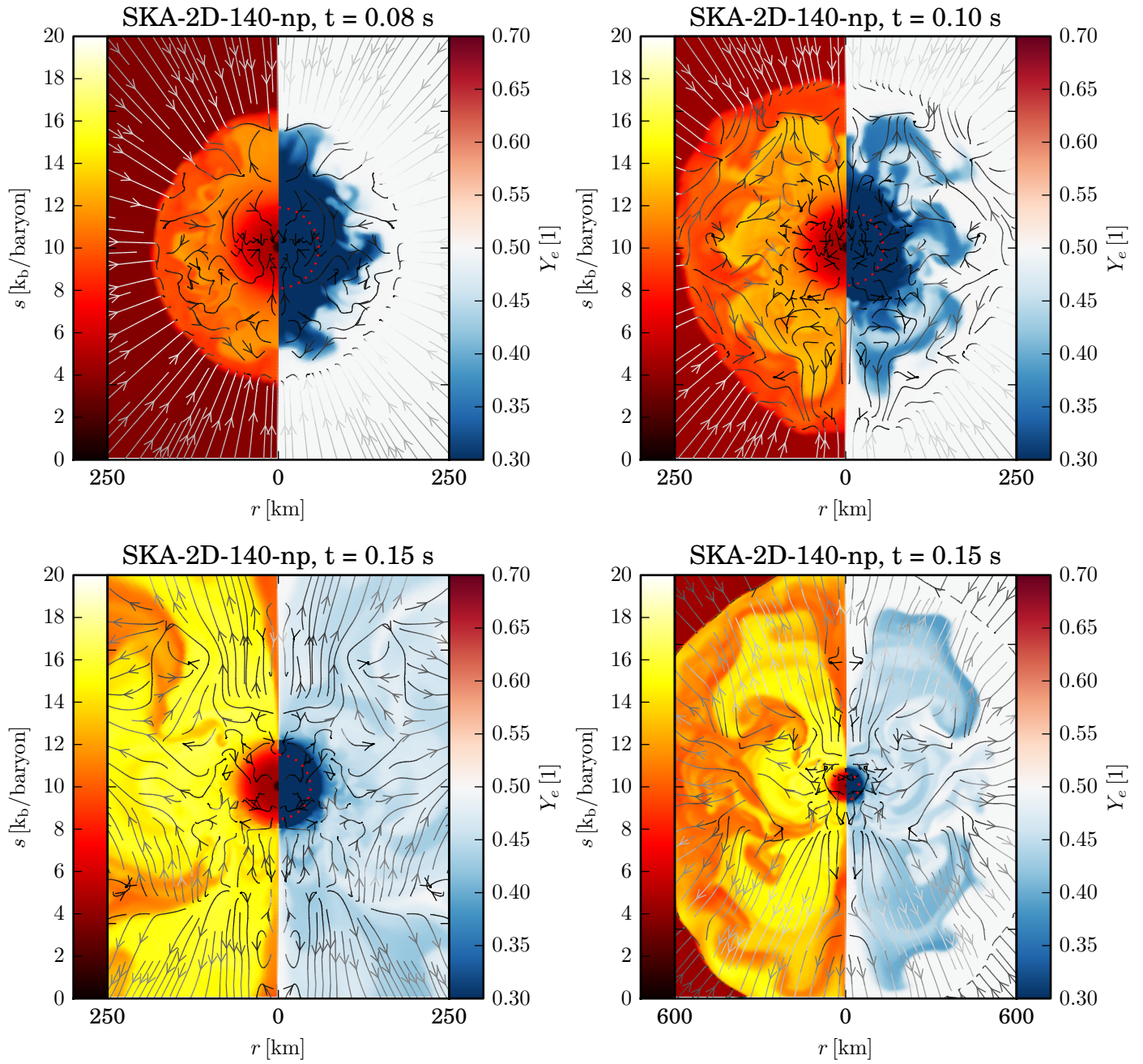


Figure 4.9: As Figure 4.7 for the model with the SKA EoS.



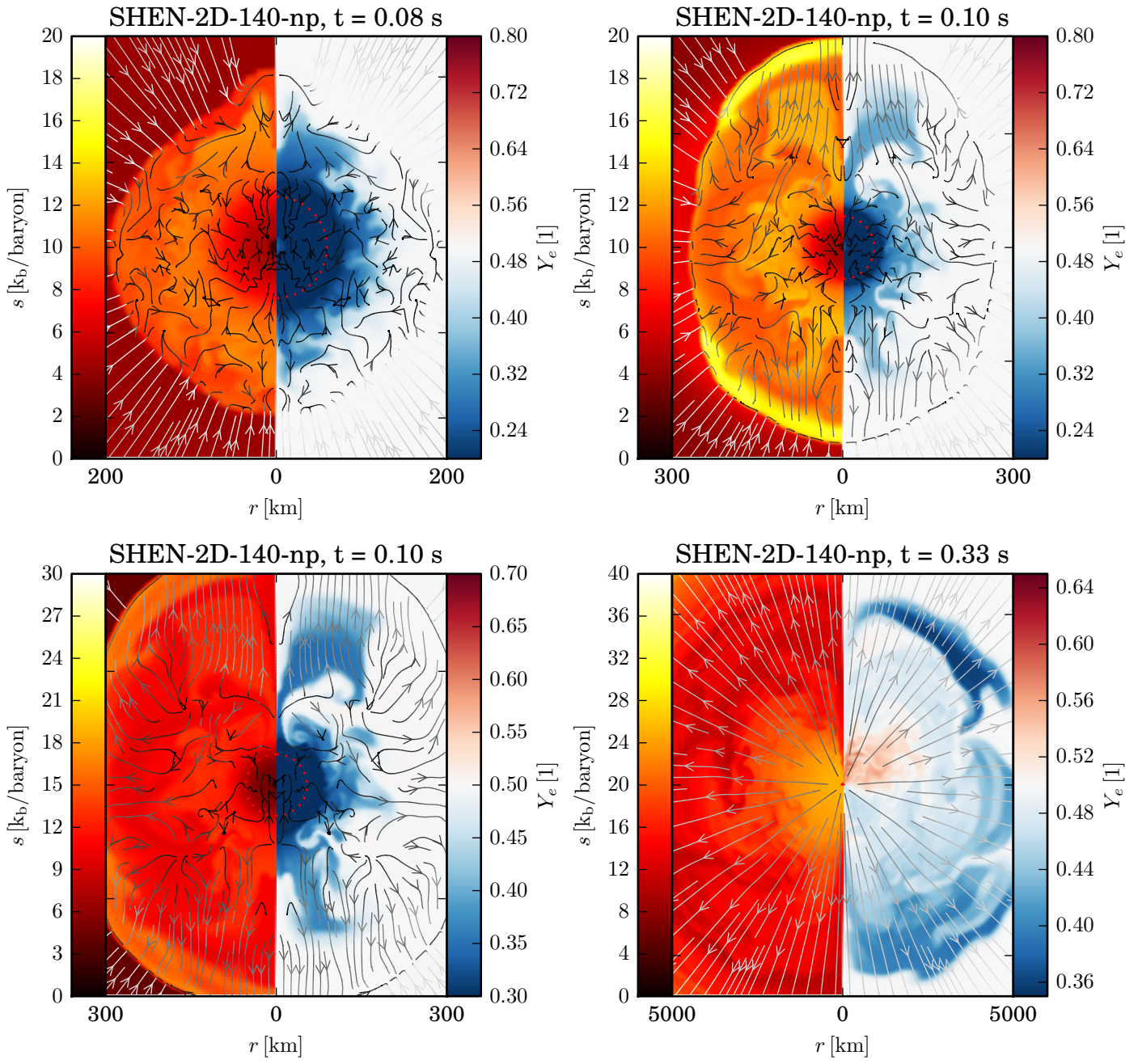
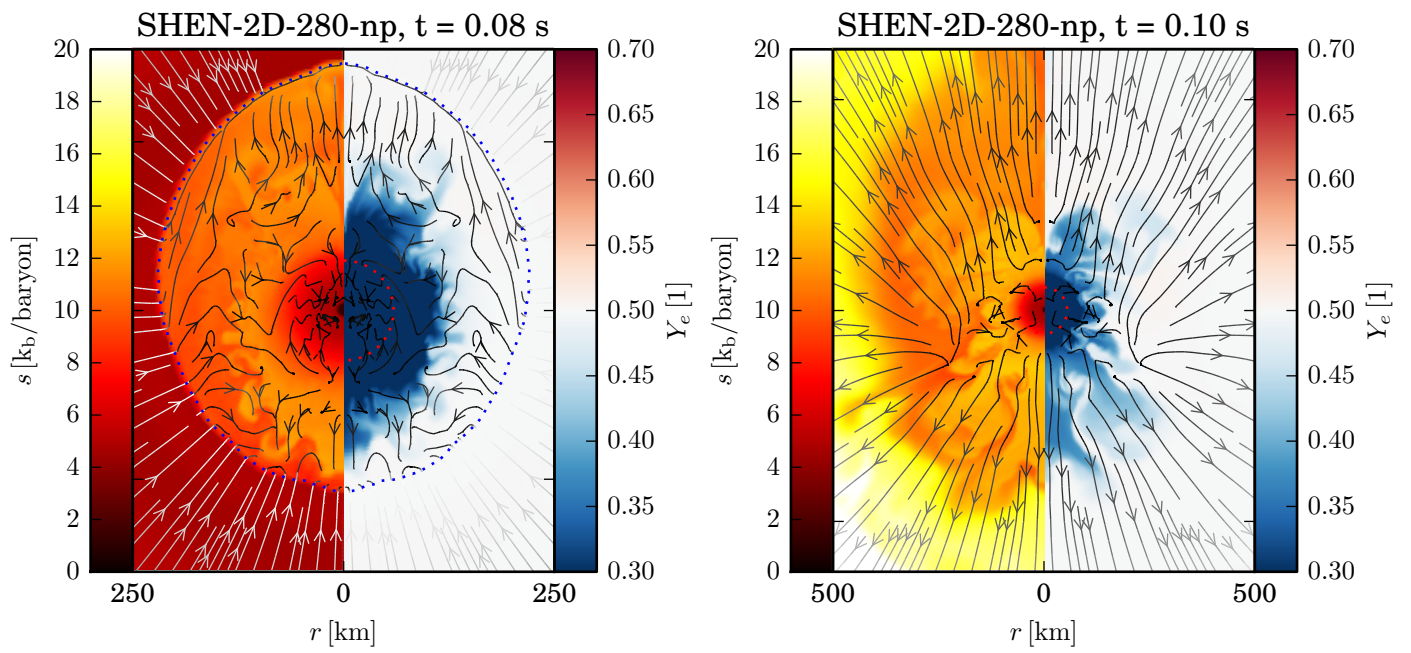


Figure 4.10: As Figure 4.7 for the low resolution model with the SHEN EoS.





**Figure 4.11:** As Figure 4.7 for the high resolution model with the SHEN EoS.



**Table 4.2:** The minimal values of  $Y_e$  and the corresponding entropy for our 2D simulations which ran longer than 70 ms.

Model	SHEN			
	$t$ [s]	$Y_e$ [1]	$s$ [k <sub>B</sub> ]	$\tau_{\text{exp}}$ [ms]
140-np-2D	0.105	0.348	12.67	41.11
280-np-2D	0.095	0.354	12.56	29.45

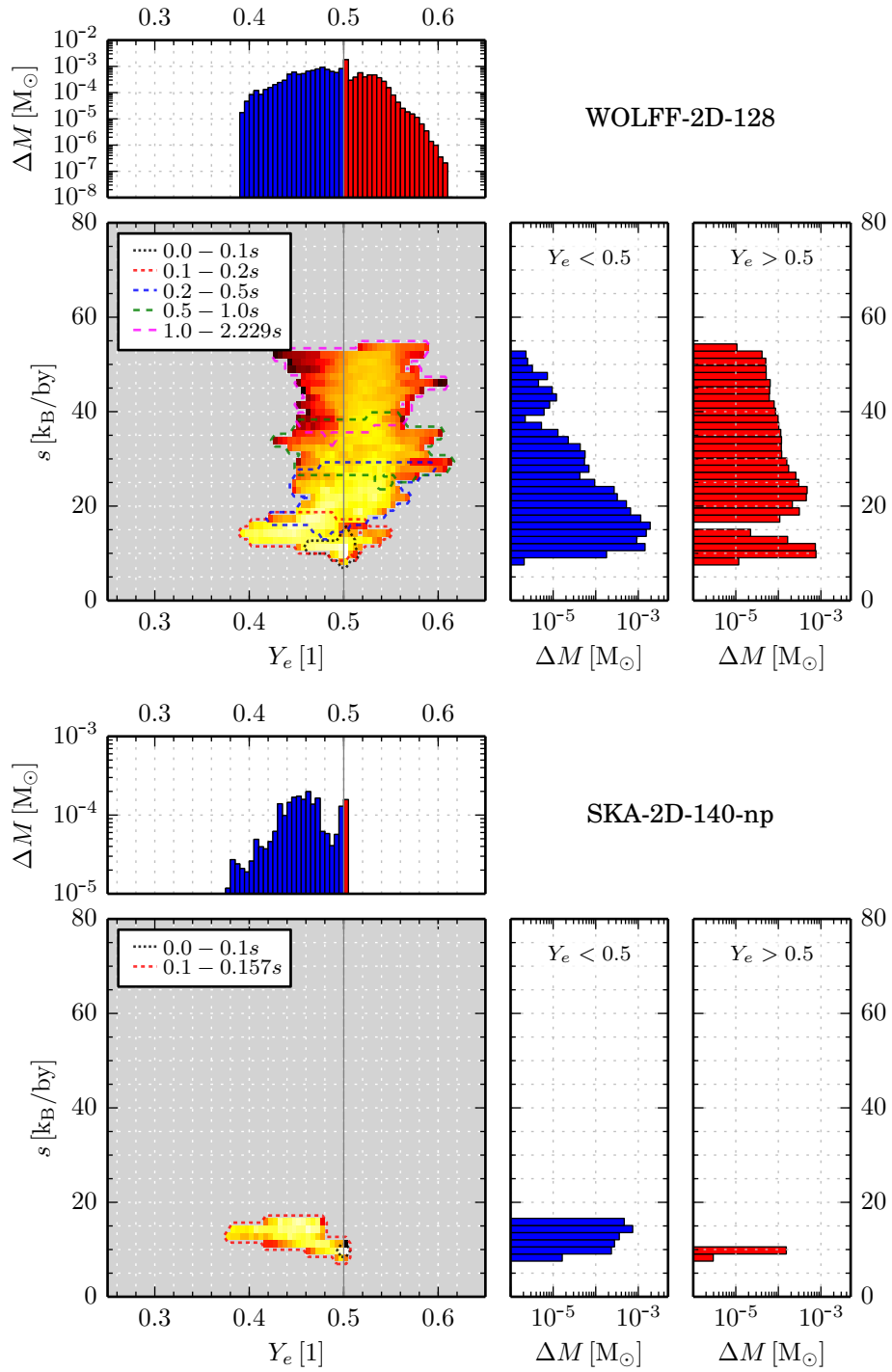
Model	SKA			
	$t$ [s]	$Y_e$ [1]	$s$ [k <sub>B</sub> ]	$\tau_{\text{exp}}$ [ms]
140-np-2D	0.110	0.376	13.22	-62.06

Model	WOLFF			
	$t$ [s]	$Y_e$ [1]	$s$ [k <sub>B</sub> ]	$\tau_{\text{exp}}$ [ms]
128-2D	0.133	0.392	14.22	37.84

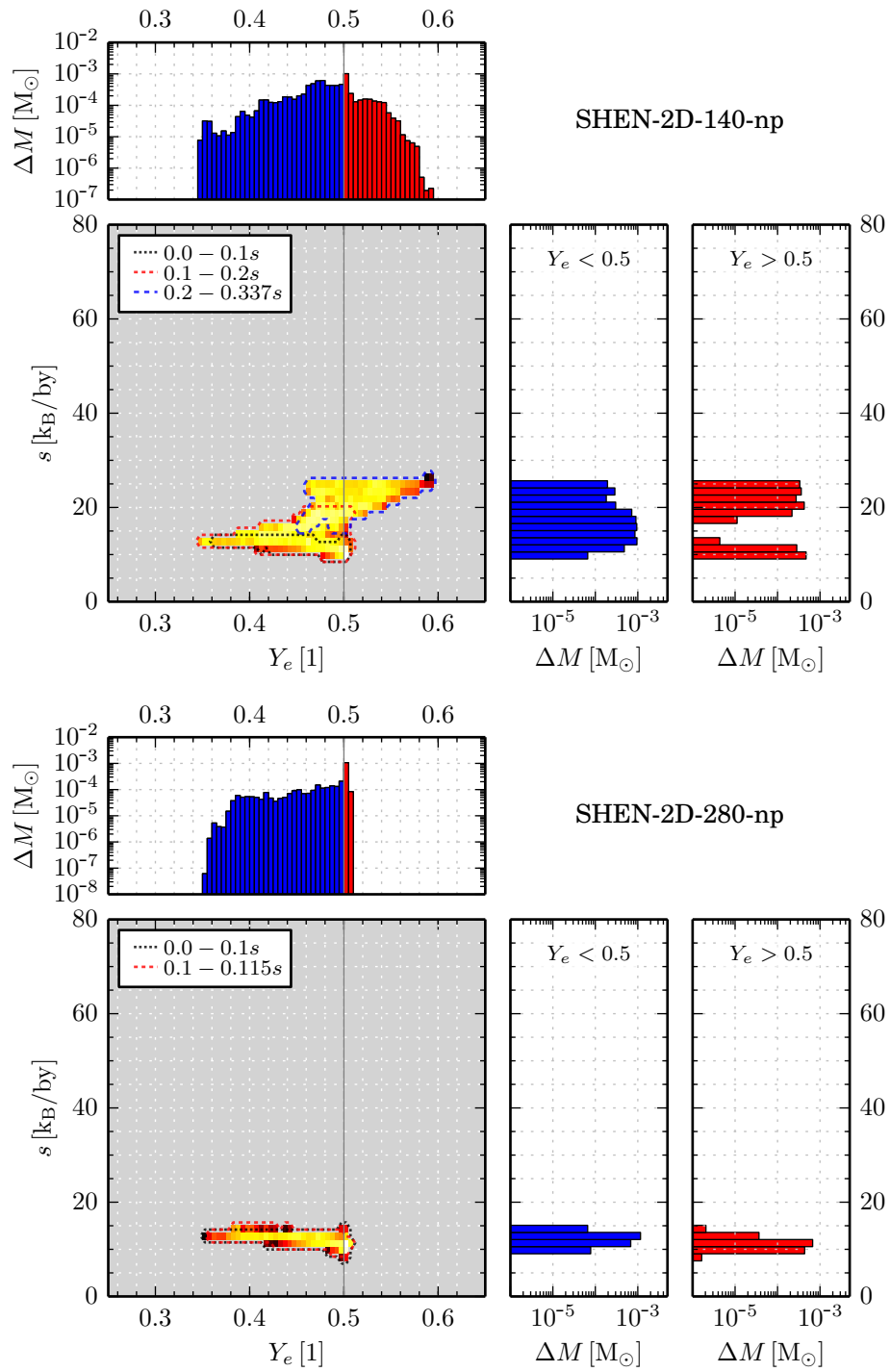
To also quantitatively evaluate these snapshots we show in Figures 4.12 and 4.13 histograms of the entropy and  $Y_e$  of the ejected matter. We see that the matter with the lowest  $Y_e$  gets ejected quite early but we also get some slightly less neutron rich matter ejected at late times. For the model with the WOLFF EoS we get neutron rich matter even after 1 s with  $Y_e \sim 0.42$  and a corresponding entropy of  $s \sim 55 \text{ k}_B$ . In Table 4.2 we show the minimal values of  $Y_e$  in the ejected matter. We see that the model with the SHEN EoS and the lower resolution has the lowest  $Y_e$ . Again, this model, had the explosive shell burning in the outer hull, therefore the value is not reliable. But the SHEN EoS with the higher angular resolution has also a very low  $Y_e$  and this model did collapse normally. We find lower values of  $Y_e$  than Wanajo et al. (2011, 2013a,b) used for their calculations with a similar entropy. This is very exciting, as with these low values of  $Y_e$  the production of heavy elements up to silver and palladium in these events seems feasible!



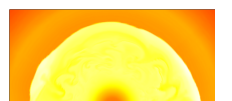


**Figure 4.12:** The histogram in the upper sub-panel shows the  $Y_e$  distribution of the ejected mass, and the right sub-panel shows the entropy distribution, separate for  $Y_e < 0.5$  and  $Y_e > 0.5$ . The central panel shows both the  $Y_e$  and entropy distribution in a 2D histogram, colour coded is the amount of mass in a  $(Y_e, s)$  bin. To also show the time-evolution, we mark the  $Y_e/s$  region of ejected matter for certain time intervals with the dashed lines. One can see that the lowest  $Y_e$  values are ejected earliest. Everything is evaluated 116 ms it streams through a radius of 250 km.





**Figure 4.13:** As Figure 4.12 but for the two models with the SHEN EoS. Note the very low  $Y_e$  values.



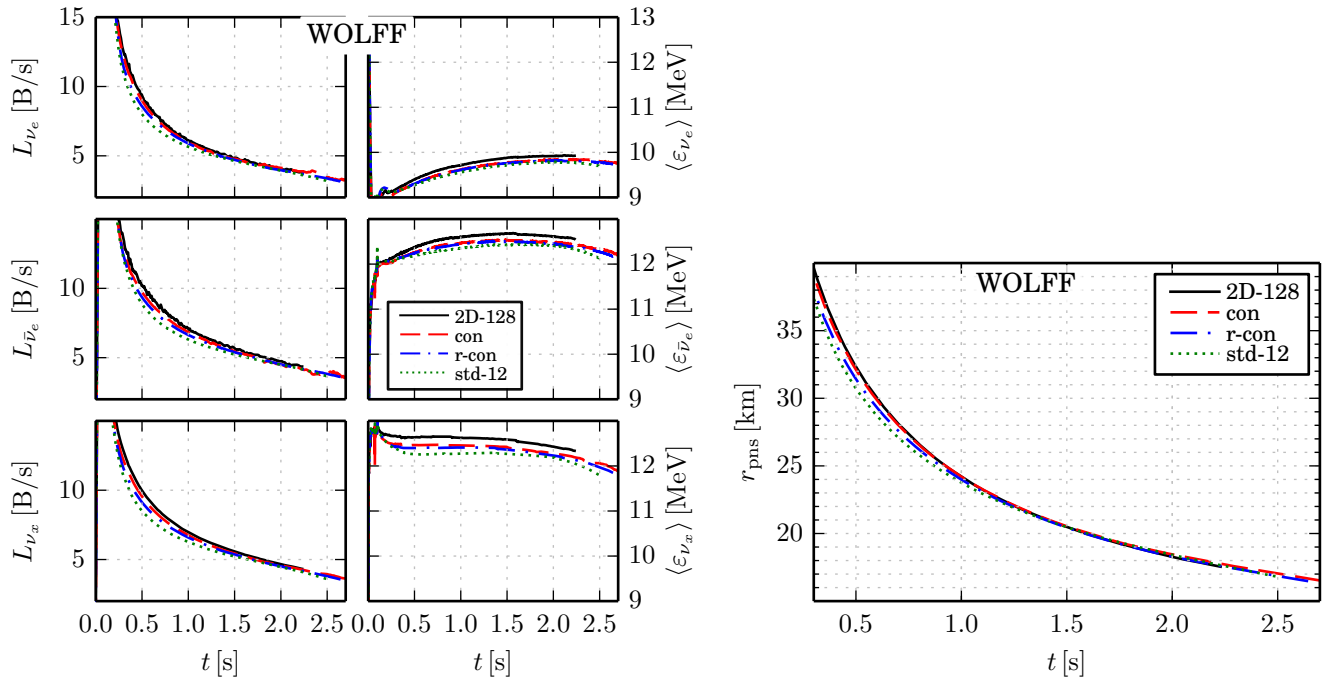


**Figure 4.14:** Comparing the neutrino signal, left hand side, and the proto neutron star radius, right hand side, of the 2D model with suitable 1D models.

## 4.4 Cooling

In this section we will discuss only the model with the WOLFF EoS, as it is the only one which was simulated long enough. To set the cooling of the PNS into a context we will compare the 2D model with suitable 1D models, those are:

- a 1D non-convective model (std-12),
- a 1D model with the Newtonian convection criterion (con),
- a 1D model with the relativistic convection criterion (r-con),

all those 1D models are simulated without the corrected neutrino nucleon opacities, as is the 2D model used here.

First of all, we want to compare the cooling phase of the neutrino signal for our 2D results with our 1D simulation. The left panel of Figure 4.14 shows this comparison. We see that the 2D simulation has for all flavors higher luminosities and higher mean energies than the 1D model, especially for the mean energy of the heavy-lepton neutrinos. Within the 1D models, the Newtonian convection treatment reproduces the 2D simulations better than the relativistic criterion (and of course the non-convective model). The luminosity of the relativistic convection treatment model stays below the 2D model but also below the Newtonian convection model.

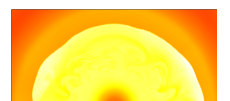


The same is true for the mean energies. We assume that the difference in the 1D convection model lies in the smaller convectively unstable region of the relativistic convection treatment. Also both 1D convection models have a smaller convective unstable region than is found in the 2D model.

On the right hand side of Figure 4.14 we show the comparison of the PNS radii. We see that the 2D model has the highest PNS radius, which is very well reproduced by the 1D model with the Newtonian convection treatment. Only the early maxima of the radius for those two models is slightly different. The PNS radius of the relativistic convection 1D model is almost the same as for the non-convective 1D model. At the end of the simulation, the radii get very similar for all models.

In Figure 4.15 we see the time evolution of certain quantities against the enclosed mass as a radial coordinate. We see that the non-convective 1D model is not in a good agreement with the 2D model. The 1D model with the relativistic convection treatment shows a better agreement, but we get a much better agreement between the 1D model with Newtonian convection treatment and the 2D model. This reinforces our belief that Eq. (2.37) is the proper criterion or that there are still some numerical issues with the version using Eq. (2.38).

All models show a similar behaviour over time. The matter density gets higher with time, as the proto neutron star is still contracting, see Figure 4.14. We can see that the core is still heating up due to the neutrino energy transport inside the PNS. The  $Y_e$  shows nicely the deleptonisation of the PNS over time. In the panel with the entropy we see the influence of the convection, which smoothes out the entropy gradient. We see that this works very well for the 1D model with the Newtonian convection criterion. To illustrate this, we show in Figure 4.16 the time evolution of the convectively unstable regions of the 2D and the 1D model with Newtonian convection criterion. For this, we show a map of  $\omega_{BV}$  for the 1D model in comparison with the absolute value of the velocity field for the 2D simulation. We see that the 1D convectively unstable regions, (where  $\omega_{BV} > 0$ ), represents the 2D convectively unstable regions very well. The only area we can not represent in the 1D case is an unstable region in the centre of the PNS that appears between 1.0 and 2 seconds.



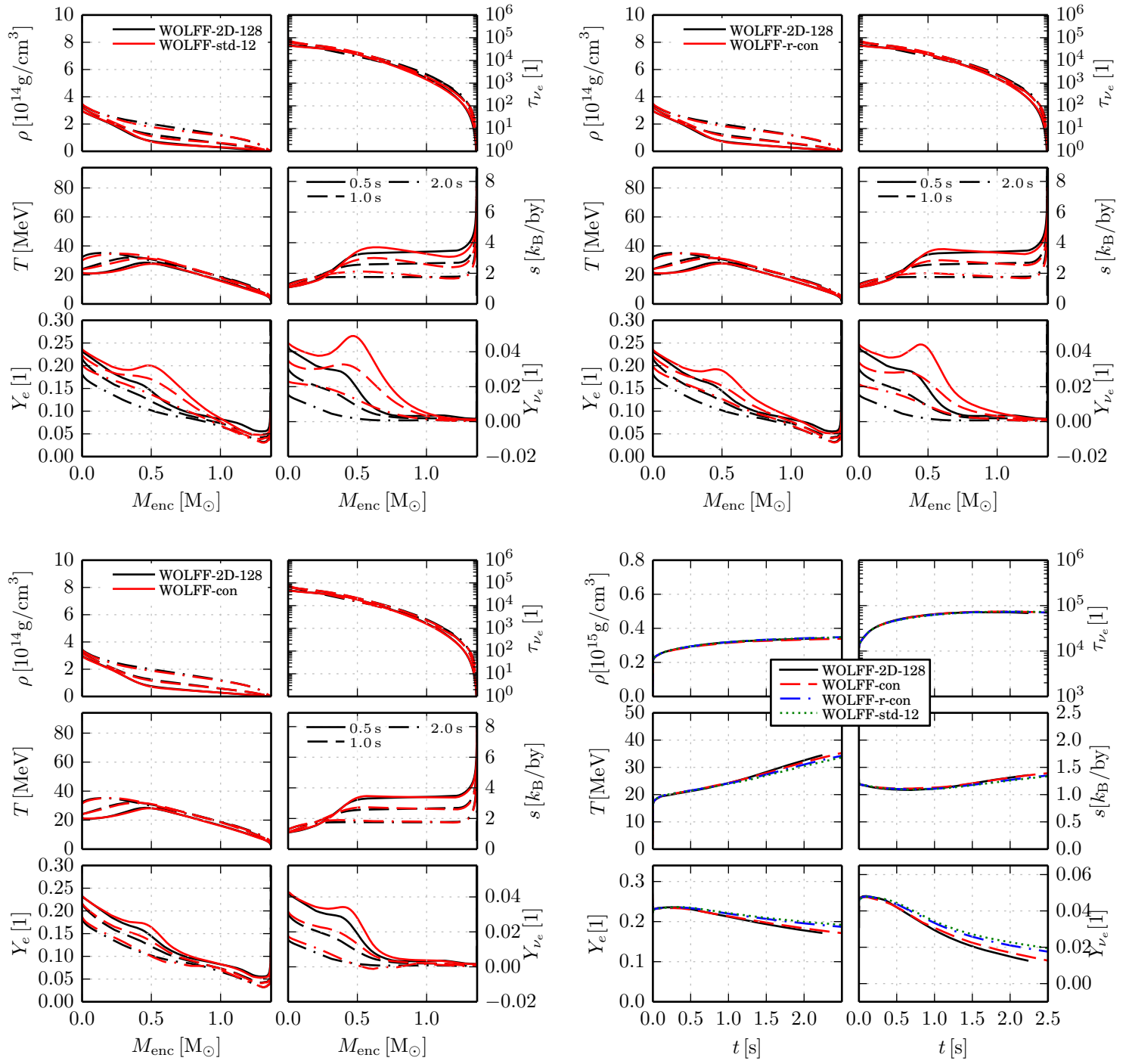


**Figure 4.15:** Similar as Figure 3.33 for the 2D model in comparison with a suitable set of 1D models.



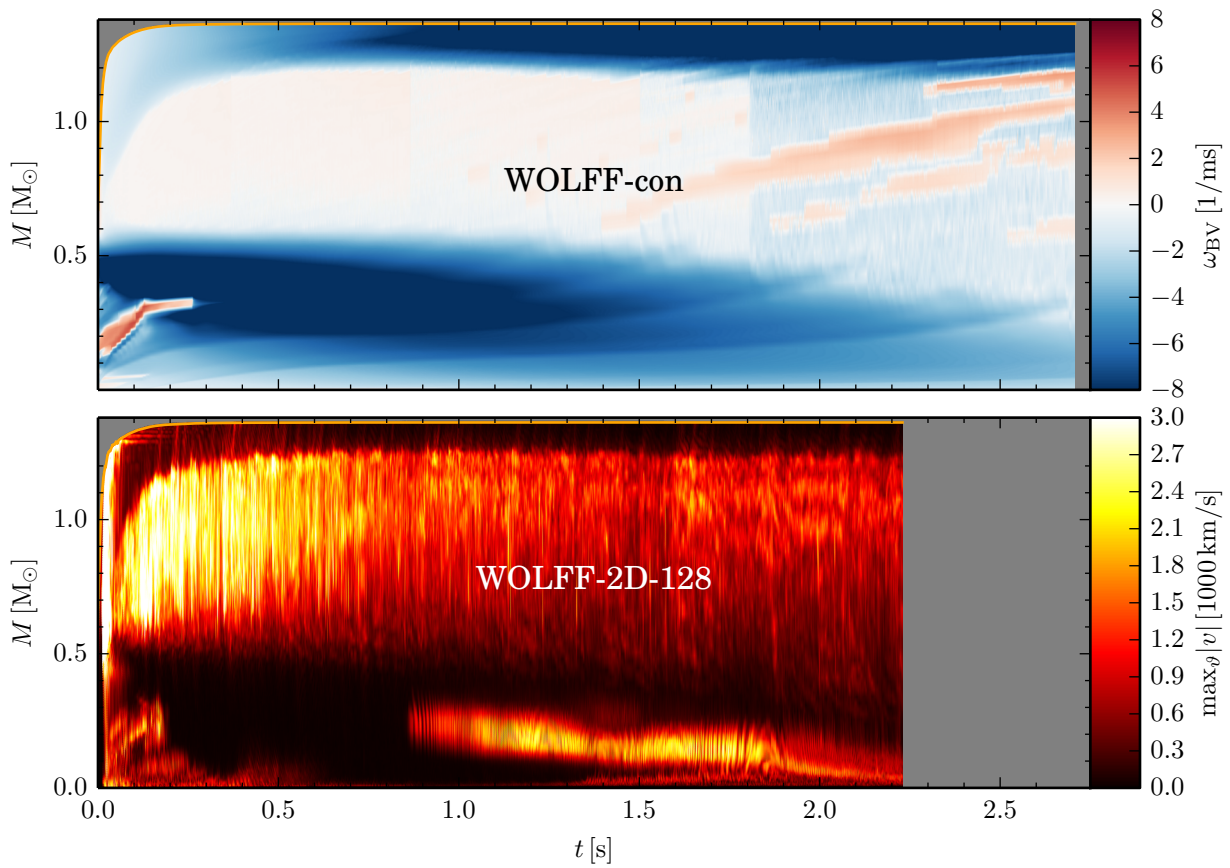


**Figure 4.16:** Comparison of the convection with the mixing length scheme in 1D and for the truly multi dimensional model. To illustrate the 1D convection we use the Brunt-Väisälä frequency  $\omega_{\text{BV}}$  and for the actual 2D convection the local velocity maximum.

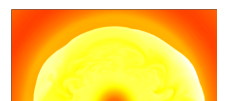


**Table 4.3:** Proto neutron star configuration at the end of the simulations.

Model	SHEN										
	$t_{\text{end}}$ [s]	$r_{\text{pns}}$ [km]	$M_{\text{pns}}$ [ $M_{\odot}$ ]	$M_{\text{G}}$ [ $M_{\odot}$ ]	$r'_{\text{pns}}$ [km]	$M'_{\text{pns}}$ [ $M_{\odot}$ ]	$M'_{\text{G}}$ [ $M_{\odot}$ ]	$E_{\nu}$ [ $B$ ]	[1]	$N_L$ [ $10^{56}$ ]	[1]
140-np-2D	0.337	33.6	1.3653	1.3399	50.7	1.3681	1.3427	45	(0.27)	5.32	(0.80)
280-np-2D	0.115	52.2	1.3447	1.3314	117.8	1.3694	1.3561	24	(0.15)	4.85	(0.74)

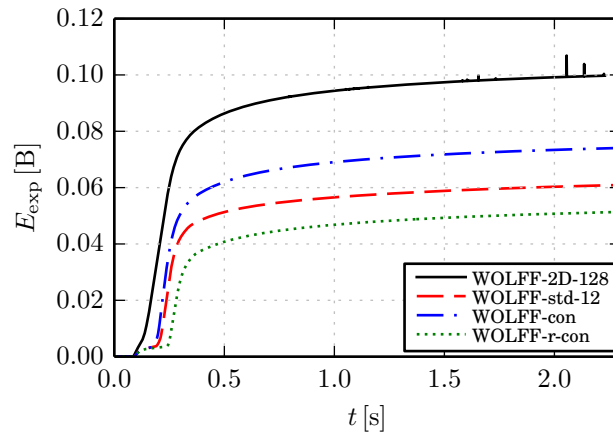
  

Model	SKA										
	$t_{\text{end}}$ [s]	$r_{\text{pns}}$ [km]	$M_{\text{pns}}$ [ $M_{\odot}$ ]	$M_{\text{G}}$ [ $M_{\odot}$ ]	$r'_{\text{pns}}$ [km]	$M'_{\text{pns}}$ [ $M_{\odot}$ ]	$M'_{\text{G}}$ [ $M_{\odot}$ ]	$E_{\nu}$ [ $B$ ]	[1]	$N_L$ [ $10^{56}$ ]	[1]
140-np-2D	0.157	46.4	1.3579	1.3419	90.0	1.3707	1.3547	29	(0.16)	4.88	(0.73)

Model	WOLFF										
	$t_{\text{end}}$ [s]	$r_{\text{pns}}$ [km]	$M_{\text{pns}}$ [ $M_{\odot}$ ]	$M_{\text{G}}$ [ $M_{\odot}$ ]	$r'_{\text{pns}}$ [km]	$M'_{\text{pns}}$ [ $M_{\odot}$ ]	$M'_{\text{G}}$ [ $M_{\odot}$ ]	$E_{\nu}$ [ $B$ ]	[1]	$N_L$ [ $10^{56}$ ]	[1]
128-2D	2.229	17.5	1.3619	1.2962	21.7	1.3621	1.2964	118	(0.67)	6.42	(0.96)
con-1D	2.707	16.5	1.3644	1.2944	20.1	1.3645	1.2946	125	(0.71)	6.61	(0.99)
r-con-1D	2.645	16.5	1.3672	1.2994	20.0	1.3674	1.2996	121	(0.69)	6.31	(0.94)
std-12-1D	2.489	16.8	1.3661	1.3023	20.5	1.3663	1.3024	114	(0.65)	6.17	(0.92)





**Figure 4.17:** Explosion energy of the 2D model compared with suitable 1D models.

## 4.5 Explosion energy

For calculating the explosion energy of our 2D models only the WOLFF-2D-128 model, ran long enough. Here we will therefore only discuss the low resolution model with the WOLFF EoS. The explosion energy is calculated as described in Section 3.7.

In Figure 4.17 we show the explosion energy of this 2D model and compare it with suitable 1D models.

We saw in the section above that the 1D model with Newtonian convection treatment agrees better with the 2D model than the 1D model with the relativistic convection treatment. This is again seen here, even more pronounced, as the explosion energy of the relativistic convection model is barely half of that in 2D. Also the 1D model with the Newtonian convection does not attain an explosion energy that is as high as the 2D model, as we can only approximate the proto neutron star convection there. In the case of the 2D model, we have additionally the neutrino driven convection above the proto neutron star in the accretion layer. Therefore, matter can flow back and get heated repeatedly. Also, the explosion itself is a little bit faster in 2D, thus ejecting more matter.

All in all, we see that the 2D explosion energy is higher higher than all 1D explosion energies shown, see also Table 4.4. This was also found by Kitaura (2007). He showed in his Appendix II, Figure 3.4, a comparison of the explosion energy of a 2D and 1D model done with the LS180 EoS. In contrast to that, Janka et al. (2008) sees that in their case (see their Figure 5) the explosion energy of the 2D and 1D model, also done with the LS180, are quite similar.



**Table 4.4:** Properties of the explosion energy at the end of our simulations, similar to Table 3.11.

Model	$t_{\text{end}}$ [s]	$t_{\text{expl}}$ [s]	$t_{\text{shock}}$ [s]	$M_{\text{ej}}$ [ $10^{-3}M_{\odot}$ ]	$E_{\text{expl, He}}$ [B]	$E_{\text{expl}}$ [B]	$E_{\text{expl, Fe}}$ [B]
128-2D	2.229	0.070	0.094	15.4	0.064	0.100	0.112
con-1D	2.707	0.098	0.101	13.0	0.048	0.075	0.089
r-con-1D	2.645	0.098	0.100	10.1	0.032	0.052	0.063
std-12-1D	2.489	0.098	0.100	11.2	0.038	0.061	0.073



## 5 Summary and Conclusion

We have presented a number of 1D and 2D simulations of the electron capture supernova of an ONeMg progenitor, with five different Equation of State models.

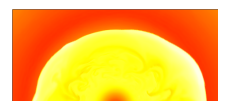
We showed that general relativity plays an important role for the result of supernova simulations, even compared to post-Newtonian simulations. In the post-Newtonian case one can reach velocities which are far too large, even higher than the speed of light. But accurate velocities are very important for the details of the mass ejection. It was already hinted that neutron rich matter can be ejected by convective motions during the explosion, we investigated this in detail. We found that neutron rich matter gets ejected quite early and therefore will also stay neutron rich, as the neutrinos do not have a chance to change the composition that quickly. This re-opens the possibility of r-process nucleosynthesis in a supernova environment (Wanajo et al., 2013a; Wanajo, 2013). We also showed that the EoS plays a huge role in the amount, distribution and composition of the ejected neutron rich matter. Most of our 2D simulations did not run long enough yet and need to be studied further in the future. It would also be interesting to investigate the relative effect of the improved neutrino opacities on 2D simulations. Also a fully 3D simulation of an ECSN would be an interesting challenge to study. However, in GR this probably would be computationally excessively expensive.

We saw that the improved neutrino opacities play an important role, especially for the neutrino driven wind phase. There, 1D simulations are appropriate, as the wind phase is again very spherically symmetric, which we have actually seen in the first long-time 2D proto neutron star cooling simulations with VERTEX-CoCoNuT that we presented here. With the improved opacities, the wind  $Y_e$  gets reduced considerably and depends more strongly on the EoS. We still always find proton rich ejecta, but it is conceivable other EoS models might produce neutron rich outflows, see e.g. Roberts (2012c); Hüdepohl (2014).

A convection treatment in the form of a mixing length scheme was adapted to our GR code and improved the 1D simulations considerably. An effect was seen for the explosion itself, but the influence is most important during the cooling phase. We could show that the mixing length prescription matches our truly multi dimensional models very well. The proto neutron star convection strongly accelerates the cooling and deleptonization of the proto neutron star. Also here we saw a strong dependence on the EoS.

We conclude that both convection and improved neutrino nucleon opacities should be considered in all future simulations.

The stronger than previously thought EoS dependence creates possibilities and problems: The possibility that r-process nucleosynthesis might again be feasible in

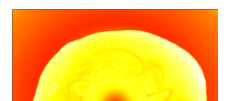


a supernova environment, with the problem that much of the high density Equation of State is still poorly constrained.



# Bibliography

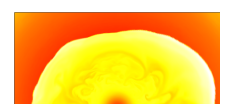
- Alexeyev, E. N., Alexeyeva, L. N., Volchenko, V. I., Krivosheina, I. V. (1988). Characteristics of a neutrino signal from SN 1987A, detected by the Baksan underground scintillation telescope of the Nuclear Research Institute of the Soviet Academy of Sciences. *Pis ma Astronomicheskii Zhurnal*, volume 14, pp. 99–106.
- Antoniadis, J., Freire, P. C. C., Wex, N., Tauris, T. M., Lynch, R. S., van Kerkwijk, M. H., Kramer, M., Bassa, C., Dhillon, V. S., Driebe, T., Hessels, J. W. T., Kaspi, V. M., Kondratiev, V. I., Langer, N., Marsh, T. R., McLaughlin, M. A., Pennucci, T. T., Ransom, S. M., Stairs, I. H., van Leeuwen, J., Verbiest, J. P. W., Whelan, D. G. (2013). A Massive Pulsar in a Compact Relativistic Binary. *Science*, volume 340, p. 448. doi:10.1126/science.1233232.
- Arcones, A., Thielemann, F.-K. (2013). Neutrino-driven wind simulations and nucleosynthesis of heavy elements. *Journal of Physics G Nuclear Physics*, volume 40(1), 013201. doi:10.1088/0954-3899/40/1/013201.
- Arnowitz, R., Deser, S., Misner, C. W. (2008). Republication of: The dynamics of general relativity. *General Relativity and Gravitation*, volume 40, pp. 1997–2027. doi:10.1007/s10714-008-0661-1.
- Banyuls, F., Font, J. A., Ibanez, J. M. A., Marti, J. M. A., Miralles, J. A. (1997). Numerical 3+1 General Relativistic Hydrodynamics: A Local Characteristic Approach. *The Astrophysical Journal*, volume 476, p. 221. doi:10.1086/303604.
- Baron, E., Cooperstein, J., Kahana, S. (1987). Collapse of 9 solar mass stars. *The Astrophysical Journal*, volume 320, pp. 300–303. doi:10.1086/165541.
- Bethe, H. A. (1990). Supernova mechanisms. *Reviews of Modern Physics*, volume 62, pp. 801–866.
- Bionta, R. M., Blewitt, G., Bratton, C. B., Caspere, D., Ciocio, A. (1987). Observation of a neutrino burst in coincidence with supernova 1987A in the Large Magellanic Cloud. *Physical Review Letters*, volume 58, pp. 1494–1496.
- Blaschke, D. B., Grigorian, H. A., Alvarez-Castillo, D. E., Ayriyan, A. S. (2014). Mass and radius constraints for compact stars and the QCD phase diagram. *Journal of Physics Conference Series*, volume 496(1), 012002. doi:10.1088/1742-6596/496/1/012002.



- Bruenn, S. W. (1985). Stellar core collapse – numerical model and infall epoch. *The Astrophysical Journal Supplement Series*, volume 58, pp. 771–841. doi:10.1086/191056.
- Bruenn, S. W., Mezzacappa, A. (1997). Ion screening effects and stellar collapse. *Physical Review D*, volume 56, pp. 7529–7547. doi:10.1103/PhysRevD.56.7529.
- Buras, R., Janka, H.-T., Keil, M. T., Raffelt, G. G., Rampp, M. (2003). Electron neutrino pair annihilation: A new source for muon and tau neutrinos in supernovae. *The Astrophysical Journal*, volume 587, pp. 320–326. doi:10.1086/368015.
- Buras, R., Rampp, M., Janka, H.-T., Kifonidis, K. (2006). Two-dimensional hydrodynamic core-collapse supernova simulations with spectral neutrino transport. I. Numerical method and results for a 15  $M_{\odot}$  star. *Astronomy & Astrophysics*, volume 447, pp. 1049–1092. doi:10.1051/0004-6361:20053783.
- Burrows, A. (2012). Multi-dimensional core-collapse supernova explosions. In S. Kubono, T. Hayakawa, T. Kajino, H. Miyatake, T. Motobayashi, K. Nomoto, editors, *American Institute of Physics Conference Series*, volume 1484 of *American Institute of Physics Conference Series*, pp. 5–12. doi:10.1063/1.4763364.
- Burrows, A., Lattimer, J. M. (1985). The prompt mechanism of Type II supernovae. *The Astrophysical Journal Letters*, volume 299, pp. L19–L22. doi:10.1086/184572.
- Burrows, A., Sawyer, R. F. (1998). Effects of correlations on neutrino opacities in nuclear matter. *Physical Review C*, volume 58, pp. 554–571. doi:10.1103/PhysRevC.58.554.
- Burrows, A., Sawyer, R. F. (1999). Many-body corrections to charged-current neutrino absorption rates in nuclear matter. *Physical Review C*, volume 59, pp. 510–514. doi:10.1103/PhysRevC.59.510.
- Burrows, A., Dessart, L., Ott, C. D., Livne, E. (2007). Multi-dimensional explorations in supernova theory. *Physics Reports*, volume 442, pp. 23–37. doi:10.1016/j.physrep.2007.02.001.
- Cardall, C. Y., Fuller, G. M. (1997). General Relativistic Effects in the Neutrino-driven Wind and r-Process Nucleosynthesis. *The Astrophysical Journal Letters*, volume 486, pp. L111–L114. doi:10.1086/310838.
- Carter, G. W., Prakash, M. (2002). The quenching of the axial coupling in nuclear and neutron-star matter. *Physics Letters B*, volume 525, pp. 249–254. doi:10.1016/S0370-2693(01)01452-6.
- Catchpole, R. M. (2012). 25 Years after Supernova 1987A. *Monthly Notes of the Astronomical Society of South Africa*, volume 71, pp. 65–71.
- Cernohorsky, J. (1994). Symmetries in neutrino-electron scattering. *The Astrophysical Journal*, volume 433, pp. 247–249. doi:10.1086/174639.



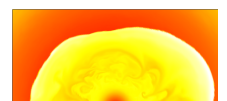
- Colgate, S. A., Petschek, A. G. (1980). The Rayleigh-Taylor instability overturn of supernova cores during bouncing and resulting neutrino energy release. *Highlights of Astronomy*, volume 5, pp. 517–519.
- Colgate, S. A., White, R. H. (1966). The Hydrodynamic Behavior of Supernovae Explosions. *The Astrophysical Journal*, volume 143, pp. 626–+.
- Colgate, S. A., Grasberger, W. H., White, R. H. (1961). The Dynamics of Supernova Explosions. *Astronomical Journal*, volume 66, p. 280. doi:10.1086/108573.
- Couch, S. M. (2013). On the Impact of Three Dimensions in Simulations of Neutrino-driven Core-collapse Supernova Explosions. *The Astrophysical Journal*, volume 775, 35. doi:10.1088/0004-637X/775/1/35.
- Demorest, P. B., Pennucci, T., Ransom, S. M., Roberts, M. S. E., Hessels, J. W. T. (2010). A two-solar-mass neutron star measured using Shapiro delay. *Nature*, volume 467, pp. 1081–1083. doi:10.1038/nature09466.
- Dessart, L., Burrows, A., Livne, E., Ott, C. D. (2006). Multidimensional Radiation/Hydrodynamic Simulations of Proto-Neutron Star Convection. *The Astrophysical Journal*, volume 645, pp. 534–550. doi:10.1086/504068.
- Dimmelmeier, H. (2001). *General Relativistic Collapse of Rotating Stellar Cores in Axisymmetry*. Dissertation, Technische Universität München, München. <http://nbn-resolving.de/urn/resolver.pl?urn:nbn:de:bvb:91-diss2001110613006>.
- Dolence, J. C., Burrows, A., Murphy, J. W., Nordhaus, J. (2013). Dimensional Dependence of the Hydrodynamics of Core-collapse Supernovae. *The Astrophysical Journal*, volume 765, 110. doi:10.1088/0004-637X/765/2/110.
- Duncan, R. C., Shapiro, S. L., Wasserman, I. (1986). Neutrino-driven winds from young, hot neutron stars. *The Astrophysical Journal*, volume 309, pp. 141–160. doi:10.1086/164587.
- Epstein, R. I. (1979). Lepton-driven convection in supernovae. *Monthly Notices of the Royal Astronomical Society*, volume 188, pp. 305–325.
- Fischer, T., Whitehouse, S. C., Mezzacappa, A., Thielemann, F., Liebendörfer, M. (2010). Protoneutron star evolution and the neutrino-driven wind in general relativistic neutrino radiation hydrodynamics simulations. *Astronomy & Astrophysics*, volume 517, pp. A80+. doi:10.1051/0004-6361/200913106.
- Freiburghaus, C., Rembges, J.-F., Rauscher, T., Kolbe, E., Thielemann, F.-K., Kratz, K.-L., Pfeiffer, B., Cowan, J. J. (1999). The Astrophysical r-Process: A Comparison of Calculations following Adiabatic Expansion with Classical Calculations Based on Neutron Densities and Temperatures. *The Astrophysical Journal*, volume 516, pp. 381–398. doi:10.1086/307072.



- Fuller, G. M., Meyer, B. S. (1995). Neutrino Capture and Supernova Nucleosynthesis. *The Astrophysical Journal*, volume 453, p. 792. doi:10.1086/176442.
- Fuller, G. M., Yong-Zhong, Q. (1996). Neutrino gravitational redshift and the electron fraction above nascent neutron stars. *Nuclear Physics A*, volume 606, pp. 167–172. doi:10.1016/0375-9474(96)00268-0.
- Hanke, F., Marek, A., Müller, B., Janka, H.-T. (2012). Is Strong SASI Activity the Key to Successful Neutrino-driven Supernova Explosions? *The Astrophysical Journal*, volume 755, 138. doi:10.1088/0004-637X/755/2/138.
- Hanke, F., Müller, B., Wongwathanarat, A., Marek, A., Janka, H.-T. (2013). SASI Activity in Three-dimensional Neutrino-hydrodynamics Simulations of Supernova Cores. *The Astrophysical Journal*, volume 770, 66. doi:10.1088/0004-637X/770/1/66.
- Hannestad, S., Raffelt, G. (1998). Supernova neutrino opacity from nucleon–nucleon bremsstrahlung and related processes. *The Astrophysical Journal*, volume 507, pp. 339–352. doi:10.1086/306303.
- Hillebrandt, W., Wolff, R. G. (1985). Models of Type II Supernova Explosions. In *Nucleosynthesis : Challenges and New Developments*, Ed. Arnett, W. D. and Truran, J. W., p. 131.
- Hillebrandt, W., Wolff, R. G., Nomoto, K. (1984). Supernova explosions of massive stars – The mass range 8 to 10 solar masses. *Astronomy & Astrophysics*, volume 133, pp. 175–184.
- Hirata, K., Kajita, T., Koshiba, M., Nakahata, M., Oyama, Y. (1987). Observation of a neutrino burst from the supernova SN1987A. *Physical Review Letters*, volume 58, pp. 1490–1493. doi:10.1103/PhysRevLett.58.1490.
- Hoffman, R. D., Woosley, S. E., Qian, Y.-Z. (1997). Nucleosynthesis in neutrino-driven winds. ii. implications for heavy element synthesis. *The Astrophysical Journal*, volume 482(2), pp. 951–962. doi:10.1086/304181.
- Horowitz, C. J. (1997). Neutrino trapping in a supernova and the screening of weak neutral currents. *Physical Review D*, volume 55, pp. 4577–4581. doi:10.1103/PhysRevD.55.4577.
- Horowitz, C. J. (2002). Weak magnetism for antineutrinos in supernovae. *Physical Review D*, volume 65(4), pp. 043001–+. doi:10.1103/PhysRevD.65.043001.
- Hüdepohl, L. (2009). *Neutrinos cooling evolution of the newly formed neutron stars from electron capture supernovae*, Diploma Thesis. Master’s thesis, Technische Universität München.
- Hüdepohl, L. (2014). *Neutrinos from the Formation, Cooling and Black Hole Collapse of Neutron Stars*. Ph.D. thesis, Technische Universität München.



- Hüdepohl, L., Müller, B., Janka, H., Marek, A., Raffelt, G. G. (2010). Neutrino Signal of Electron-Capture Supernovae from Core Collapse to Cooling. *Physical Review Letters*, volume 104(25), pp. 251101–+. [doi:10.1103/PhysRevLett.104.251101](https://doi.org/10.1103/PhysRevLett.104.251101).
- Janka, H.-T. (1999). unpublished.
- Janka, H.-T. (2001). Conditions for shock revival by neutrino heating in core-collapse supernovae. *Astronomy & Astrophysics*, volume 368, pp. 527–560. [doi:10.1051/0004-6361:20010012](https://doi.org/10.1051/0004-6361:20010012).
- Janka, H.-T. (2012). Explosion Mechanisms of Core-Collapse Supernovae. *Annual Review of Nuclear and Particle Science*, volume 62, pp. 407–451. [doi:10.1146/annurev-nucl-102711-094901](https://doi.org/10.1146/annurev-nucl-102711-094901).
- Janka, H.-T., Müller, E. (1996). Neutrino heating, convection, and the mechanism of Type-II supernova explosions. *Astronomy & Astrophysics*, volume 306, pp. 167–+.
- Janka, H.-T., Müller, B., Kitaura, F. S., Buras, R. (2008). Dynamics of shock propagation and nucleosynthesis conditions in O-Ne-Mg core supernovae. *Astronomy & Astrophysics*, volume 485, pp. 199–208. [doi:10.1051/0004-6361:20079334](https://doi.org/10.1051/0004-6361:20079334).
- Janka, H.-T., Hanke, F., Hüdepohl, L., Marek, A., Müller, B., Obergaullinger, M. (2012). Core-collapse supernovae: Reflections and directions. *Progress of Theoretical and Experimental Physics*, volume 2012(1), 01A309. [doi:10.1093/ptep/pts067](https://doi.org/10.1093/ptep/pts067).
- Kippenhahn, R., Weigert, A., Weiss, A. (2012). *Stellar Structure and Evolution, Second Edition*. Astronomy and Astrophysics Library. Springer, Berlin. ISBN 978-3-642-30255-8.
- Kitaura, F. S., Janka, H.-T., Hillebrandt, W. (2006). Explosions of O-Ne-Mg cores, the Crab supernova, and subluminous type II-P supernovae. *Astronomy & Astrophysics*, volume 450, pp. 345–350. [doi:10.1051/0004-6361:20054703](https://doi.org/10.1051/0004-6361:20054703).
- Kitaura, F. S. J. (2007). *Cosmic cartography*. Ph.D. thesis, Ludwig-Maximilians-Universität. <http://nbn-resolving.de/urn:nbn:de:bvb:19-81208>.
- Langanke, K., Martínez-Pinedo, G., Sampaio, J. M., Dean, D. J., Hix, W. R., Messer, O. E., Mezzacappa, A., Liebendörfer, M., Janka, H.-T., Rampp, M. (2003). Electron capture rates on nuclei and implications for stellar core collapse. *Physical Review Letters*, volume 90(24), pp. 241102–+. [doi:10.1103/PhysRevLett.90.241102](https://doi.org/10.1103/PhysRevLett.90.241102).
- Langanke, K., Martínez-Pinedo, G., Müller, B., Janka, H.-T., Marek, A., Hix, W. R., Juodagalvis, A., Sampaio, J. M. (2008). Effects of Inelastic



- Neutrino-Nucleus Scattering on Supernova Dynamics and Radiated Neutrino Spectra. *Physical Review Letters*, volume 100(1), pp. 011101–+. [doi:10.1103/PhysRevLett.100.011101](https://doi.org/10.1103/PhysRevLett.100.011101).
- Lattimer, J. M. (2006). Constraints on the Dense Matter Equation of State from Observations. In *American Institute of Physics Conference Series*, pp. 155–162. [doi:10.1063/1.2234397](https://doi.org/10.1063/1.2234397).
- Lattimer, J. M. (2009). personal communication.
- Lattimer, J. M., Prakash, M. (2007). Neutron star observations: Prognosis for equation of state constraints. *Physics Reports*, volume 442, pp. 109–165. [doi:10.1016/j.physrep.2007.02.003](https://doi.org/10.1016/j.physrep.2007.02.003).
- Lattimer, J. M., Swesty, F. D. (1991). A generalized equation of state for hot, dense matter. *Nuclear Physics A*, volume 535, pp. 331–376. [doi:10.1016/0375-9474\(91\)90452-C](https://doi.org/10.1016/0375-9474(91)90452-C).
- Lattimer, J. M., Pethick, C. J., Ravenhall, D. G., Lamb, D. Q. (1985). Physical properties of hot, dense matter: The general case. *Nuclear Physics A*, volume 432, pp. 646–742. [doi:10.1016/0375-9474\(85\)90006-5](https://doi.org/10.1016/0375-9474(85)90006-5).
- Marek, A. (2007). *Multi-dimensional simulations of core collapse supernovae with different equations of state for hot proto-neutron stars*. Ph.D. thesis, Technische Universität München. <http://nbn-resolving.de/urn/resolver.pl?urn:nbn:de:bvb:91-diss-20070424-604499-0-1>.
- Marek, A., Janka, H.-T., Müller, E. (2009). Equation-of-state dependent features in shock-oscillation modulated neutrino and gravitational-wave signals from supernovae. *Astronomy & Astrophysics*, volume 496, pp. 475–494. [doi:10.1051/0004-6361/200810883](https://doi.org/10.1051/0004-6361/200810883).
- Martínez-Pinedo, G., Fischer, T., Lohs, A., Huther, L. (2012). Charged-Current Weak Interaction Processes in Hot and Dense Matter and its Impact on the Spectra of Neutrinos Emitted from Protoneutron Star Cooling. *Physical Review Letters*, volume 109(25), 251104. [doi:10.1103/PhysRevLett.109.251104](https://doi.org/10.1103/PhysRevLett.109.251104).
- Mayle, R., Wilson, J. R. (1988). Supernovae from collapse of oxygen-magnesium-neon cores. *The Astrophysical Journal*, volume 334, pp. 909–926. [doi:10.1086/166886](https://doi.org/10.1086/166886).
- Meyer, B. S., Brown, J. S. (1997). Survey of r-Process Models. *The Astrophysical Journal Supplement Series*, volume 112, pp. 199–220. [doi:10.1086/313032](https://doi.org/10.1086/313032).
- Mezzacappa, A., Bruenn, S. W. (1993a). Stellar core collapse – a boltzmann treatment of neutrino–electron scattering. *The Astrophysical Journal*, volume 410, pp. 740–760. [doi:10.1086/172791](https://doi.org/10.1086/172791).



- Mezzacappa, A., Bruenn, S. W. (1993b). Type II supernovae and Boltzmann neutrino transport - The infall phase. *The Astrophysical Journal*, volume 405, pp. 637–668. doi:10.1086/172394.
- Müller, B., Janka, H., Dimmelmeier, H. (2010). A New Multi-dimensional General Relativistic Neutrino Hydrodynamic Code for Core-collapse Supernovae. I. Method and Code Tests in Spherical Symmetry. *The Astrophysical Journal Supplement Series*, volume 189, pp. 104–133. doi:10.1088/0067-0049/189/1/104.
- Müller, B., Janka, H.-T., Heger, A. (2012a). New Two-dimensional Models of Supernova Explosions by the Neutrino-heating Mechanism: Evidence for Different Instability Regimes in Collapsing Stellar Cores. *The Astrophysical Journal*, volume 761, 72. doi:10.1088/0004-637X/761/1/72.
- Müller, B., Janka, H.-T., Marek, A. (2012b). A New Multi-dimensional General Relativistic Neutrino Hydrodynamics Code for Core-collapse Supernovae. II. Relativistic Explosion Models of Core-collapse Supernovae. *The Astrophysical Journal*, volume 756, 84. doi:10.1088/0004-637X/756/1/84.
- Müller, B., Janka, H.-T., Marek, A. (2013). A New Multi-dimensional General Relativistic Neutrino Hydrodynamics Code of Core-collapse Supernovae. III. Gravitational Wave Signals from Supernova Explosion Models. *The Astrophysical Journal*, volume 766, 43. doi:10.1088/0004-637X/766/1/43.
- Murphy, J. W., Dolence, J. C., Burrows, A. (2013). The Dominance of Neutrino-driven Convection in Core-collapse Supernovae. *The Astrophysical Journal*, volume 771, 52. doi:10.1088/0004-637X/771/1/52.
- Müller, B. (2009). *Multi-Dimensional Relativistic Simulations of Core-Collapse Supernovae with Energy-Dependent Neutrino Transport*. Dissertation, Technische Universität München, München. <http://nbn-resolving.de/urn/resolver.pl?urn:nbn:de:bvb:91-diss-20090519-800389-1-1>.
- Ning, H., Qian, Y.-Z., Meyer, B. S. (2007). r-Process Nucleosynthesis in Shocked Surface Layers of O-Ne-Mg Cores. *The Astrophysical Journal Letters*, volume 667, pp. L159–L162. doi:10.1086/522372.
- Nomoto, K. (1983). Presupernova evolution of 8-12 solar mass stars and the Crab Nebula's progenitor. In J. Danziger, P. Gorenstein, editors, *Supernova Remnants and their X-ray Emission*, volume 101 of *IAU Symposium*, pp. 139–143.
- Nomoto, K. (1984). Evolution of 8–10 solar mass stars toward electron capture supernovae. I – Formation of electron-degenerate O + NE + MG cores. *The Astrophysical Journal*, volume 277, pp. 791–805. doi:10.1086/161749.
- Nomoto, K. (1987). Evolution of 8–10 solar mass stars toward electron capture supernovae. II – Collapse of an O + NE + MG core. *The Astrophysical Journal*, volume 322, pp. 206–214. doi:10.1086/165716.



- Nomoto, K., Sugimoto, D., Sparks, W. M., Fesen, R. A., Gull, T. R., Miyaji, S. (1982). The Crab Nebula's progenitor. *Nature*, volume 299, pp. 803–805. doi:10.1038/299803a0.
- Nomoto, K., Tominaga, N., Blinnikov, S. I. (2014). Electron-capture supernovae of super-asymptotic giant branch stars and the Crab supernova 1054. In S. Jeong, N. Imai, H. Miyatake, T. Kajino, editors, *American Institute of Physics Conference Series*, volume 1594 of *American Institute of Physics Conference Series*, pp. 258–265. doi:10.1063/1.4874079.
- Nordhaus, J., Burrows, A., Almgren, A., Bell, J. (2010). Dimension as a Key to the Neutrino Mechanism of Core-collapse Supernova Explosions. *The Astrophysical Journal*, volume 720, pp. 694–703. doi:10.1088/0004-637X/720/1/694.
- Oppenheimer, J. R., Volkoff, G. M. (1939). On Massive Neutron Cores. *Physical Review*, volume 55, pp. 374–381. doi:10.1103/PhysRev.55.374.
- Otsuki, K., Tagoshi, H., Kajino, T., Wanajo, S. (2000). General Relativistic Effects on Neutrino-driven Winds from Young, Hot Neutron Stars and r-Process Nucleosynthesis. *The Astrophysical Journal*, volume 533, pp. 424–439. doi:10.1086/308632.
- Pons, J. A., Miralles, J. A., Ibanez, J. M. A. (1998). Legendre expansion of the  $\nu\bar{\nu} \rightleftharpoons e^+e^-$  kernel: Influence of high order terms. *A&AS*, volume 129, pp. 343–351. doi:10.1051/aas:1998189.
- Pons, J. A., Reddy, S., Prakash, M., Lattimer, J. M., Miralles, J. A. (1999). Evolution of Proto-Neutron Stars. *The Astrophysical Journal*, volume 513, pp. 780–804. doi:10.1086/306889.
- Qian, Y. Z. (2008). Recent Progress in the Understanding of the r-Process. In *Nuclei in the Cosmos (NIC X)*.
- Qian, Y.-Z., Woosley, S. E. (1996). Nucleosynthesis in neutrino-driven winds. i. the physical conditions. *The Astrophysical Journal*, volume 471(1), pp. 331–351. doi:10.1086/177973.
- Rampp, M., Janka, H.-T. (2002). Radiation hydrodynamics with neutrinos. variable eddington factor method for core-collapse supernova simulations. *Astronomy & Astrophysics*, volume 396, pp. 361–392. doi:10.1051/0004-6361:20021398.
- Reddy, S., Prakash, M., Lattimer, J. M., Pons, J. A. (1999). Effects of strong and electromagnetic correlations on neutrino interactions in dense matter. *Physical Review C*, volume 59, pp. 2888–2918.
- Roberts, L. (2012c). Neutrino interactions near the neutrino sphere in proto neutron stars, [http://stellarcollapse.org/media/micra2013/Luke\\_Roberts.pdf](http://stellarcollapse.org/media/micra2013/Luke_Roberts.pdf). In *MICRA 2013 – Microphysics in Computational Relativistic Astrophysics*.



- Roberts, L. F. (2012). A New Code for Proto-neutron Star Evolution. *The Astrophysical Journal*, volume 755, 126. doi:10.1088/0004-637X/755/2/126.
- Roberts, L. F., Reddy, S., Shen, G. (2012a). Medium modification of the charged-current neutrino opacity and its implications. *Physical Review C*, volume 86(6), 065803. doi:10.1103/PhysRevC.86.065803.
- Roberts, L. F., Shen, G., Cirigliano, V., Pons, J. A., Reddy, S., Woosley, S. E. (2012b). Protoneutron Star Cooling with Convection: The Effect of the Symmetry Energy. *Physical Review Letters*, volume 108(6), 061103. doi:10.1103/PhysRevLett.108.061103.
- Scholberg, K. (2007). Supernova neutrino detection. *ArXiv Astrophysics e-prints*.
- Shen, H., Toki, H., Oyamatsu, K., Sumiyoshi, K. (1998a). Relativistic equation of state of nuclear matter for supernova explosion. *Progress of Theoretical Physics*, volume 100, pp. 1013–1031. doi:10.1143/PTP.100.1013.
- Shen, H., Toki, H., Oyamatsu, K., Sumiyoshi, K. (1998b). Relativistic equation of state of nuclear matter for supernova and neutron star. *Nucl. Phys. A*, volume 637, pp. 435–450. doi:10.1016/S0375-9474(98)00236-X.
- Shen, H., Toki, H., Oyamatsu, K., Sumiyoshi, K. (2011). Relativistic equation of state for core-collapse supernova simulations. *The Astrophysical Journal Supplement Series*, volume 197(2), p. 20.
- Siess, L. (2006). Evolution of massive AGB stars. In T. Montmerle, C. Kahane, editors, *EAS Publications Series*, volume 19 of *EAS Publications Series*, pp. 103–124. doi:10.1051/eas:2006028.
- Sinnott, B., Welch, D. L., Rest, A., Sutherland, P. G., Bergmann, M. (2013). Asymmetry in the Outburst of SN 1987A Detected Using Light Echo Spectroscopy. *The Astrophysical Journal*, volume 767, 45. doi:10.1088/0004-637X/767/1/45.
- Steiner, A. W., Hempel, M., Fischer, T. (2013). Core-collapse Supernova Equations of State Based on Neutron Star Observations. *The Astrophysical Journal*, volume 774, 17. doi:10.1088/0004-637X/774/1/17.
- Sumiyoshi, K., Yamada, S., Suzuki, H., Shen, H., Chiba, S., Toki, H. (2005). Postbounce Evolution of Core-Collapse Supernovae: Long-Term Effects of the Equation of State. *The Astrophysical Journal*, volume 629, pp. 922–932. doi:10.1086/431788.
- Takahara, M., Hino, M., Oda, T., Muto, K., Wolters, A. A., Glaudemans, P. W. M., Sato, K. (1989). Microscopic calculation of the rates of electron captures which induce the collapse of O+Ne+Mg cores. *Nuclear Physics A*, volume 504, pp. 167–192. doi:10.1016/0375-9474(89)90288-1.



- Takahashi, K., Wittl, J., Janka, H.-T. (1994). Nucleosynthesis in neutrino-driven winds from protoneutron stars II. The r-process. *Astronomy & Astrophysics*, volume 286, pp. 857–869.
- Thompson, T. A., Burrows, A., Meyer, B. S. (2001). The Physics of Proto-Neutron Star Winds: Implications for r-Process Nucleosynthesis. *The Astrophysical Journal*, volume 562, pp. 887–908. doi:10.1086/323861.
- Thompson, T. A., Burrows, A., Pinto, P. A. (2003). Shock breakout in core–collapse supernovae and its neutrino signature. *The Astrophysical Journal*, volume 592, pp. 434–456. doi:10.1086/375701.
- Tolman, R. C. (1939). Static solutions of einstein’s field equations for spheres of fluid. *Phys. Rev.*, volume 55(4), pp. 364–373. doi:10.1103/PhysRev.55.364.
- Tominaga, N., Blinnikov, S. I., Nomoto, K. (2013). Supernova Explosions of Superasymptotic Giant Branch Stars: Multicolor Light Curves of Electron-capture Supernovae. *The Astrophysical Journal Letters*, volume 771, L12. doi:10.1088/2041-8205/771/1/L12.
- Wanajo, S. (2013). The r-process in Proto-neutron-star Wind Revisited. *The Astrophysical Journal Letters*, volume 770, L22. doi:10.1088/2041-8205/770/2/L22.
- Wanajo, S., Nomoto, K., Janka, H.-T., Kitaura, F. S., Müller, B. (2009). Nucleosynthesis in Electron Capture Supernovae of Asymptotic Giant Branch Stars. *The Astrophysical Journal*, volume 695, pp. 208–220. doi:10.1088/0004-637X/695/1/208.
- Wanajo, S., Janka, H.-T., Müller, B. (2011). Electron-capture Supernovae as The Origin of Elements Beyond Iron. *The Astrophysical Journal Letters*, volume 726, L15. doi:10.1088/2041-8205/726/2/L15.
- Wanajo, S., Janka, H.-T., Müller, B. (2013a). Electron-capture Supernovae as Origin of  $^{48}\text{Ca}$ . *The Astrophysical Journal Letters*, volume 767, L26. doi:10.1088/2041-8205/767/2/L26.
- Wanajo, S., Janka, H.-T., Müller, B. (2013b). Electron-capture Supernovae as Sources of  $^{60}\text{Fe}$ . *The Astrophysical Journal Letters*, volume 774, L6. doi:10.1088/2041-8205/774/1/L6.
- Wittl, J., Janka, H.-T., Takahashi, K. (1994). Nucleosynthesis in neutrino-driven winds from protoneutron stars I. The  $\alpha$ -process. *Astronomy & Astrophysics*, volume 286, pp. 841–856.
- Woosley, S., Heger, A., Weaver, T., Langer, N. (1997). Sn 1987a — presupernova evolution and the progenitor star. preprint MPA-1024, MPI f. Astrophysik, Garching.



Woosley, S. E., Hoffman, R. D. (1992). The alpha-process and the r-process. *The Astrophysical Journal*, volume 395, pp. 202–239. [doi:10.1086/171644](https://doi.org/10.1086/171644).





# Danksagung

Als erstes möchte ich mich an dieser Stelle bei all denjenigen bedanken, die diese Arbeit möglich gemacht haben. In erster Linie bei meinem Betreuer Hans-Thomas Janka, der mir die Möglichkeit geboten hat in diesem Thema zu arbeiten. Weiterhin möchte ich Bernhard Müller danken für die Unterstützung bei der Bearbeitung seines Codes. Natürlich möchte ich mich auch bei der Gruppe bedanken, ganz besonders bei Alexandra, du bist meine Heldin, und bei Andi fürs mitfluchen. Lorenz, vielen Dank für die hilfreichen Plotting-Routinen und das tolle Skript fürs Daumenkino.

Thank you Margi and Andressa for necessary distraction.

Vielen Dank, auch an Steffi und Axel, dass ich immer ihre Gute Stube zum Schreiben benutzen durfte. Lorenz und Kathi vielen Dank fürs Korrekturlesen.

Am allermeisten aber möchte ich mich bei meiner Familie bedanken. Für die tolle Unterstützung und Anteilnahme und dass ihr mich bis hier her begleitet und geprägt habt. Mama, du hast mich zu der gemacht die ich bin, ich find dich toll! Und die vielen lieben Grüße haben mir sehr geholfen und mich aufgeheitert. Ich danke dir Lorenz das du mir durch diese immer noch schwere Zeit geholfen hast, ohne dich hätte ich das nie geschafft! Gut, dass es dich gibt.

Vielen Dank an meinen Papa, ich hoffe ich hätte dich hiermit stolz gemacht!

